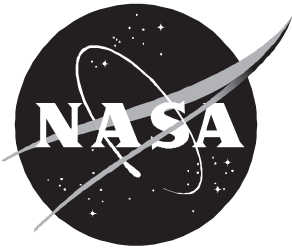# Invariance of Hypersonic Normal Force Coefficients With Reynolds Number and Determination of Inviscid Wave Drag From Laminar Experimental Results

Jim A. Penland and Richard Hawkins

Invariance of Hypersonic Normal Force Coefficients With Reynolds Number and Determination of Inviscid Wave Drag From Laminar Experimental Results

Jim A. Penland
Langley Research Center • Hampton, Virginia

Richard Hawkins
Analytical Services & Materials, Inc. • Hampton, Virginia

Contents

Abstract

Observations have been made and reported that the experimental normal force coefficients at a constant angle of attack were constant with a variation of more than 2 orders of magnitude of Reynolds number at a free-stream Mach number M_∞ of 8.00 and more than 1 order of magnitude variation at $M_\infty = 6.00$ on the same body–wing hypersonic cruise configuration. These data were recorded under laminar, transitional, and turbulent boundary-layer conditions with both hot-wall and cold-wall models. This report presents experimental data on 25 configurations of 17 models of both simple and complex geometry taken at $M_\infty = 6.00$, 6.86, and 8.00 in 4 different hypersonic facilities. Aerodynamic calculations were made by computational fluid dynamics (CFD) and engineering methods to analyze these data. The conclusions were that the normal force coefficients at a given altitude are constant with Reynolds numbers at hypersonic speeds and that the axial force coefficients recorded under laminar boundary-layer conditions at several Reynolds numbers may be plotted against the laminar parameter (the reciprocal of the Reynolds number to the one-half power) and extrapolated to the ordinate axis to determine the inviscid-wave-drag coefficient at the intercept.

Introduction

The vitally important performance parameters lift, drag, and the range factor lift-drag ratio are oriented in the wind axis system and may be determined directly from mechanical or electronic force measuring devices attached to test models exposed to natural or artificial fluid flow. These performance parameters are usually and more efficiently determined by measuring the more basic load components—the normal force and axial force, which are oriented in the body axis system, at each angle of attack. The lift, drag, and lift-drag ratio are calculated trigonometrically and put in coefficient form by dividing by the reference conditions.

Of particular importance were the observations reported in reference 1 that the experimental normal force coefficients, at a constant attitude, were constant with a variation of more than 2 orders of magnitude of Reynolds number at a free-stream Mach number M_∞ of 8.00; reference 2 reports more than 1 order of magnitude variation at $M_\infty = 6.00$ on the same body–wing hypersonic cruise configuration. These data, recorded under laminar, transitional, and turbulent boundary-layer conditions, consisted of test runs at 65 different Reynolds numbers at $M_\infty = 8.00$ in 2 different facilities with both hot-wall and cold-wall test models and 30 runs at $M_\infty = 6.00$ with a hot-wall test model.

If the normal force coefficients are constant with Reynolds number, the determination of lift, drag, and lift-drag ratio is simplified by at least 50 percent, as only the axial force coefficients are left to be accurately assessed with Reynolds number. The axial force coefficients of concept configurations can be estimated by a number of analytic, empirical, and individual component summation methods. Simple shapes having only bow shocks lend themselves well to all methods. The drag of configurations with wings, vertical surfaces, and/or inlets that produce additional shocks downstream of the bow shock introduce changes in dynamic pressure, and flow angularity, that, short of future proven time-consuming and expensive computational fluid dynamics (CFD) programs, cannot be estimated with the desired accuracy. The axial force coefficients therefore encompass not only the inviscid pressure drag but also all the viscous drag contributions that are affected methodically and indelibly by any variation in Reynolds number.

Blasius and others have established that all laminar viscous parameters may be expressed as functions of Reynolds number—to be exact, the reciprocal of Reynolds number to the one-half power for values greater than about 1000. All these laminar parameters—the skin friction, the boundary-layer depth, and the momentum, displacement, and energy thickness—are used at various speed ranges with the appropriate temperatures to study laminar viscous aerodynamic drag. Ratios of these various thicknesses, known as shape factors, have been used successfully, in conjunction with surface roughness, to predict transition and laminar separation locations at lower speeds. Because all laminar viscous parameters can be expressed as functions of the reciprocal of the Reynolds number to the one-half power $1/\sqrt{R_l}$, it is logical to assume that any combination of these parameters would also be a function of $1/\sqrt{R_l}$ and to use this factor to predict viscous drag under laminar conditions at higher or lower Reynolds numbers. A successful attempt was made in reference 1 to predict the inviscid axial force coefficient at very high Reynolds numbers that approached infinity on a highly streamlined body–wing concept by plotting the experimental axial force coefficients versus the factor $1/\sqrt{R_l}$ and then extrapolating these data to the ordinate axis. This

intercept value coincided with the inviscid calculated result made with the hypersonic arbitrary-body aerodynamic program (HABAP) of reference 3.

The present paper presents additional experimental evidence that the normal force coefficients are constant with Reynolds number and that the inviscid axial force coefficients can be determined by the extrapolation process. Experimental data on 25 configurations of 17 different models of both simple and complex geometry, taken at $M_\infty = 6.00$, 6.86, and 8.00 in 4 hypersonic test facilities, are used. Aerodynamic calculations determined by CFD are used where possible, supplemented by engineering methods applied by hand and machine. Additional analysis of the data at $M_\infty = 8.00$ of reference 1 and $M_\infty = 6.00$ of reference 2 are also included.

Symbols

A	aspect ratio
b	wing span
C_A	axial force coefficient, $\dfrac{F_A - F_b}{q_\infty S_r}$
$C_{A,LE}$	axial force coefficient at leading edge
C_F	average skin friction coefficient
C_N	normal force coefficient, $\dfrac{F_N}{q_\infty S_r}$
C_p	pressure coefficient
$(C_{p,\max})_{st}$	stagnation pressure coefficient, $\dfrac{p_{t,2}/p_{t,1} - p_\infty/p_{t,1}}{(\gamma/2M_\infty^2)(p_\infty/p_{t,1})}$
c	wing chord
c_{cl}	centerline chord
c_r	root chord of delta or caret wing
d	base diameter or disk diameter
F_A	axial force along X-axis (positive direction, $-X$)
F_b	base pressure correction, $(p_\infty - p_b) S_b$
F_N	normal force along Z-axis (positive direction, $-Z$)
H_e	effective test section height
l	model length
M_∞	free-stream Mach number
p_b	base pressure
$p_{t,1}$	total pressure
$p_{t,2}$	total pressure behind normal shock
p_∞	free-stream pressure
q_∞	free-stream dynamic pressure

R_l	free-stream Reynolds number based on maximum chord or body
S_b	base area
S_p	planform area
S_r	reference area, varies with model
t	maximum thickness
V	total volume of model
$\dfrac{V^{2/3}}{S_p}$	nondimensional volume parameter
X,Z	body axes
α	angle of attack, deg
β	angle of sideslip, deg, or flow expansion angle, deg
γ	ratio of specific heats, 1.4
δ	flow deflection, deg, or boundary-layer thickness
δ_E	elevon deflection, deg
δ_H	horizontal tail deflection, deg
δ^*	boundary-layer displacement thickness
θ	cone half-angle (semivertex angle) or wedge angle, deg (see fig. 2)
Λ	sweep angle of wing leading edge, deg
$1/\sqrt{R_l}$	laminar-flow parameter
$1/\sqrt[7]{R_l}$	turbulent-flow parameter

Model components:

B	body
C	cone
D	delta
E	elevon
H	horizontal tail
I	inlet
V	vertical tail
W	wing

Abbreviations:

BBMN	blunt body modified Newtonian, $(C_{p,\max})_{st}$ = Stagnation pressure coefficient
CFD	computational fluid dynamics
GASP	General Aerodynamic Simulation Program
HABAP	Hypersonic Arbitrary-Body Aerodynamic Program, Mark III
JPL HWT	Jet Propulsion Laboratory Hypersonic Wind Tunnel

Presentation of Models and Data

The models and data are presented in the following figures:

Apparatus and Test Conditions

Data measured in four different hypersonic facilities were analyzed and are discussed in this paper. At each of the four installations, the stagnation temperature was set sufficiently high to avoid liquefaction and remain above the supersaturated region, as defined by reference 4 for all tests. All screw, dowel holes, and joints were filled with dental plaster before each test was run.

Langley 11-Inch Hypersonic Tunnel

Most of the tests presented in this paper on right circular cones, rectangular wings, delta wings, and a caret wing were conducted in the Mach number 6.86 test section of the Langley 11-Inch Hypersonic Tunnel (now decommissioned). The design of this facility may be found in references 5 and 6. The contours of the two-dimensional nozzle constructed of invar were calculated by Ivan E. Beckwith and are presented in figure 13. Invar was used to construct this nozzle to alleviate the deflection of the first minimum that occurred in the steel nozzle of reference 6 because of differential heating of the nozzle blocks. The tunnel-wall boundary-layer thickness and, therefore, the free-stream Mach number of this test section were dependent upon the stagnation pressure.

For these tests, the stagnation pressure was varied from about 74 to 515 psia, and the stagnation temperature varied from 1040°R to 1150°R. These conditions resulted in an average free-stream Mach number from 6.70 to 6.90 and a unit Reynolds number per foot from 0.617×10^6 to 4.29×10^6, as well as an average Reynolds number based on model length from 0.58×10^6 to 5.35×10^6. The absolute humidity was kept to less than 1.9×10^{-5} lb of water/lb of dry air for all tests. The 11-Inch Hypersonic Tunnel had predominantly laminar flow conditions at all operating pressures; this was substantiated by tests where the transition on a sharp-edged hollow cylinder was experimentally measured in this tunnel at Reynolds numbers as high as 5.7×10^6 (ref. 7). Similar tests on a sharp-edged flat plate showed transition began at a Reynolds number of about 2×10^6 in this tunnel (ref. 8). A private communication from Pierce L. Lawing of the Langley Research Center, who retested the flat plate of reference 8, indicates, however, that his tests showed that, by meticulously cleaning the tunnel walls and throat of dust particles and other debris before each test, he could increase the transition Reynolds number to about 5×10^6, and conversely, by intentionally adding roughness to the tunnel walls in the form of minute glass beads, he could reduce the transition Reynolds number to values approaching the 2×10^6 shown in reference 8. All models were tested on two-, three-, or six-component strain-gauge balances. The size of models for the 11-Inch Tunnel was determined by the method described in appendix A.

Langley Mach 8 Variable-Density Tunnel

The Langley Mach 8 Variable-Density Tunnel (VDT) (now decommissioned) consisted of an axially symmetric nozzle with contoured walls, had an 18-in-diameter test section, and operated on a blowdown cycle. The tunnel-wall boundary-layer thickness, and therefore the free-stream Mach number, were dependent upon the stagnation pressure. For these tests, the stagnation pressure was varied from about 128 to 2835 psia and the stagnation temperature was varied from about 1135°R to 1480°R. These conditions resulted in an average free-stream Mach number from 7.74 to 8.07 and a Reynolds number based on fuselage length from 1.371×10^6 to 27.084×10^6 (0.636×10^6 to 12.539×10^6/ft). Dry air was used for all tests to avoid any condensation effects. The calibration of this tunnel for the present tests is discussed in reference 1. The model of an advanced blended body-wing hypersonic cruise concept (fig. 2(g)), was

tested in the Mach VDT on a sting-mounted, internal, six-component, water-cooled strain-gauge balance. This combination was injected into the hypersonic flow after the blowdown cycle had begun and retracted before the cycle was stopped. Tests were made at a fixed angle of attack, and the final data were corrected for sting deflection.

Calspan Hypersonic Shock Tunnel

The Calspan 96-Inch Hypersonic Shock Tunnel, described in reference 9, employs a reflected shock to process air to conditions suitable for supplying an axially symmetric, convergent-divergent hypersonic nozzle. For the tests discussed herein, the shock-processed air was expanded through the contoured nozzle, which has interchangeable throats, to the desired test conditions at the 24-in. exit diameter. Test time varied with conditions up to about 13 ms duration. For the shock-tunnel tests, the stagnation pressure varied from about 337 to 18 650 psia (22.9 to 1269 atm), and stagnation temperature varied from about 691°R to 3973°R (231°F to 3513°F) not only to avoid liquefaction but also to tailor the wide range of test Reynolds number to a Mach number of approximately 8 (varying only from 7.507 to 8.26). (These conditions resulted in a Reynolds number based on fuselage length from 0.527×10^6 to 160.7×10^6 (0.244×10^6 to 74.4×10^6/ft).) Some of the higher stagnation temperatures were used at the lower stagnation pressures to help obtain the lower Reynolds numbers by increasing viscosity and lowering the density. The free-stream Mach number was determined from pitot pressures measured for each test run by means of piezoelectric crystal pressure transducers mounted in the test section. The advanced blended body–wing hypersonic cruise model was tested in the Calspan Shock Tunnel on a three-component strain-gauge balance (fig. 2(g)).

Langley 20-Inch Mach 6 Tunnel

The Langley 20-Inch Mach 6 Tunnel operates on a blowdown cycle through a 2-D nozzle with a test section 20.5 in. high and 20 in. wide. Dry air was used for all tests to avoid water condensation effects. Tests were conducted at free-stream Mach numbers from 5.799 to 5.994, stagnation pressures from 34.3 to 525 psia, and stagnation temperatures from about 784°R to 912°R. These conditions resulted in an average free-stream Reynolds number based on fuselage length from 1.562×10^6 to 19.067×10^6 (0.723×10^6 to 8.827×10^6/ft) (ref. 10).

A six-component, water-cooled strain-gauge balance was installed inside the advanced blended body–wing hypersonic cruise model body and attached to the tunnel variable-angle sting-support system (fig. 2(g)). Forces

and moments were measured through a range of angle of attack from $-1°$ to $8°$.

Models and Tests

Photographs of all models presented in this report are shown in figure 1. All models were fabricated from metal, hollowed to decrease weight where practical, and tested on multicomponent strain-gauge balances. For most tests the angle of attack was set prior to each test point in both the 11-Inch Hypersonic Tunnel and the 20-Inch Mach 6 Tunnel by projecting a point source of light onto a lens-prism combination installed in the model wall and reading the reflected image on a calibrated chart. Accuracy of $\pm 0.050°$ was possible with this method. The exceptions to this hands-on procedure were the tests for the advanced blended body–wing configuration in the Mach 8 VDT and Hypersonic Shock Tunnel. During these tests, the model was mounted on either a six-component or three-component strain-gauge balance in the test region at the prescribed angle of attack before the test run; then the final angle was determined from sting-bending calibrations and measured air loads. The accuracy of this method is equal or superior to the light-impingement method described previously. All data reported herein were corrected to base pressure equal to free-stream static pressure, and all tests were made with free transition.

Cones

Data from three separate cone test programs (refs. 11 to 13) are presented in figure 3. Models were machined from either stainless steel or aluminum alloys, as indicated in figure 2. The smaller stainless steel models were tested on a two-component external strain-gauge balance, and the larger aluminum models and the one large stainless steel model were tested on six-component, internal-external strain-gauge balances. The strain gauges and the associated flexural beams are located outside the test model for external balances and housed in protective covers to shield them from the hot air flow. The internal-external balances had the axial force and rolling-moment components externally housed from the model; the remaining four components, consisting of normal force, side force, pitching-moment, and yawing-moment components, were mounted inside the model with the moment center coinciding with the selected center of gravity in the model. The reference area for the cones is the base area.

Wings

The rectangular, delta, and caret wings were all machined from aluminum alloy (figs. 2(b) to (d)), and care was taken to maintain all leading edges as sharp as

possible (refs. 14 and 15). These models were tested on a three-component, external, water-cooled strain-gauge balance. The reference area for the rectangular, delta, and caret wings is the planform area.

Blended and Distinct Body–Wing Configurations

These complete airplane configurations (figs. 2(e) and (f)), designed and tested for references 16 and 17, were cast from aluminum with wooden pattern models. Wing surfaces and balance cavities were machined and bored after casting. Flow-through engine inlet cowls were machined from stainless steel and attached to the models with screws. Elevon deflections were facilitated on the blended body–wing model by interchangeable elevons that had machined angles and were attached by screws. The horizontal tails of the distinct body–wing model were rotated about small shafts machined on the hinge line that extended into the fuselage side and were held in place by set screws from the base of the model. The reference area for the blended and distinct body–wing configurations is the wing area including the fuselage intercept.

Advanced Blended Body–Wing Test Configuration

This advanced blended body–wing configuration (fig. 2(g)) was designed primarily for tests at high Reynolds numbers in the Calspan Shock Tunnel (refs. 1, 2, and 18) and was machined from a solid billet of 4130 steel because of the inherent high strength and weldability of the steel. The model was hollowed out, and a cover was welded on prior to final machining. This model had leading-edge diameters and trailing-edge heights of 0.006 in. The reference area for the advanced blended body–wing configuration is the wing area including the fuselage intercept.

Theoretical Methods

In keeping with the variety of different model types studied in the present paper, a variety of theoretical methods were used to predict the forces and viscous effects encountered during the wind tunnel and shock tunnel tests. Estimates were made by hand with a desk calculator on the simple flat faceted wing models, the HABAP (Hypersonic Arbitrary-Body Aerodynamic Program, Mark III) (ref. 3) was used to provide engineering predictions on the more complex airplane configurations, and the GASP (General Aerodynamic Simulation Program) (refs. 19 to 22) was used to provide inviscid and viscid CFD predictions for selected cones and wings.

Engineering Predictions

Inviscid forces were determined, where possible, from tables calculated by CFD methods (i.e., the values of C_N and C_A for cones at angles of attack below the semivertex angle). (See refs. 23 to 25.) Forces on the 2-D wedge wings, the three-dimensional (3-D) delta wings, and the caret wing were determined by tangent-wedge–Prandtl-Meyer (TW–PM) theory. The one exception was the use of the tangent-cone–Prandtl Meyer (TC–PM) theory on the very slim 85° swept delta wing. Hand calculations required that the airstream surface of the configuration under consideration be divided into panels and that the local flow deflection angle be determined. From this flow deflection angle, the local pressure coefficient was determined from oblique shock charts or tables if in compression or from PM charts or tables if in expansion. These pressure coefficients were then summed with the appropriate area ratios to determine the normal and axial force coefficients. Hand calculations were greatly simplified by the use of cross plots of oblique shock and PM expansion pressure coefficients versus Mach number and flow deflection angle calculated from the table of reference 26 and cone pressure coefficients of references 23 to 25. The HABAP, of course, has these pressure coefficients stored in the computer program. The present in-house HABAP has been modified to optionally use a lookup table for cone pressure coefficients, instead of the empirical equations of the original program, and the option of limiting the expansion coefficients to a value equal to $-1/M_\infty^2$ (ref. 27). Both options were used in the present theoretical estimates. All calculations assumed free-stream static pressure on the bases of models.

Modified Newtonian Theory

Blunt-Body Option

An estimation of the axial force contribution from the bluntness of the model noses and leading edges was made by the proven modified Newtonian theory, which substitutes the maximum stagnation pressure coefficient of the Mach number under study for the classic Newtonian value of 2.0 and is known as the blunt-body option (BBMN). For $M_\infty = 6.86$, $(C_{p,\max})_{st}$ is 1.823. Of historical interest is that this concept, when first reported by the author, was considered sensitive to the national interest and was published as a classified NACA report (ref. 28) in March 1954, declassified in 1956, and republished as unclassified in 1957 (ref. 29). The modified Newtonian drag coefficient for a sphere at $M_\infty = 6.86$ is equal to $(C_{p,\max})_{st}/2$ or 0.911; that of a cylinder normal to the flow is equal to $2/3(C_{p,\max})_{st}$ or 1.215. These constants were used herein for the model nose and leading-edge estimates, respectively, with the leading-edge sweep taken into account.

Sharp-Body Option

By substituting $M_\infty = \infty$ into the oblique shock equations, the so-called sharp-body option to the Newtonian theory (SBMN) was derived in reference 30, whereas $C_{p,\max}$ was found to be $(\gamma + 1)$ or 2.4. This option was used herein on the faceted configurations for reference.

Skin Friction

The axial force contribution of laminar skin friction for the cones and faceted wing models was made by use of the Monaghan reference temperature method of reference 31, taking into account the ratio of wetted area to reference area, the dynamic pressure increase across the leading-edge shocks, and the variation of surface angularity with the reference axis. Determination of the average skin friction by the Monaghan method takes into account the local Mach number, static temperature and pressure, and the model wall temperature and planform effects. The skin friction on the cones used the well-known Mangler transformation to modify flat-plate skin friction to that applicable to conical bodies (ref. 32). No induced effects were included in the final summation.

Computational Fluid Dynamics

CFD calculations were made with the GASP (refs. 19 to 22), which solves the integral form of the 3-D compressible Navier-Stokes equations. GASP uses a cell-centered, finite-volume formulation with upwind-biased spatial discretization.

The code is able to switch from solving the Navier-Stokes equations in elliptic (or global iteration) mode to the parabolized Navier-Stokes (PNS) equations in the space marching mode. The code marches by iterating on cross-flow planes to converge the solution plane by plane. The Vigneron technique (ref. 22) is used to limit the streamwise pressure gradient in the subsonic portion of the boundary layer to avoid departure solutions. All cases were marched taking advantage of the nature of the problem in that signals cannot travel upstream in a supersonic flow field. All the solutions obtained in this paper used either a no-slip, fixed-wall temperature or no-slip, adiabatic boundary condition applied at the surface, except for the infinite Reynolds number cases (inviscid), which had tangency imposed at the surfaces.

The 2-D wedge, delta-wing, and caret-wing grids were blocked. As an example of this blocking strategy, imagine a cross section of the delta wing. Capture of the flow around the wing required a total of four rectangular grid blocks: two blocks directly above and below the wing and two more blocks adjacent to these to capture the flow outboard of the wingtip. Pairs of blocks could be combined in a number of ways, such as combining the two upper blocks into one, the two lower blocks, or the two outboard blocks; but for simplicity of setup, the blocks were kept separate. The blocks exchanged flow information with neighboring blocks across their boundaries as the solution was marched downstream. The grid densities were 65 by 65 by 65 for each block.

The grids were tailored to resolve viscous effects. Grid points were clustered near the surface to resolve the boundary layer and hence the skin friction. All the first spacings off of the surfaces were set at 1×10^{-4} in. The axial spacings were clustered at the leading edge to resolve the viscous-inviscid interaction that creates high pressure and high skin friction values initially, but these values decrease rapidly downstream. Spanwise clustering also captured the decrease in boundary-layer thickness and the resulting increase in skin friction near wingtips caused by edge effects.

To decrease convergence time without sacrificing accuracy, all the grids started at a small distance downstream from the leading edge (on the order of 0.02 in.). This procedure prevented one or more of the grid blocks from becoming singular at the leading edge of the geometry. For example, on the 3-D wedge, a grid block on the side of the wedge collapses to a line if begun at the leading edge of the geometry. Convergence becomes very slow near a singular edge, and the solution can be unstable because of the discontinuous spacing at the boundaries where the blocks exchange information with their neighbors.

To ensure accuracy, a simple grid-convergence test was performed. Each case was solved twice: once on the fine grid, and again, on the coarse grid—every other point in the fine grid was taken out in each direction, which means the fine grid had 2^3 or 8 times as many points as the coarse grid. Also, the spacing off the wall was slightly more than halved from the coarse to the fine grids. Almost all the cases had less than 1 percent difference in axial and normal force coefficients for the coarse and fine grid results. (The exception was the caret wing at 6° angle of attack, which showed less than 2 percent difference.) A cross section of the trailing-edge grid for all configurations is presented in figure 14.

Results and Discussion

The study of the invariance of normal force coefficient with Reynolds number under all viscous conditions and the determination of the inviscid axial force, or wave drag, under laminar-boundary-layer flow conditions consisted of the analysis of data recorded on 17 separate models. One configuration was tested at both $M_\infty = 6.00$ and 8.00, and 16 shapes were tested at about $M_\infty = 6.86$ (refs. 1, 2, and 11 to 15), two of which had pitch-control

deflections of +5° to −5° and of +5° to −15°. Two configurations were tested with and without engine inlet installation, and one was tested at $\beta = 0°$ and $\beta = -4°$, for a total of 26 test models or test conditions. Normal force coefficients were available for all configurations and axial force coefficients, with accurate base pressure corrections and minimum scatter tested under laminar conditions, were available for 10 of the models. For the overall tests, the angle of attack varied from 0° to as high as 30°, and the Reynolds number based on model length varied from about 0.35×10^6 to 161×10^6.

Right Circular Cones

Normal Force

The normal force coefficients for sharp-nosed, right-circular cones are presented in figures 3(a)–(d) at various angles of attack and $M_\infty = 6.70$ to 6.89. (See refs. 11 to 13). These data, recorded under laminar flow conditions, are shown plotted against Reynolds number based on model length. The normal force coefficient C_N may be observed to be constant with Reynolds number at each angle of attack for each of the cone models that had semivertex angles θ of 5°, 10°, 20°, and 30°. It therefore seems reasonable to assume that, if the normal force coefficient does not vary with Reynolds number, it is not significantly affected by viscous effects, which do vary greatly with Reynolds number. Furthermore, under the same conditions, inviscid calculations should give good estimates. Inviscid normal force values from references 23 to 25 are shown for some of the lower angles of attack for all four cones (fig. 3) and verify that the inviscid values of C_N provide good predictions of the viscid experimental normal force coefficients on cones. To further examine this hypothesis and determine theoretical axial force coefficients, limited CFD calculations were made with the GASP code of references 19 to 22 on the cones with $\theta = 5°$ and 10° at angles of attack up to 10° under both viscid and inviscid flow conditions. The grid used for these calculations, discussed in the section "Theoretical Methods," is shown in figure 14. The results of the calculations presented in figures 3(a) and (b) show that the viscid and inviscid C_N values were within 1 percent of each other, and the CFD methods of references 23 to 25 give identical inviscid values. This parabolized Navier-Stokes code is not necessarily limited to calculations at angles of attack on cones to those angles equal to or less than the cone half-angle, but by selecting an angle of attack of 10°, relatively high pressures were encountered for summation and expensive machine time was conserved. Additional PNS calculations on a right-angle circular cone $\theta = 10°$ with and correlation with experimental results at $M_\infty = 7.95$ may be found in reference 33. Therefore the conclusions are that the experimental and CFD-calculated normal force coeffi-

cients for right-circular cones with half-angles of 5° to 30° at any given angle of attack and Mach number are constant with Reynolds number and that inviscid calculations give excellent predictions of the parameter.

Axial Force

The determination of inviscid axial force coefficient C_A was made by plotting the experimental values at constant angles of attack against the reciprocal of the square root of the Reynolds number (i.e., $1/\sqrt{R_l}$) and fairing the data to the ordinate axis. This intercept is then a measure of the axial force at a very high Reynolds number that approaches infinity and, therefore, is an estimate of the inviscid axial force coefficient. Note that this straight-line extrapolation of axial force coefficients is valid only for data recorded under laminar-flow boundary-layer conditions. The data presented in figures 3(a) and (b) for the cones with $\theta = 5°$ and 10°, recorded at $M_\infty = 6.86$ under laminar-flow conditions, were faired to the ordinate axis and compared with inviscid coefficients from references 23 to 25; the agreement with the inviscid theory was excellent. The results of the use of the GASP CFD code to calculate the axial force coefficient C_A for the cones with $\theta = 5°$ and 10° are presented in figures 3(a) and (b). Not only did the inviscid values, also referred to as "Euler values," at various angles of attack correlate precisely with the calculations of references 23, 24, and 25 but also the viscous values at different Reynolds numbers plotted on a straight line extrapolated back to the ordinate to the inviscid value when plotted against the laminar boundary-layer parameter $1/\sqrt{R_l}$. The conclusion may be made that accurate estimates of the inviscid axial force coefficients for cones at a given angle of attack and constant Mach number may be obtained by extrapolation of laminar experimental data by using the parameter $1/\sqrt{R_l}$. The study of cone drag in reference 34 at $M_\infty = 10$ and 14 provides additional data to support this conclusion.

Two-Dimensional Wedge Wings

Normal Force

To further study the normal force coefficients invariance with Reynolds number, four 2-D wedge wings that were tested at $M_\infty = 6.86$ (refs. 14 and 15) were considered. These wings had aspect ratios of 0.35, 1.07, and 3.0 and were tested at two different Reynolds numbers (fig. 4). Two wings with aspect ratio 1.07 had thickness ratios of 0.116 and 0.234. The normal force coefficient data from all these wings were constant with Reynolds number through the relatively wide change in aspect ratio and the variation in magnitude of the tip effects. Inviscid estimates were made by the TW theory with the oblique-shock and PM expansion tables of reference 26 for all

configurations. Corrections for pressure decreases near the tip were accounted for by use of linear theory based on free-stream Mach angle, as presented in reference 35. More rigorous calculations were made for the 2-D wing model W1, which had an aspect ratio of 0.35 when the GASP code of references 19 to 22 was used. This wing would be expected to have the greatest tip losses and thus be a more exacting test of the CFD code. The theoretical predictions by the TW–PM theory were good, particularly at the lower angles of attack and for the models of higher aspect ratio where the tip effects were reduced. An estimation of the effect of C_F of the triangular sides of the models on C_N was made and found to be negligible. Superior C_N predictions were obtained from the GASP CFD program, particularly at the highest angle of attack of 14°. The trailing edge of the input grid discussed in the section "Theoretical Methods" may be seen in figure 14. Inviscid values of C_N were unexpectedly slightly higher than the viscid calculations. Oil flows on wing W4 are shown in figure 7(a), taken at an angle of attack of 9°. These pictures show a slight outflow near the tips on the bottom and inflow on the top view of the wing, as would be expected; no flow separation or vorticity can be observed. At the three angles of attack studied up to $\alpha = 14°$, the values of C_N were constant with Reynolds number. It may be concluded that the normal force coefficients for 2-D wedges of various aspect ratios are constant with Reynolds number for any given angular attitude and Mach number, both experimentally and theoretically.

Axial Force

The inviscid axial force coefficients for the wedge models were estimated by the extrapolation process used for the cones and are presented in figures 4(a)–(c). The results were excellent, particularly for the model having an aspect ratio of 3, where the scatter of the experimental data was small and the correlation with the theoretical estimates was enhanced by the smaller tip losses. Inviscid estimates of axial force by the CFD program (fig. 4(a)) were of slightly higher magnitude than those by the TW–PM method. As observed on the conical models, the viscid calculations extrapolated to the inviscid values. For 2-D wedge wings, it may be concluded that inviscid axial force coefficients may be estimated with confidence by the extrapolation of laminar data with the parameter $1/\sqrt{R_l}$.

Three-Dimensional Delta Wings

Normal Force

Experimental data taken at $M_\infty \approx 6.86$ and at five different Reynolds numbers on flat-bottom rooftop delta wings (ref. 14) are presented in figures 5(a)–(e). These delta wings had leading-edge sweep angles that varied from 75° to 85°, thickness ratios of 0.088 and 0.176 that corresponded to streamwise wedge angles of 5° and 10°, and aspect ratios that varied from 0.35 to 1.07 because of the leading-edge sweep changes. The normal force coefficient was constant at any given angle of attack through a nearly sevenfold change in Reynolds number for all five delta wing models. Theoretical estimates were made by three different methods: first, the straightforward TW–PM; second, TC–PM methods; and third, the GASP.

TW–PM estimates were made with the equations of reference 36 to determine the local flow deflection angles and the tables of reference 26 to obtain the corresponding oblique-shock and PM expansion pressure coefficients. The calculations were summed up to produce the normal force coefficients shown in figure 5 and, subsequently, the axial force coefficients labeled TW–PM. This simplified theoretical approach gave acceptable estimates of the normal force coefficients for the four delta wings having leading-edge sweep angles of 75° and 80° (figs. 5(a)–(d)), with the trend of a slight underprediction at low angles of attack and an overestimation at the higher angles. The exception was the estimates made for the 85° swept delta wing, model D5, with its inherent high degree of three dimensionality, the TW–PM theory grossly overpredicted the normal force at both low and high angles of attack. Greatly improved estimates were possible when the pressure coefficients derived for 3-D conical bodies (refs. 23, 24, and 25) were substituted for the oblique shock values of reference 26. Normal force coefficients obtained in this manner, labeled "TC–PM" in figure 5(e), show acceptable estimates at all angles of attack. This overprediction by the TW–PM theory is in contrast to the underprediction of C_N for the 2-D rectangular wing, model W1, which also had an aspect ratio of 0.35 and a common $V^{2/3}/S_p$ of 0.210.

The more exact calculations made with the GASP CFD program, shown by dashed lines in figure 5(a), provided excellent predictions of normal force coefficients with angle of attack and further proof that the coefficient is constant with Reynolds number. This program also showed that there were but minimal viscous effects on normal force for the thin delta wing. The GASP input grid used for delta wing model D1 is discussed in the section "Theoretical Methods" and shown in figure 14. Oil flows on wing models D1 and D5 are shown in figures 7(b) and (c). Slight inflow at the leading edges can be seen on model D1 at $\alpha = 7.0°$. The oil flow on the 85° swept wing model D5 was nearly conical even at the relatively high angle of attack of 8.5°. Therefore, the use of the TC–PM theory was justified for these engineering estimates. From the study of the experimental data and the theoretical results, however, the normal force

coefficients are constant with Reynolds number for delta planform 3-D bodies and that simple TW or TC pressure coefficients in conjunction with PM expansion coefficients may provide acceptable estimates of the normal force coefficients. More exact results were shown to be possible with the GASP CFD program.

Axial Force

The axial force coefficients were available for delta wing models D1 to D4 and are shown plotted against the laminar parameter $1/\sqrt{R_l}$ in figures 5(a)–(d), along with estimates of the inviscid values calculated by the methods described in the previous section "Normal Force." For all models, particularly for the two models that have high thickness ratios (figs. 5(c) and (d)), higher drag, and less scatter, the experimental data that faired to the inviscid values provide further evidence that this extrapolation method is sound. Inviscid calculations on model D1 (fig. 5(a)) with either TW–PM or GASP CFD methods gave nearly the same results. Experimental data were incrementally higher than the GASP viscid results and could not be accounted for, although errors in experimental base-pressure measurements are suspect. The GASP computations, however, further confirmed the second prime contention of this paper, which was that an extrapolation of the laminar viscid axial force coefficients to very high Reynolds numbers plotted against the laminar flow parameter $1/\sqrt{R_l}$ is rigorously valid from theoretical considerations.

Caret Wing

Normal Force

The caret model (fig. 2(d)) was designed with geometric characteristics similar to the 2-D rectangular wing model W4 (figs. 2(b) and 4(d)) and delta wing model D1 (figs. 2(c) and 5(a)). The three wings had a common aspect ratio of 1.07, and the leading-edge sweep was 75° for the caret and the delta wings. The volume ratio $V^{2/3}/S_p$ was held constant for the delta and rectangular wings; thus, the thickness ratio varied. The thickness ratio was held constant at 0.1163 for the caret wing to match the rectangular 2-D wing, and the negative dihedral angle was set to coincide with the leading-edge shock observed on the rectangular wing (fig. 4(d)) at its maximum lift-drag ratio, which occurred at an angle of attack of about 9° (ref. 14). Thus, the volume ratio geometrically had to vary when the thickness ratio was held constant. (See table and sketch in fig. 2(d).) Figure 6 shows that, as with the simpler shapes, the normal force coefficient is constant with Reynolds number at angles of attack up to 6°. There appears to be a slight trend for the coefficient to increase with Reynolds number at the higher angles of attack, a trend also exhibited by the

rectangular wing model W4 but not shown for any of the previous 11 simple shapes or the 3 subsequent more complicated aircraft configurations. Prediction of the normal force coefficients for the caret wing by the simple TW–PM theory are shown to be inadequate at all test angles of attack; this indicates that the flow, on the bottom surface particularly, is more complex than that of the other simple wings reported herein. Four angles of attack were run with the GASP CFD code with mixed results; C_N values decreased slightly with Reynolds number, which is contradictory to the experimental data and probably an indication of inadequate modeling of flows of the more 3-D shapes. The oil flow study shown in figure 7(d), however, indicates that the flow was orderly on both the top and bottom surfaces with a slight inflow just aft of the leading edges at the test angle of attack of 7.5°. The GASP input grid for the caret wing, discussed in general in the section "Theoretical Methods," is shown in figure 14 in abbreviated form. The conclusion may be made that the normal force coefficient for a simple caret wing is constant with Reynolds number.

Axial Force

The axial force coefficients were available for the lower angles of attack and are presented in figure 6. This somewhat more complicated aerodynamic shape exhibited the same laminar characteristic of extrapolating to the inviscid value at very high Reynolds numbers. These inviscid values were calculated by the same methods, TW–PM and GASP CFD, as were those of the delta wings described previously. The inviscid axial force coefficient for this unique configuration consists only of the pressure forces on the top surface because the bottom surface is parallel to the oncoming flow. The present experimental data were corrected for base pressure. Viscous axial forces therefore consist of pressure forces on the top surface and skin friction on both the top and bottom surfaces. These data thus provide additional evidence that the conclusion the extrapolation of low Reynolds number laminar data to high Reynolds numbers by the parameter $1/\sqrt{R_l}$ is valid. The inviscid axial force coefficients determined by the GASP CFD program were slightly lower than those determined by the TW–PM theory, a trend also shown for the delta wing (fig. 5(a)).

Viscous CFD and Engineering Estimates of Axial Force Coefficients at $\alpha = 0°$

Figure 8 was prepared to summarize and compare the viscous CFD and engineering axial force theories on the basic research models at an angle of attack of 0°. The methods of determining the pressure loadings and viscous forces were discussed in the section "Theoretical

Methods." Although estimates of the nose and leading-edge drag made by the modified Newtonian method of references 28 and 29 were not included in the CFD or engineering calculations where sharpness was assumed, they are included for each configuration for the maximum diameters considered possible. For reference, the sharp-body modified Newtonian theory is shown for the wing models where the $C_{p,\max} = \gamma + 1$ (ref. 30).

A cursory study of figure 8 gives the impression, with the exception of the axial force predictions for the $10°$ cone, that the present methods are inadequate in providing accurate axial force coefficients on simple research configurations at $M_\infty \approx 7.00$ under laminar flow conditions. If performance estimates were desired for flight under these conditions, the impression would be correct. However, the fact that the inviscid estimates of the GASP procedures for the cones were identical with those of references 23 to 25 and the engineering inviscid estimates for the faceted wings were close to those of GASP is possibly more important. Under viscid conditions, the GASP estimates that included the viscous interaction effects (i.e., the change in the surface pressure caused by the boundary-layer buildup and the change in the skin friction caused by this pressure change) were higher than the TW–PM + C_F estimates, which did not account for these viscous effects and was to be expected. Exact modeling of the flow is further complicated by the knowledge that the laminar skin friction increases with decreasing model wall temperature and the boundary-layer displacement thickness decreases with decreasing wall temperature (ref. 1). The assumption that the models had a constant wall temperature during the blowdown tunnel tests was incorrect, but the exact wall temperature was unknown, as was the temperature distribution. The regions near the model leading edges and the nose were quite possibly near the adiabatic wall temperature during the tests; these regions are where a large portion of the viscous interaction takes place.

The multiple calculations made by the GASP CFD program at various Reynolds numbers for each test model are shown to plot in a straight line that extrapolates back to the ordinate axis to intercept the inviscid or Euler value to give proof that the initial postulation, based on experimental data, was correct. This extrapolation provides further validation of the initial introductory premise that all the laminar viscous parameters and any combination of them may be expressed as functions of the reciprocal of the Reynolds number to the one-half power $1/\sqrt{R_l}$.

Hypersonic Cruise Configurations

Thus far, the present paper has presented only experimental data and theoretical estimates on relatively simple aerodynamic shapes that had simple bow shocks and no appendages downstream of the nose or leading edge to further disturb the flow. This paper now addresses the experimental results from three hypersonic cruise configurations at $M_\infty = 6.00$, 6.86, and 8.00.

Blended Body–Wing Configuration

The first blended body–wing transport airplane configuration shown in figure 2(e) was conceived during a NASA-Convair trade-off study of two hypersonic cruise configurations discussed in references 16 and 17 and tested at $M_\infty = 6.86$, Reynolds numbers based on body length from 1.36×10^6 to 4.36×10^6, and angles of attack from $0°$ to $12°$. The normal force data from these tests are presented in figure 9 for the complete configuration—body, blended wing with elevons, vertical tail, and scramjet engine inlet cowl—at elevon deflections from $0°$ to $-15°$ and with and without engine inlet cowl at $\delta_e = 0°$. The data for the complete configuration, BWEVI, were taken at four Reynolds numbers and for the configuration with elevon deflection and without inlet, BWEV, were taken at only the two extreme Reynolds numbers. The normal force coefficient is constant with Reynolds number at each angle of attack for the complete configuration (fig. 9(a)) and for the four geometric variations in figures 9(b) and (e). Of interest is the relatively low control power of the elevons, that is, the ability of the elevons to produce C_N with deflection, particularly at low angles of attack even though they encompassed about 10.2 percent of the reference area or, more importantly, about 14.4 percent of the wing outside the body (ref. 37). Although the addition of the engine inlet and/or the deflection of the elevon controls do affect the magnitude of the normal force coefficients as expected, they do not change their invariance with Reynolds number. For a relatively clean airplane configuration with various pitch control deflections, the normal force coefficients are constant with Reynolds numbers at a given attitude even though M_∞ varied from 6.76 to 6.89 at the lowest to the highest test Reynolds number.

Distinct Body–Wing–Tail Configuration

The distinct body-wing airplane configuration shown in figure 2(f) was the second design conceived during the NASA-Convair trade-off study of references 16 and 17. This complete configuration consists of the body, wing with ailerons and flaps, horizontal and vertical tails, and scramjet engine inlet cowl. The normal force coefficients at $\alpha = 0°$ to $12°$ are presented in figure 10. The tests were conducted at horizontal tail deflections of $-5°$, $0°$, and $+5°$. Tests were made with and without engine inlet cowl, at $\delta_H = 0°$ and $\beta = -5°$. The Reynolds numbers based on fuselage length varied from about 1.66×10^6 to 5.35×10^6. Four different

Reynolds numbers were used for the complete configuration, BWHVI, at $\delta_H = 0°$ and 5°, and the two extreme Reynolds numbers were used for other configuration variables. The normal force coefficient for this distinct body–wing airplane configuration was constant with variations of Reynolds number for all tests.

Advanced Blended Body–Wing Configuration Tested at $M_\infty \approx 8.00$

Normal force. Our last example test shape is a highly blended body–wing design (fig. 2(g)) derived from the previously discussed blended body–wing configuration designed during the trade-off studies of references 16 and 17. This blended body–wing configuration had a gross volume similar to the configurations shown in figures 2(e) and (f) but had revised elliptical fuel tanks with an eccentricity of about 2; thus, this resulted in a flatter fuselage. Tests were made without vertical tail and engine cowl. More details of the design philosophy can be found in reference 1. Although all these basic data for the tests on this model at $M_\infty \approx 8.00$ were presented in reference 1, only those data at $\alpha = 3°$ were examined in detail.

The present paper examines all the data at all angles of attack up to $\alpha = 6°$ from the Langley Mach 8 VDT and the Calspan Shock Tunnel. To obtain data at whole angles of attack, faired curves were used to determine some points. Figure 11(a) presents the normal force coefficients versus Reynolds number based on the theoretical length that is shown in figure 2(g) as dashed lines. Note that the Calspan Shock Tunnel data extended from a low Reynolds number of about 0.53×10^6 to a high of 161.0×10^6; the preliminary results were presented in reference 18. The data from the Mach 8 VDT were taken at $R_l \approx 1.51 \times 10^6$ to 27.1×10^6. Also, included in figure 11(a) are calculations made with TC–TW—PM theory and the Mark III Hypersonic Arbitrary-Body Aerodynamics Program of references 3 and 1. Two independent calculations were made because of the different model wall temperatures, which greatly affect the axial force, and the slightly different Mach numbers in the shock tunnel and the blowdown facility, which affect both the normal and axial forces. Because of the short run times, up to 13 ms, the model in the shock tunnel remained at approximately room temperature, whereas the model in the blowdown tunnel was exposed to the hot air (650°F to 830°F) for about 30 s and acquired a wall temperature of as much as 400°F.

As mentioned previously, the throat geometry was varied along with the stagnation conditions to provide the wide range of test Reynolds number with a minimum variation of Mach number in the Calspan Shock Tunnel. The Mach number varied approximately logarithmically with stagnation pressure from about 7.76 to 8.07 in the Mach 8 VDT. Primarily the variation in Mach number with test Reynolds number, which was accounted for in the calculations, made the difference in the normal force coefficients between the two test facilities presented in figure 11(a). The small increase in Mach number accounts for the slight decrease in both the experimental and the calculated normal force coefficients with Reynolds number. This variation with Mach number may be observed in plots of the inviscid C_N on simple flat plates with angle of attack and/or with the C_p on cones with cone angle. (See appendix B.) The trend indicates that the downward slope increases, that is, the rate of change of normal force coefficient decrease with Mach number increases with increasing flow deflection angle.

A study of figure 11(a) shows that the experimental normal force coefficients were nearly constant with 2.25 orders of magnitude variation in Reynolds number. These data from both facilities were recorded with natural transition under low Reynolds number, laminar boundary-layer conditions and extended up through transition to high Reynolds number, turbulent conditions. The highest Reynolds number recorded in the shock tunnel of about 161×10^6 is representative of a 300-ft-long vehicle traveling at $M_\infty = 8.00$ at an altitude of about 109000 ft. It appears the engineering calculations made by the HABAP predicted well the unchanging normal force coefficient with Reynolds number, but this code underpredicted the coefficients at the higher angles of attack. Therefore, the normal force coefficients of this streamlined body–wing configuration were constant with Reynolds number.

Axial force. The axial force coefficients for the advanced blended body–wing configuration at a nominal Mach number of 8 are presented in figure 11(b) from both the Langley Mach 8 blowdown tunnel and the Calspan Shock Tunnel. These data are plotted against the laminar parameter $1/\sqrt{R_l}$ in the left plot and a turbulent parameter $1/\sqrt[7]{R_l}$ in the right plot for the various test angles of attack. The difference in the magnitudes of the data between the Langley and Calspan facilities is caused by the large variation in stagnation temperature and the wide variation in model wall temperatures between the two tunnels (ref. 1). These variations resulted in ratios of model wall to stagnation temperature of above 0.64 for the Mach 8 VDT and about 0.16 for the Calspan Shock Tunnel. The higher wall temperature ratio of the model in the VDT along with the lower static temperature resulted in higher basic skin friction, a thicker boundary layer, greater induced pressures, and a greater increment of change in skin friction caused by these surface pressure changes than occurred on the same model with a cold wall in the Calspan Shock Tunnel.

These variations of axial force coefficients between the two test facilities were discussed at length in reference 1, but it is important to note that the identical configuration can have different total axial force coefficients at the same Reynolds number and Mach number because of the different wall temperatures of the model in different test regimes. The data at low Reynolds number (higher values of $1/\sqrt{R_l}$) were shown to have been easily extrapolated to the inviscid axial-force value determined by the HABAP of reference 3. These inviscid values of axial force coefficient include the pressure drag from the HABAP calculations, the axial force caused by the rounded leading edges of the wings and the nose of the body, and a wing trailing-edge base pressure coefficient of $-1/M_\infty^2$ (ref. 27). The inviscid axial force coefficient may be determined for this advanced blended body–wing configuration by extrapolation of laminar-flow viscous data to very high Reynolds number with the parameter $1/\sqrt{R_l}$. Once the inviscid axial force coefficients have been determined from laminar experimental results, the turbulent parameter $1/\sqrt[7]{R_l}$ may be determined as described in reference 1. The right plot of figure 11(b) shows the same data plotted against this turbulent parameter. The value of the root, 7 in this case, may not apply to all configurations because of different component geometry and different local Reynolds numbers. Without laminar data, with the known root of 2, determination of the inviscid axial force coefficient would be highly speculative. The present turbulent data obtained at the higher Reynolds numbers (lower values of $1/\sqrt[7]{R_l}$ are shown to readily extrapolate to the inviscid value determined from the laminar results. Again, the mixed-flow region and the laminar data are faired with dashed lines. The intersection of the solid and dashed lines represents a theoretical point of instant transition, but it is plotted at the same Reynolds number in both the laminar and turbulent plots for consistency and study. The inviscid axial force coefficient or wave drag may be determined for a highly streamlined body–wing concept by extrapolating the laminar axial force coefficients to the ordinate by using the laminar parameter $1/\sqrt{R_l}$ as the abscissa.

Advanced Blended Body–Wing Configuration Tested at $M_\infty \approx 6.00$

The advanced blended body–wing configuration was also tested in the Langley 20-Inch Mach 6 Tunnel and the results were reported in reference 2. The normal force coefficients have been replotted against Reynolds number based on the theoretical length of the model (shown in fig. 2(g)) in figure 12 at angles of attack up to 8°. For these tests, the Mach number varied from about 5.799 to 5.994 through the test Reynolds number range of about 1.563 × 10⁶ to 18.985 × 10⁶. In reference 2, the tests were made under turbulent boundary-layer conditions. These data are shown along with TC–TW—theory applied with the HABAP of reference 3. The TC-TW theory predicts the normal force coefficients adequately at low angles of attack but tends to overpredict at the higher angles. Other than the slight decrease of the coefficients with the slight increase of Mach number, which is more pronounced as the angle of attack increases (discussed in appendix B), the normal force coefficients are constant with the variation of more than 1 order of magnitude of Reynolds number under turbulent boundary-layer conditions. The normal force coefficients of a highly blended body–wing configuration at $M_\infty = 6.00$ are constant with Reynolds number.

Additional experimental results at $M_\infty = 0.36$, 1.50, 2.00, 2.36, 2.86, and 6.00 on a similar aluminum configuration that has a vertical tail, engine inlet cowl, and variable elevon deflections may be found in reference 38 for $R_l = 9.4 × 10^6$ for $M_\infty = 0.36$; $R_l = 6.67 × 10^6$ for $M_\infty = 1.50$, 2.00, 2.36, and 2.86; and $R_l = 21.6 × 10^6$ for $M_\infty = 6.00$.

Space Shuttle Orbiter

Of significance are the experimental wind tunnel and flight data reported in reference 39 with variations of Mach numbers and Reynolds number on the Space Shuttle orbiter with body flap deflections of 0° and 16° and angles of attack up to 45°. These data show that the normal force coefficients were constant with Reynolds number at $M_\infty = 6.00$ and $M_\infty \approx 10.00$ in the wind tunnel and, more importantly, in flight. This result indicates that the real gas effects occurring in flight do not alter the conclusion of the constancy of C_N with Reynolds number. These data also show that normal force data recorded in a helium tunnel at $M_\infty = 18$ were constant with Reynolds number and varied little from data measured during flight.

Conclusions

An analysis of experimental data performed with current computational fluid dynamics (CFD) and engineering theoretical methods of 25 configurations varying from simple conical shapes and varying slab-sided wings to complex complete configurations tested at free-stream Mach numbers M_∞ of about 6.00, 7.00, and 8.00, in 4 distinctly different hypersonic facilities, through a range of Reynolds number based on body length R_l from 0.348 × 10⁶ to 160.7 × 10⁶ leads to the following conclusions:

1. The normal force coefficient C_N is constant with Reynolds number for a given hypersonic Mach number

and constant angles of attack and sideslip under combined laminar, transitional, and turbulent boundary-layer conditions for both simple and complex configurations.

2. The results of CFD predictions on five simple aerodynamic shapes confirm that the normal force coefficient of a given configuration is constant with Reynolds number at a fixed angular attitude and Mach number.

3. Because of the invariance of normal force coefficient with Reynolds number, the inviscid C_N (very high Reynolds number) is an excellent estimate of the viscid values of normal force coefficient.

4. The wave drag or inviscid axial force coefficient C_A may be determined from laminar experimental data recorded at various Reynolds numbers by extrapolation and utilization of the laminar parameter $1/\sqrt{R_l}$; thus, tests of new hypersonic configurations would be desirable, if not mandatory, under all laminar boundary-layer conditions so that possible comparisons could be made with Euler CFD computations.

5. The results of CFD studies confirm that the axial force coefficients plotted against the laminar parameter $1/\sqrt{R_l}$ will extrapolate as straight lines back to the Euler or inviscid values on the ordinate axes.

6. The present General Aerodynamic Simulation Program (GASP) CFD program provided identical inviscid axial and normal force coefficients as published in the past analytical studies of Kopal, Sims, and Jones (MIT Tech. Rep. 1, NASA SP-3004, and AGARD-AG-137) on right circular cones.

7. The viscid axial force coefficients provided by the GASP CFD program under laminar conditions were excellent for the cone with semivertex angle of 10° at $M_\infty = 6.86$ but were underpredicted for all other configurations at all Reynolds numbers.

8. When both laminar and turbulent experimental data are available on the same configuration, it is possible that both may be extrapolated to very high Reynolds numbers.

9. The Mark III Hypersonic Arbitrary-Body Aerodynamics Program with present Langley modifications provided excellent inviscid axial and normal force coefficients for a hypersonic blended body–wing concept.

10. It is unknown if the invariance of C_N with Reynolds number and the ability to extrapolate C_A to very high Reynolds number with the laminar parameter $1/\sqrt{R_l}$ extend to lower supersonic Mach numbers.

11. Within the accuracy of the experimental data no difference between data recorded on steel models and data recorded on aluminum models was discernible.

Appendix A

Wind Tunnel Model Size Determination

A semiempirical method was developed in the Langley 11-Inch Hypersonic Tunnel to determine the size of a test model that would ensure tunnel starting and running. This method consisted of the determination of the largest circular disk, mounted perpendicular to the flow, that would allow the tunnel to start and run with a good wake, a clear shock pattern downstream of the disk, and no nozzle roof or floor flow separation. A disk with diameter of 2.865 in. would run at $M_\infty = 6.86$ and a Reynolds number based on disk diameter of 0.447×10^6, and a disk with diameter of 2.50 in. would run at $M_\infty = 9.60$ and a Reynolds number of 0.20×10^6. Force measurements were made during the experiments, and the disk drag was determined in pounds. The selection of model size was then made by estimating the anticipated drag, that force parallel to the flow, at the highest desired angle of attack of the new model and sizing it to not exceed that of the test circular disk. In some instances, the newly sized model might extend into the boundary layer on the ceiling or floor of the test section, then the length or the angle of attack would have to be reduced. Several attempts were made to correlate these data with other supersonic and hypersonic facilities. One early effort divided the test disk diameter by the test section height minus 1 boundary-layer thickness; therefore, δ^*, the boundary-layer displacement thickness, was assumed to be 0.5δ, the total boundary-layer thickness, and the boundary layer was assumed to be of constant thickness on all test walls. These assumptions, of course, are not true particularly for square or rectangular test sections. A better correlation parameter was found to be the height of the effective test section flow determined by using the nozzle first minimum area and the calibrated test Mach number. The effective test section cross-sectional area may be obtained from the compressible flow tables. The disk diameter was then divided by the square root of this effective test section area for rectangular cross-section test sections or by the diameter of the circle having the effective cross section area for circular test sections. Figure 15 shows results of this correlation for the 11-Inch Tunnel and other Langley and Jet Propulsion Laboratory facilities. This figure shows the ratio of disk diameter d to the effective test section flow height H_e versus calibrated free-stream Mach number, with the Langley values being $d/H_e \approx 0.31$. The JPL values of reference 40 are somewhat lower, probably because of strut and sting size and geometry. All models discussed in the present report were sized by using these criteria except the advanced blended body–wing configuration tested at $M_\infty = 6.00$ and 8.00. Inviscid theory calculations were made by the method presented in reference 41. Larger disks might be expected for higher Reynolds numbers and/or smaller support structures.

The difference between the effective test section area and the geometric area is the absolute displacement boundary-layer area and, if distributed evenly over the walls of the test section, would be an estimate of the average boundary-layer displacement thickness δ^*.

Appendix B

Rate of Change of Pressure Forces on Flat Plates and Cones With M_∞ and Flow Deflection

The relationship of pressure forces on simple flat surfaces and conical bodies is fundamental to the understanding of the normal force on multisurface models and complex models of full-scale aircraft configurations. A cross plot of these relationships is presented in figures 16 and 17. Figure 16 shows the normal force (i.e., the sum of pressure forces on both bottom and top surfaces) in coefficient form of an infinite-span flat wing at hypersonic Mach numbers from 5.00 to 9.00 and at angles of attack up to 10° from the tables of reference 26. Shown also are variations of surface pressure coefficients on right circular cones at $\alpha = 0°$ for cone semivertex angles up to 14° with Mach number (refs. 23 to 25). Figure 17

presents a breakdown of the pressure coefficients on the windward or compression and leeward or expansion surfaces of the flat wing of figure 16. In each figure, the same phenomenon may be observed (i.e., as the Mach number increases, C_N and C_p decrease with Mach number). Furthermore, this decrease with Mach numbers is exacerbated with increased flow compression or expansion that occurs with increased angle of attack.

This change in pressure forces provides a ready explanation as to why the normal force coefficient showed a slight decrease with increasing Reynolds number when all tests were made in the same test facility. When the Reynolds number is increased in a given wind tunnel, the tunnel wall boundary layer thins and the average free-stream Mach number increases; small decreases in normal force coefficient follow. As previously noted, this change in C_N was most noticeable at the higher angles of attack.

References

1. Penland, Jim A.; Marcum, Don C., Jr.; and Stack, Sharon H.: *Wall-Temperature Effects on the Aerodynamics of a Hydrogen-Fueled Transport Concept in Mach 8 Blowdown and Shock Tunnels*. NASA TP-2159, 1983.

2. Penland, Jim A.; and Marcum, Don C., Jr.: *Effect of Reynolds Number Variation on Aerodynamics of a Hydrogen-Fueled Transport Concept at Mach 6*. NASA TP-2728, 1987.

3. Gentry, Arvel E.: *Hypersonic Arbitrary-Body Aerodynamic Computer Program: Mark III Version—Volume I User's Manual*. Rep. DAC 61552, Vol. 1, McDonnell Douglas Corp., Apr. 1968. (Available from DTIC as AD 851811.)

4. Daum, Fred L.; and Gyarmathy, George: Condensation of Air and Nitrogen in Hypersonic Wind Tunnels. *AIAA J.*, vol. 6, no. 3, Mar. 1968, pp. 458–465.

5. McLellan, Charles H.; Williams, Thomas W.; and Bertram, Mitchel H.: *Investigation of a Two-Step Nozzle in the Langley 11-Inch Hypersonic Tunnel*. NACA TN 2171, 1950.

6. McLellan, Charles H.; Williams, Thomas W.; and Beckwith, Ivan E.: *Investigation of the Flow Through a Single-Stage Two-Dimensional Nozzle in the Langley 11-Inch Hypersonic Tunnel*. NACA TN 2223, 1950.

7. Bertram, Mitchel H.: *Exploratory Investigation of Boundary-Layer Transition on a Hollow Cylinder at a Mach Number of 6.9*. NACA Rep. 1313, 1957. (Supersedes NACA TN 3546.)

8. Neal, Luther Jr.: *A Study of the Pressure, Heat Transfer, and Skin Friction on Sharp and Blunt Flat Plates at Mach 6.8*. NACA TN D-3312, 1966.

9. *Hypersonic Shock Tunnel—Description and Capabilities*. Calspan, Sept. 1975.

10. Keyes, J. Wayne: *Force Testing Manual for the Langley 20-Inch Mach 6 Tunnel*. NASA TM-74026, 1977.

11. Penland, Jim A.: *Aerodynamic Force Characteristics of a Series of Lifting Cone and Cone-Cylinder Configurations at a Mach Number of 6.83 and Angles of Attack up to 130°*. NASA TN D-840, 1961.

12. Penland, Jim A.: *A Study of the Stability and Location of the Center of Pressure on Sharp, Right Circular Cones at Hypersonic Speeds*. NASA TN D-2283, 1964.

13. Penland, Jim A.: *Effect of Body Nose Blunting, Control Planform Area, and Leading-Edge Bluntness on Aerodynamic Control of a 5° Semivertex Cone at Mach Number 6.9*. NASA TN D-3460, 1966.

14. Penland, Jim A.: *Maximum Lift-Drag-Ratio Characteristics of Rectangular and Delta Wings at Mach 6.9*. NASA TN D-2925, 1965.

15. Becker, John V.: Studies of High Lift/Drag Ratio Hypersonic Configurations. *Proceedings of the 4th Congress of the International Council of Aeronautical Sciences*, Robert R. Dexter, ed., Spartan Books, 1965.

16. *Conference on Hypersonic Aircraft Technology*. NASA SP-148, 1967.

17. Penland, Jim A.; Edwards, Clyde L. W.; Witcofski, Robert D.; and Marcum, Don C., Jr.: *Comparative Aerodynamic Study of Two Hypersonic Cruise Aircraft Configurations Derived From Trade-Off Studies*. NASA TM X-1436, 1967.

18. Penland, J. A.; and Romeo, D. J.: Advances in Hypersonic Exploration Capability—Wind Tunnel to Flight Reynolds Number. *J. Aircr.*, vol. 8, no. 11, Nov. 1971, pp. 881–884.

19. Walters, Robert W.; Cinnella, Pasquale; and Slack, David C.: Characteristic-Based Algorithms for Flows in Thermochemical Nonequilibrium. *AIAA J.*, vol. 30, no. 5, May 1992, pp. 1304–1313.

20. Walters, Robert W.: GASP—A Production Level Navier-Stokes Code Including Finite-Rate Chemistry. *4th Annual Review Meeting of the Center for Turbomachinery and Propulsion Research*, Apr. 1990.

21. McGrory, W. D.; Huebner, L. D.; Slack, D. C.; and Walters, R. W.: Development and Application of GASP 2.0. AIAA-92-5067, Dec. 1992.

22. Vigneron, Y. C.; Tannehill, J. C.; and Rakich, J. V.: Calculation of Supersonic Viscous Flow Over Delta Wings With Sharp Subsonic Leading Edges. AIAA-78-1137, July 1978.

23. Jones, D. J.: *Tables of Inviscid Supersonic Flow About Circular Cones at Incidence, $\gamma = 1.4$*. AGARDograph 137, Nov. 1979.

24. Sims, Joseph L.: *Tables for Supersonic Flow Around Right Circular Cones at Zero Angle of Attack*. NASA SP-3004, 1964.

25. Massachusetts Institute of Technology Department of Electrical Engineering (Zdenek Kopal, leader): *Tables of Supersonic Flow Around Cones*. MIT Tech. Rep. 1, Cambridge, 1947.

26. Malvestuto, Frank S., Jr.; Sullivan, Phillip J.; Marcy, William L.; Mortzschky, Herbert A.; Larrivee, Jules A.; and Higgins, Vivan E.: *Study To Determine Aerodynamic Characteristics on Hypersonic Re-Entry Configurations. Part II—Analytical Phase, Volume 2—Design Charts*. Tech. Rept. WADD-TR-61-56, Pt. II, Vol. 2, U.S. Air Force, Aug. 1962.

27. Mayer, John P.: *A Limit Pressure Coefficient and an Estimation of Limit Forces on Airfoils at Supersonic Speeds*. NACA RM L8F23, 1948.

28. Penland, Jim A.: *Aerodynamic Characteristics of a Circular Cylinder at Mach Number 6.86 and Angles of Attack up to 90°*. NACA RM L54A14, 1954.

29. Penland, Jim A.: *Aerodynamic Characteristics of a Circular Cylinder at Mach Number 6.86 and Angles of Attack up to 90°*. NACA TN-3861, 1957.

30. Laitone, Edmund V.: Exact and Approximate Solutions of Two-Dimensional Oblique Shock Flow. *J. Aero. Sci.*, vol. 14, no. 1, Jan. 1947, pp. 25–41.

31. Monaghan, R. J.: *An Approximate Solution of the Compressible Laminar Boundary Layer on a Flat Plate*. R. & M. 2760, British A.R.C., 1953.

32. Eckert, Ernest R. G.: *Survey on Heat Transfer at High Speeds*. WADC Tech. Rep. 54-70, U.S. Air Force, Apr. 1954.

33. Huebner, L. D.; Pittman, J. L.; and Dilley, A. D.: Hypersonic Parabolized Navier-Stokes Code Validation on a Sharp-Nose Cone. *J. Aircr.*, vol. 26, no.7, July 1989, pp. 650–656.

34. Kussoy, M. I.: Drag Measurements of Cones in the Rarefield Flow Regime. *AIAA J.*, vol. 5, no. 10, Oct. 1967, pp. 1901–1902.

35. Liepmann, H. W.; and Roshko, A.: *Elements of Gasdynamics*. John Wiley & Sons, Inc., 1957.

36. Malvestuto, Frank S., Jr.; Sullivan, Phillip J.; Marcy, William L., et al.: *Study To Determine Aerodynamic Characteristics on Hypersonic Re-Entry Configurations. Part II—Analytical Phase, Volume I—Analysis*. WADD-TR-61-56, Pt. II, Vol. I, U.S. Air Force, Mar. 1962.

37. Penland, Jim A.; and Pittman, James L.: *Aerodynamic Characteristics of a Distinct Wing-Body Configuration at Mach 6*. NASA TP-2567, 1985.

38. Ellison, James C.: *Investigation of the Aerodynamic Characteristics of a Hypersonic Transport Model at Mach Numbers to 6*. NASA TN D-6191, 1971.

39. Brauckmann, G. J.; Paulson, J. W., Jr.; and Weilmuenster, K. J.: Experimental and Computational Analysis of Shuttle Orbiter Hypersonic Trim Anomaly. J. Spacecr. & Rocket, vol. 32, no. 5, Sept.–Oct. 1995, pp. 758–764.

40. *Jet Propulsion Laboratory Wind Tunnel Facilities*. Tech. Memo. 33-335, JPL, California Inst. Technol., Apr. 1967.

41. Lindsey, Walter F.; and Chew, William L.: T*he Development and Performance of Two Small Tunnels Capable of Intermittent Operation at Mach Numbers Between 0.4 and 4.0*. NACA TN-2189, 1950.
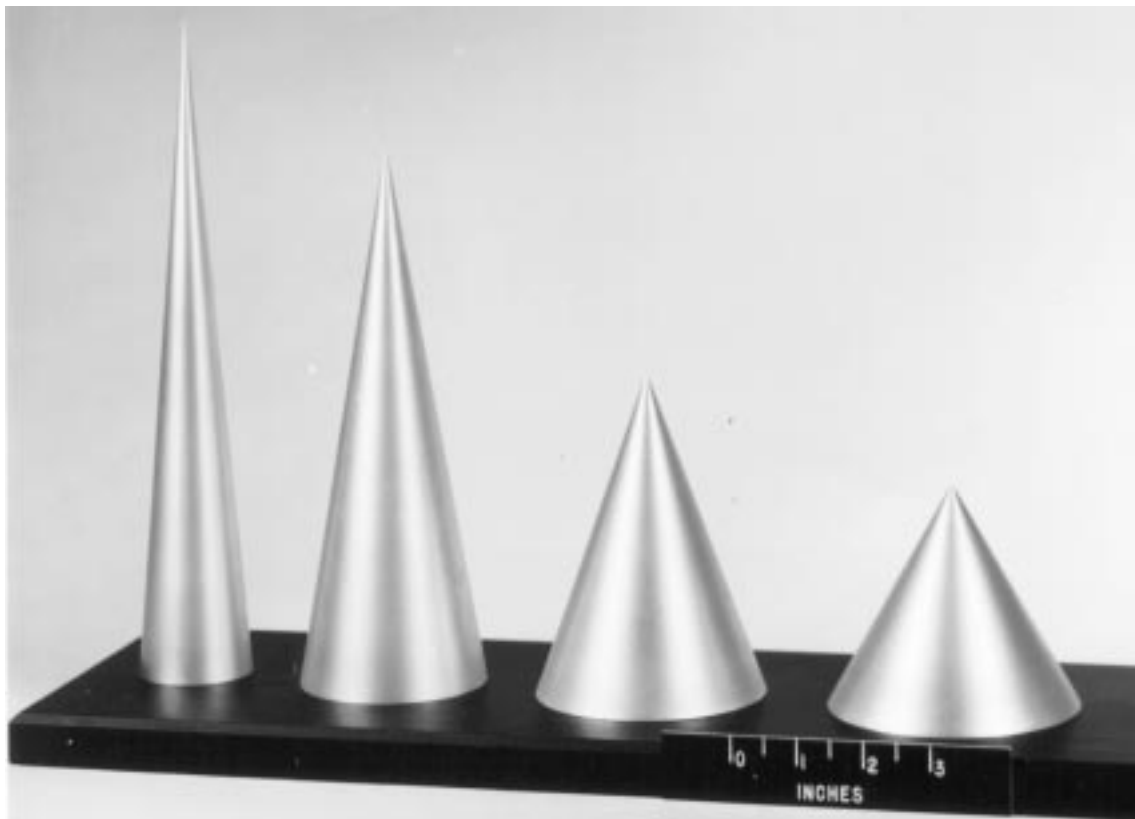
(a) Right circular cones.
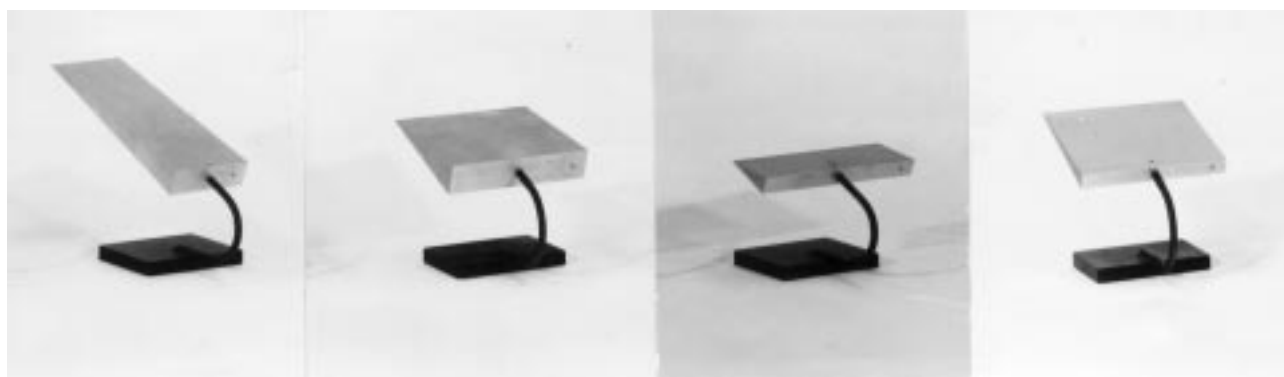
W1　　　　　　　W2　　　　　　　W3　　　　　　　W4

(b) Rectangular wings.

Figure 1. Models.

D1   D2   D3   D4   D5

(c) Rooftop delta wings.

(d) Caret wing.

Figure 1. Continued.

(e) Distinct body–wing–horizontal tail and blended body–wing configurations.

Figure 1. Continued.

(f) Advanced blended body–wing configuration.

Figure 1. Concluded.
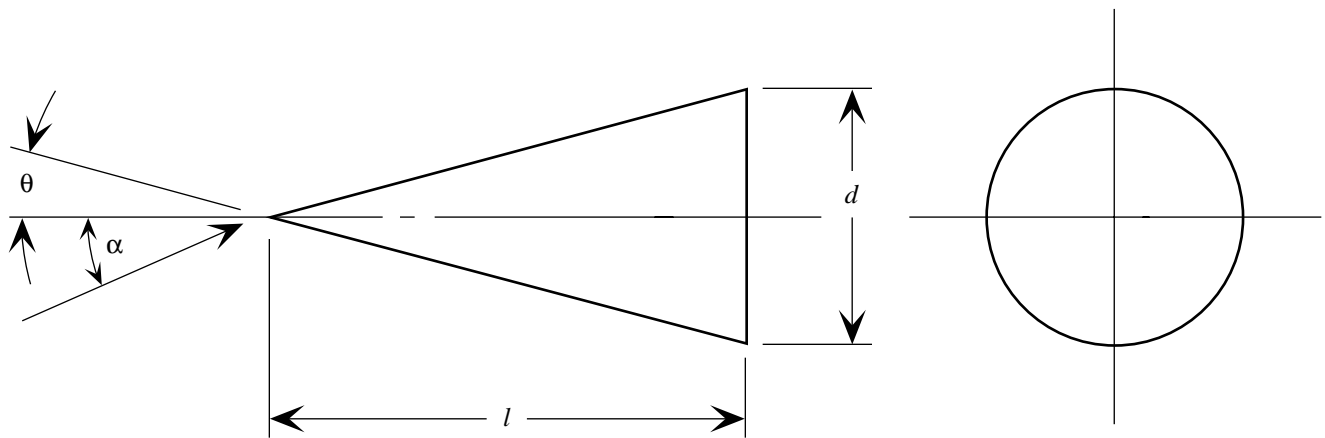
Model	θ, deg	l, in.		d, in.	
		Steel	Aluminum	Steel	Aluminum
C1	5	5.000 and 10.500	10.500	0.875 and 1.838	1.838
C2	10	3.365	8.500	1.189	2.997
C3	20	2.343	5.000	1.704	3.640
C4	30	1.861	3.400	2.149	3.926

(a) Cone models.

Figure 2. Detailed drawings showing dimensions of models.
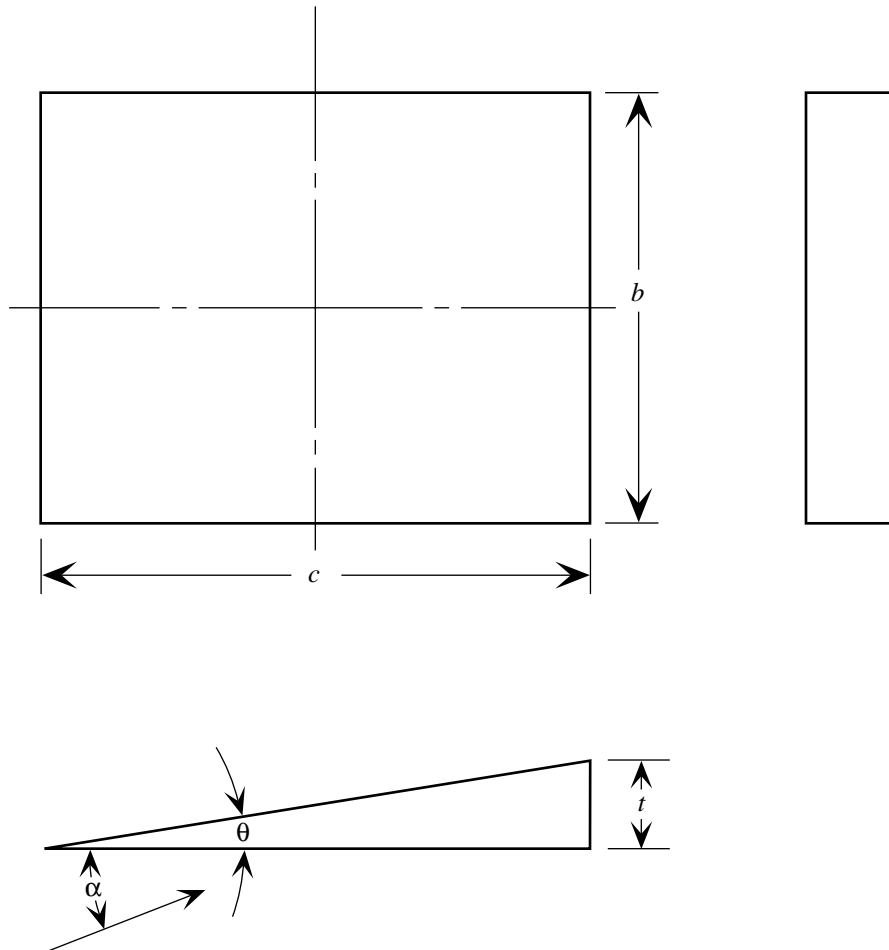
Model	θ, deg	b, in.	c, in.	t, in.	S_p, in^2	S_b, in^2	V, in^3	$V^{2/3}/S_p$	t/c	A
W1	6.37	2.899	8.290	0.923	24.0	2.68	11.084	0.210	0.111	0.35
W2	13.18	5.070	4.734	1.108	24.0	5.62	13.293	.234	.234	1.07
W3	17.22	6.000	2.000	.620	12.0	3.72	3.72	.200	.31	3.00
W4	6.63	5.070	4.734	.551	24.0	2.79	6.612	.147	.116	1.07

(b) Rectangular wings.

Figure 2. Continued.
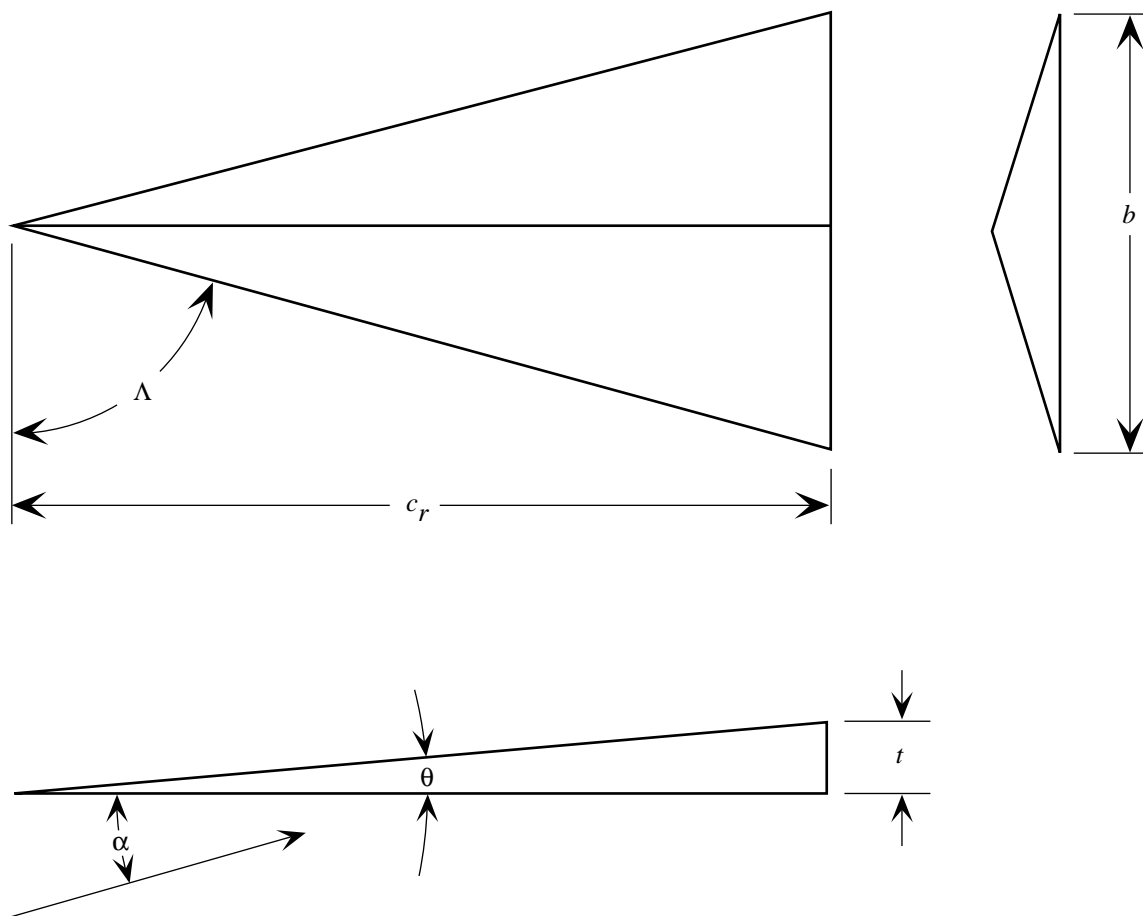
Model	θ, deg	Λ, deg	b, in.	c_r, in.	t, in.	S_p, in^2	S_b, in^2	V, in^3	$V^{2/3}/S_p$	t/c_r	A
D1	5	75	6.431	12	1.050	38.59	3.376	13.5	0.147	0.088	1.07
D2	5	80	4.231	12	1.050	25.49	2.221	8.9	.168	.088	.702
D3	10	75	6.431	12	2.116	38.59	6.800	27.2	.234	.176	1.07
D4	10	80	4.231	12	2.116	25.49	4.475	17.9	.268	.176	.702
D5	5	85	2.100	12	1.050	12.60	1.103	4.4	.210	.088	.35

(c) Rooftop delta wings.

Figure 2. Continued.

Model	θ, deg	$V^{2/3}/S_p$	t/c	A
W4	6.63	0.147	0.1163	1.07
D1	5.0	.147	.088	1.07
Caret	6.63	.178	.1163	1.07

15°

5.072

Shock

1.101

6.634°

6.50°

1.079

α

9.464
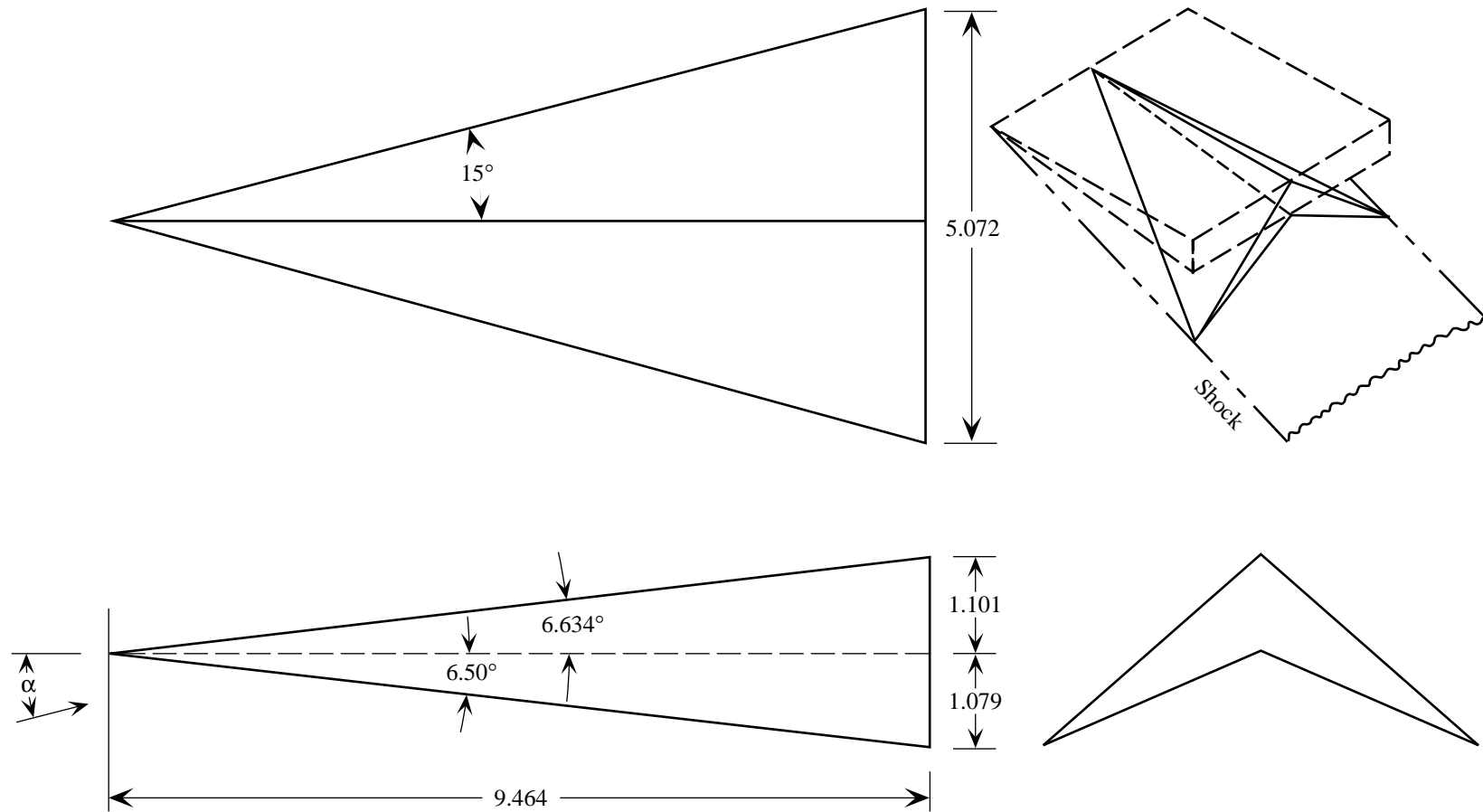
(d) Caret wing.

Figure 2. Continued
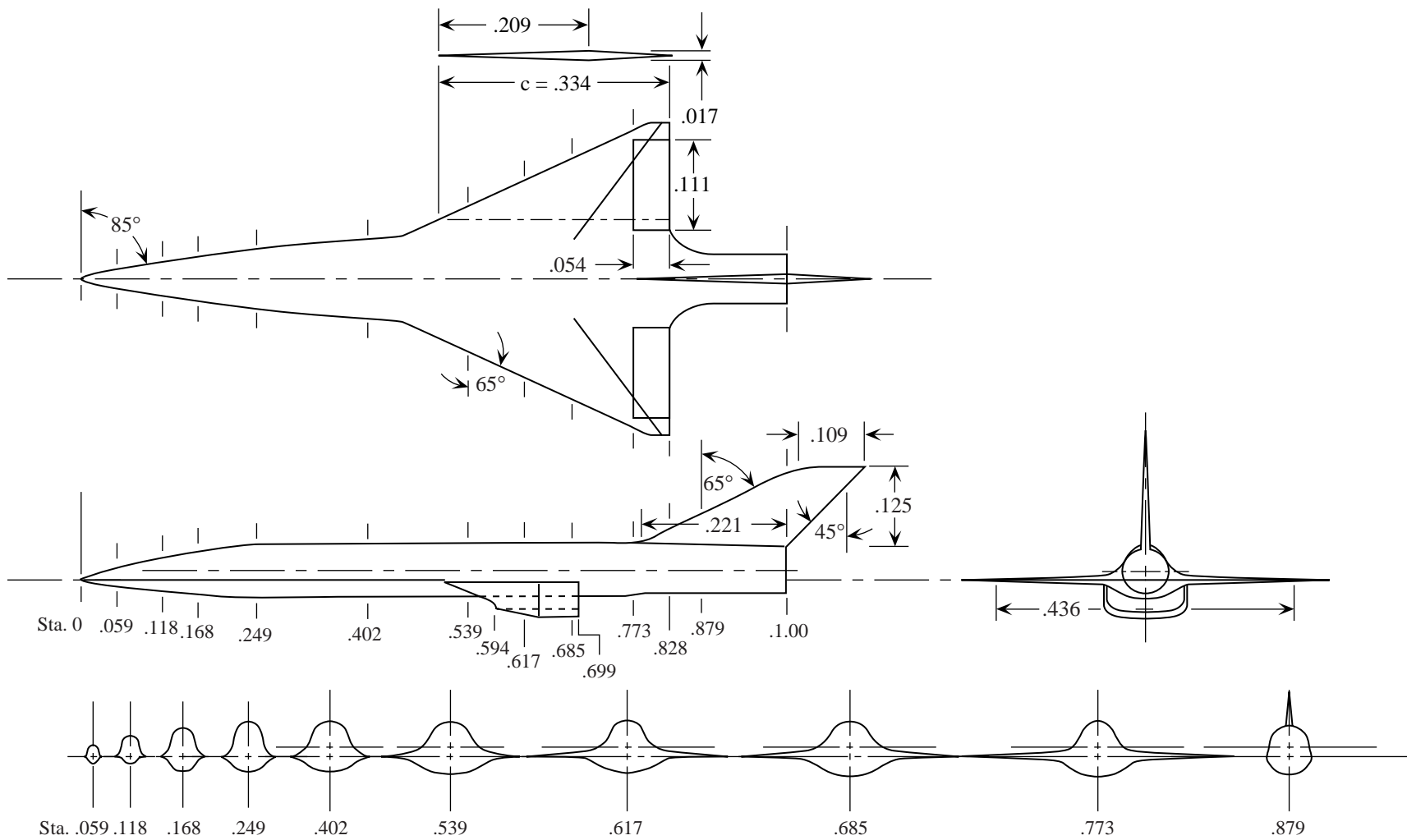
(e) Blended body–wing hypersonic cruise configuration; dimensions normalized by body length l of 14.00 in.

Figure 2. Continued.
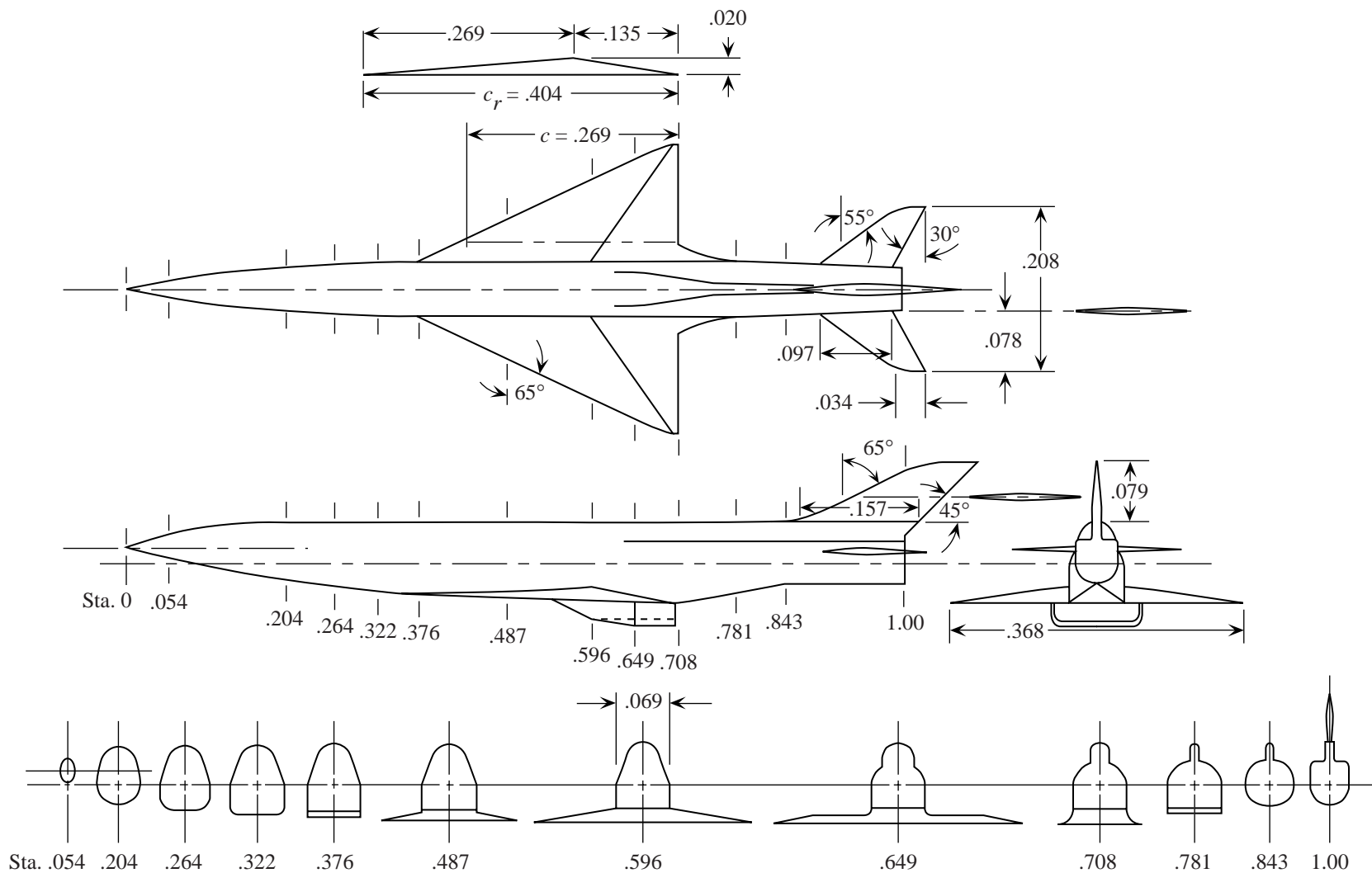
(f) Distinct body–wing–tail hypersonic cruise configuration; dimensions normalized by body length l of 16.64 in.

Figure 2. Continued.
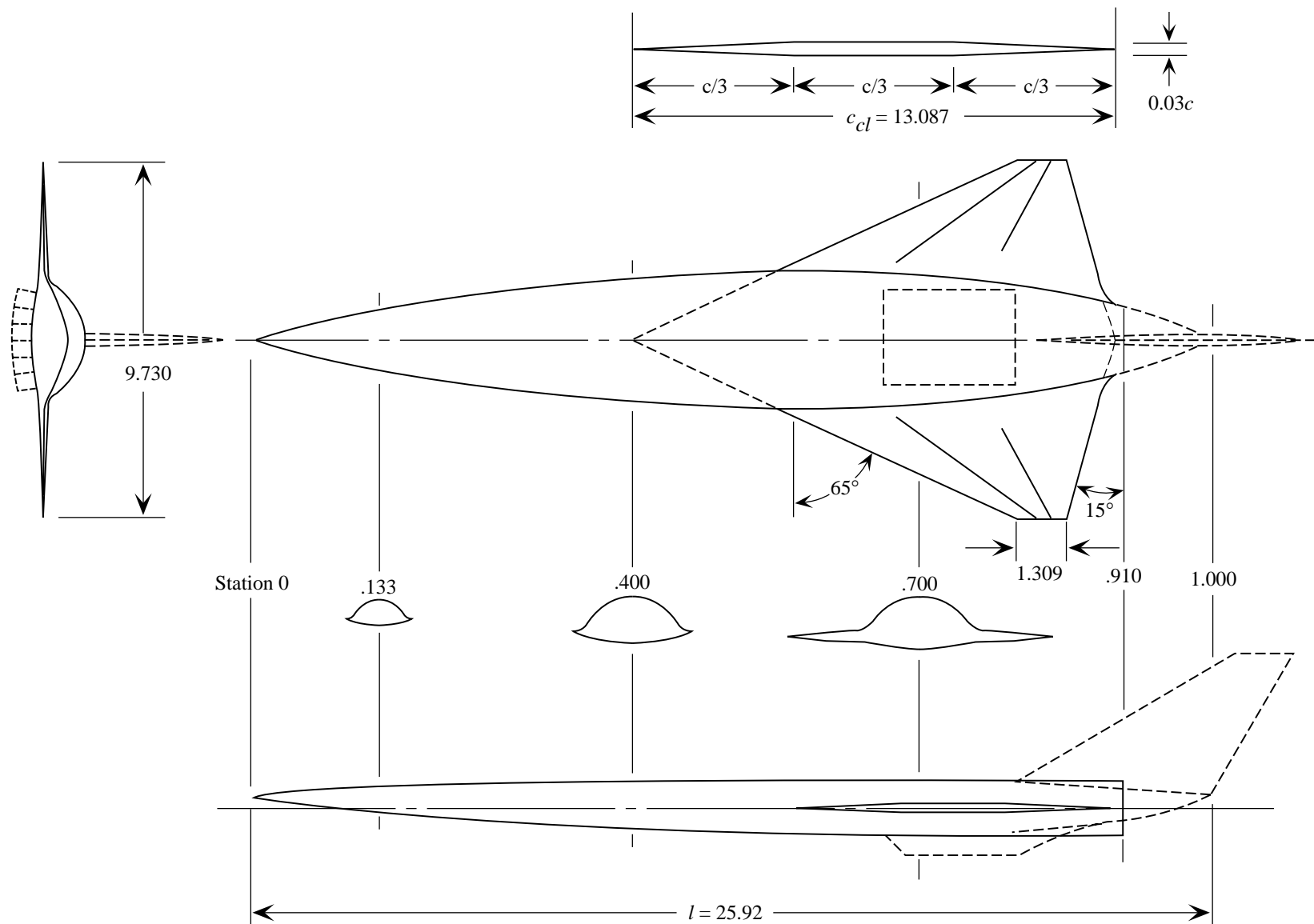
(g) Advanced blended body–wing hypersonic cruise configuration; linear dimensions are in inches; dashed lines show components not in present test.

Figure 2. Concluded.
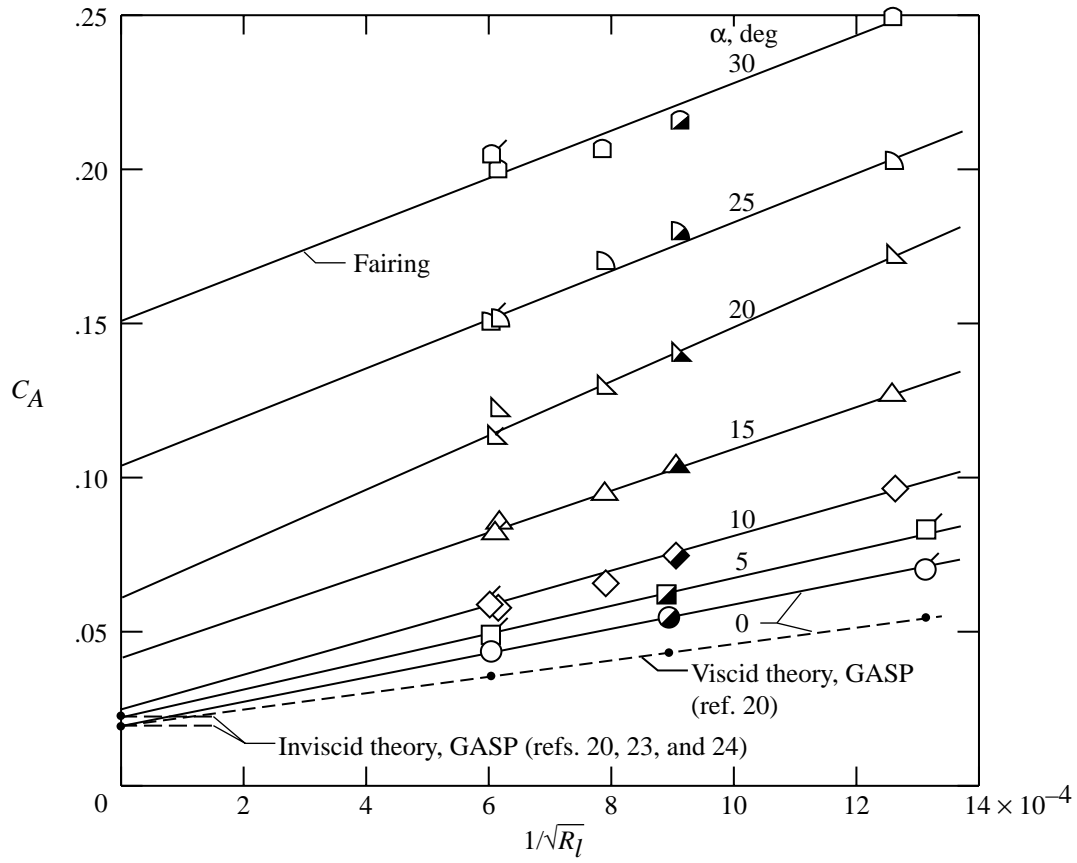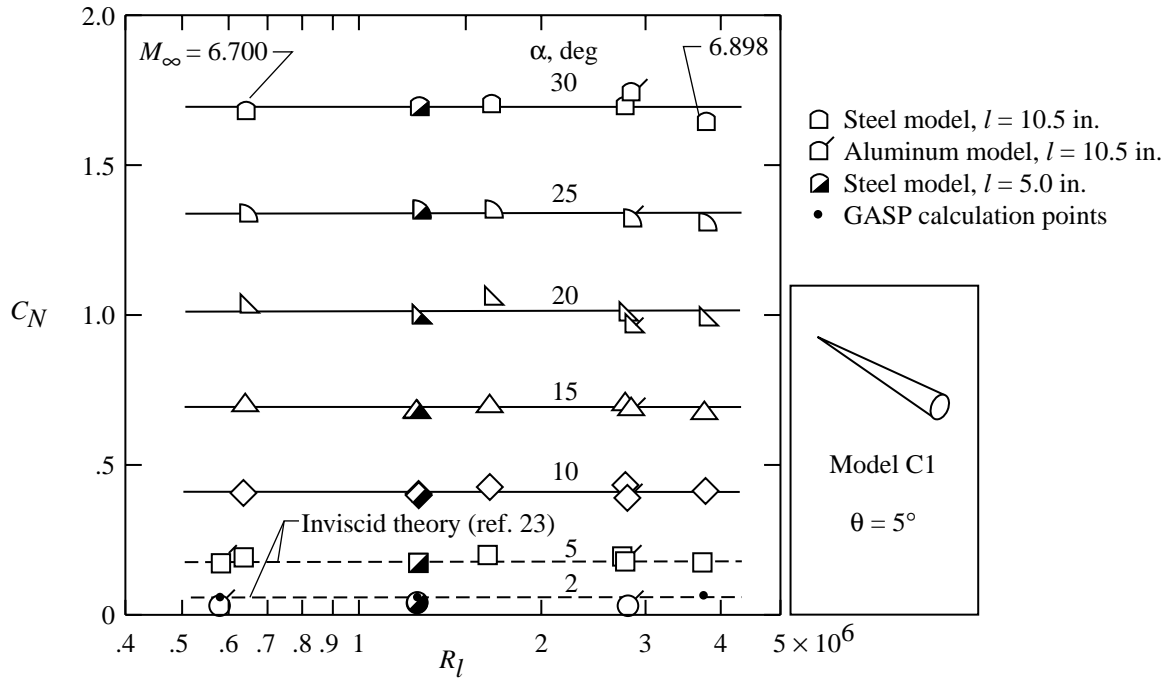
(a) Model C1; $\theta = 5°$.
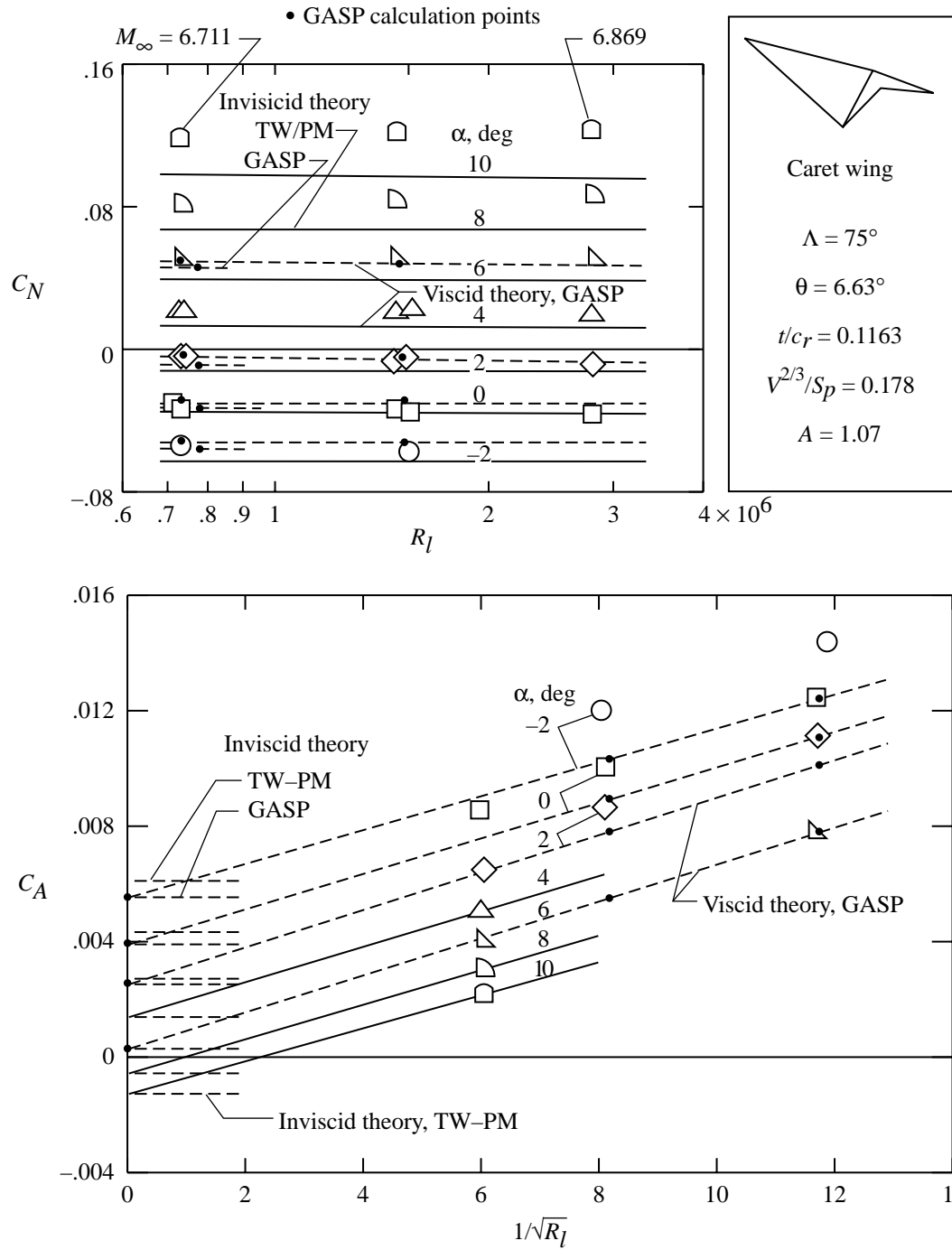
Figure 3. Variation of normal force and axial force coefficients with Reynolds number at $M_\infty \approx 6.86$ for cones.

○ Steel model, l = 3.365 in.
⊘ Aluminum model, l = 8.5 in.
• GASP calculation points

α, deg

C_N

Viscid theory,
GASP
(ref. 20)

Inviscid theory (ref. 23)

25

20

15

10

4

R_l

Model C2

$\theta = 10°$

α, deg

C_A

Fairing

Viscid theory, GASP
(ref. 20)

Inviscid theory,
GASP (refs. 20
and 23)

20

15

10

4

0

$1/\sqrt{R_l}$
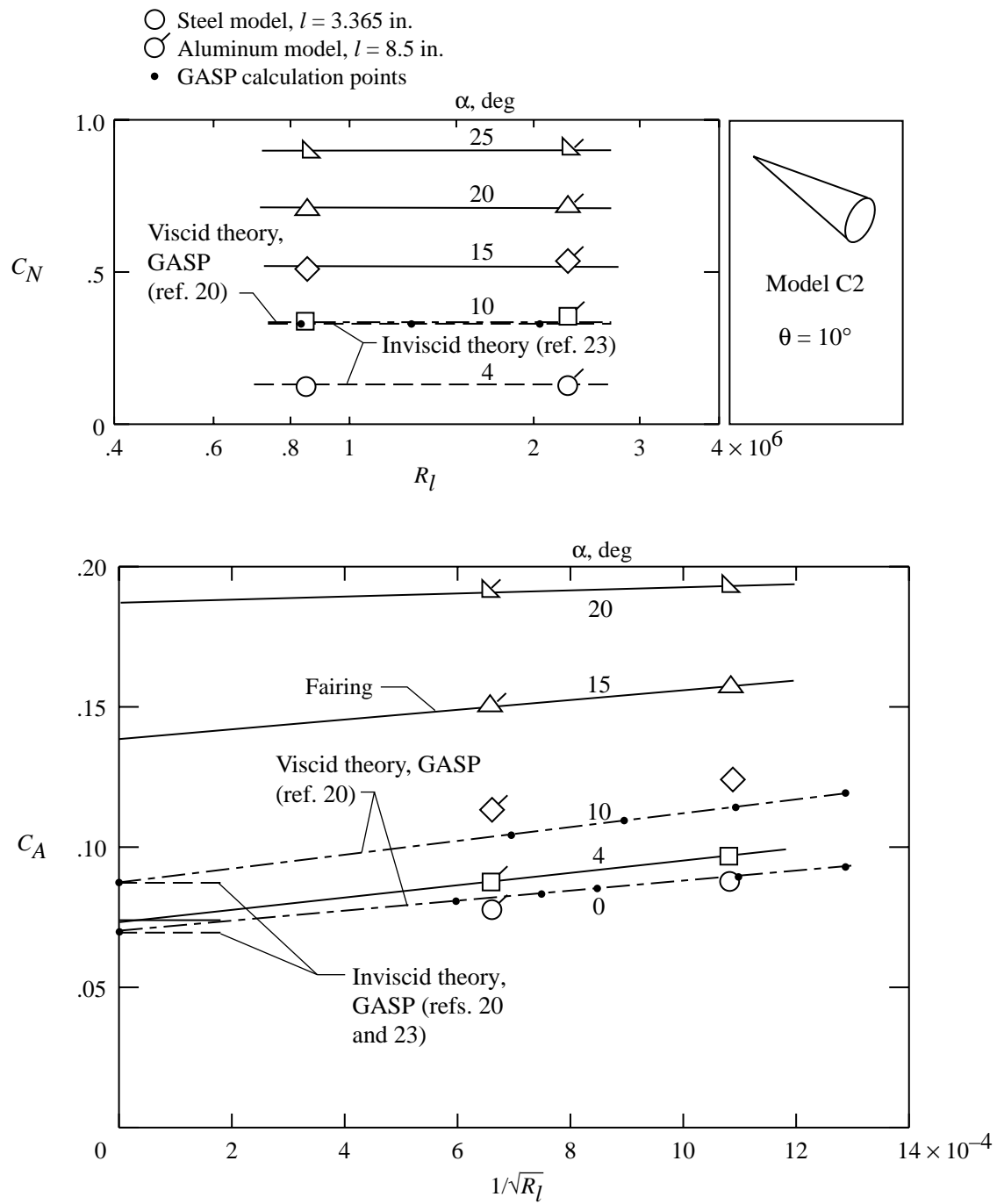
(b) Model C2; θ = 10°.

Figure 3. Continued.
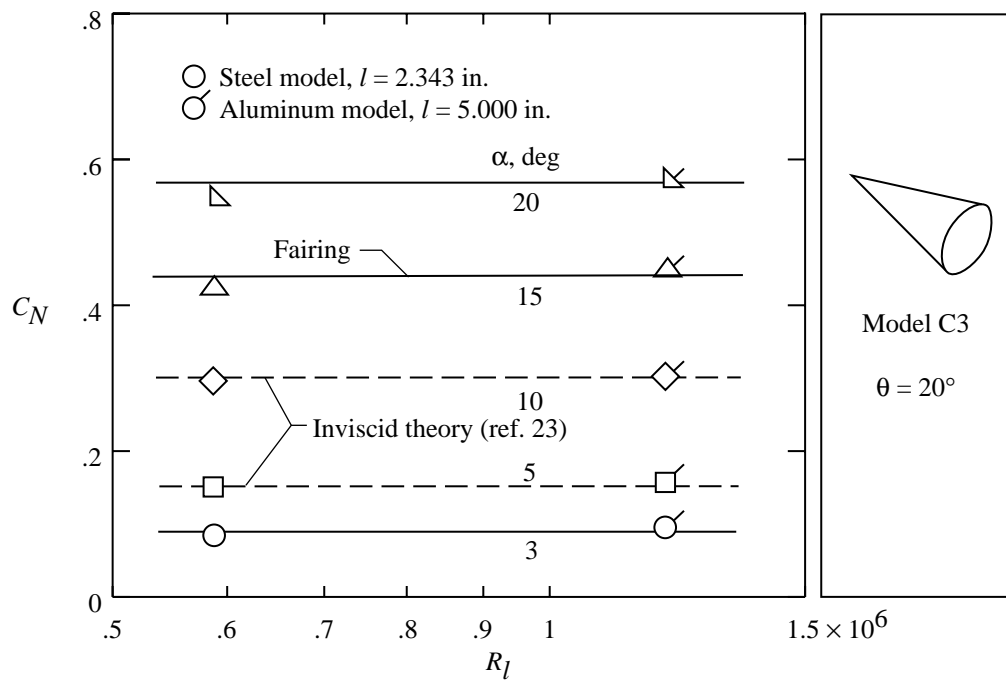
(c) Model C3; θ = 20°.
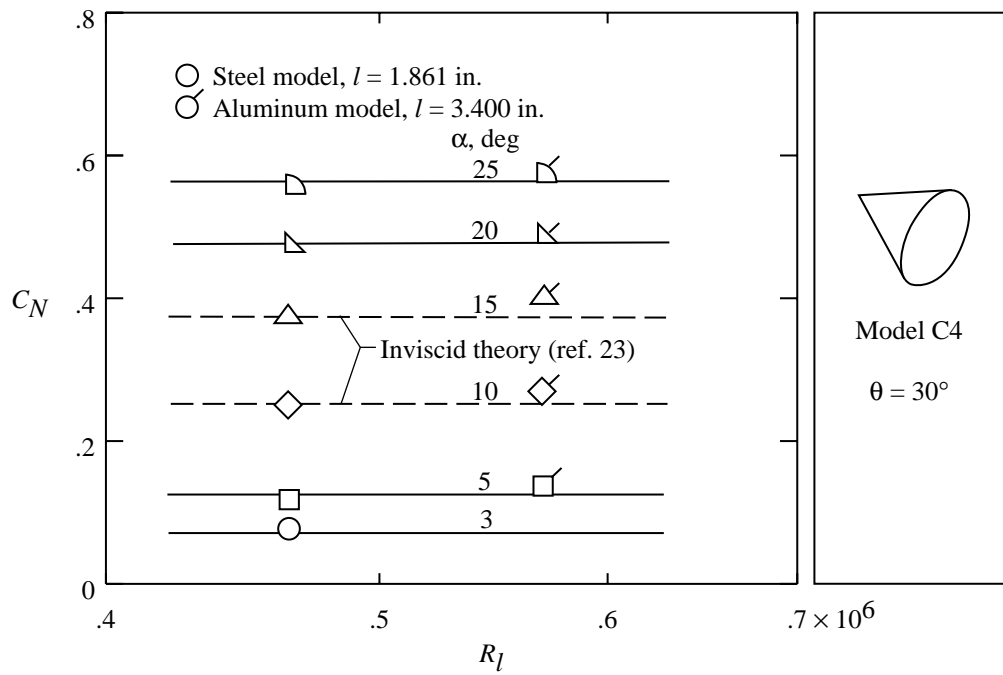
(d) Model C4; θ = 30°.

Figure 3. Concluded.
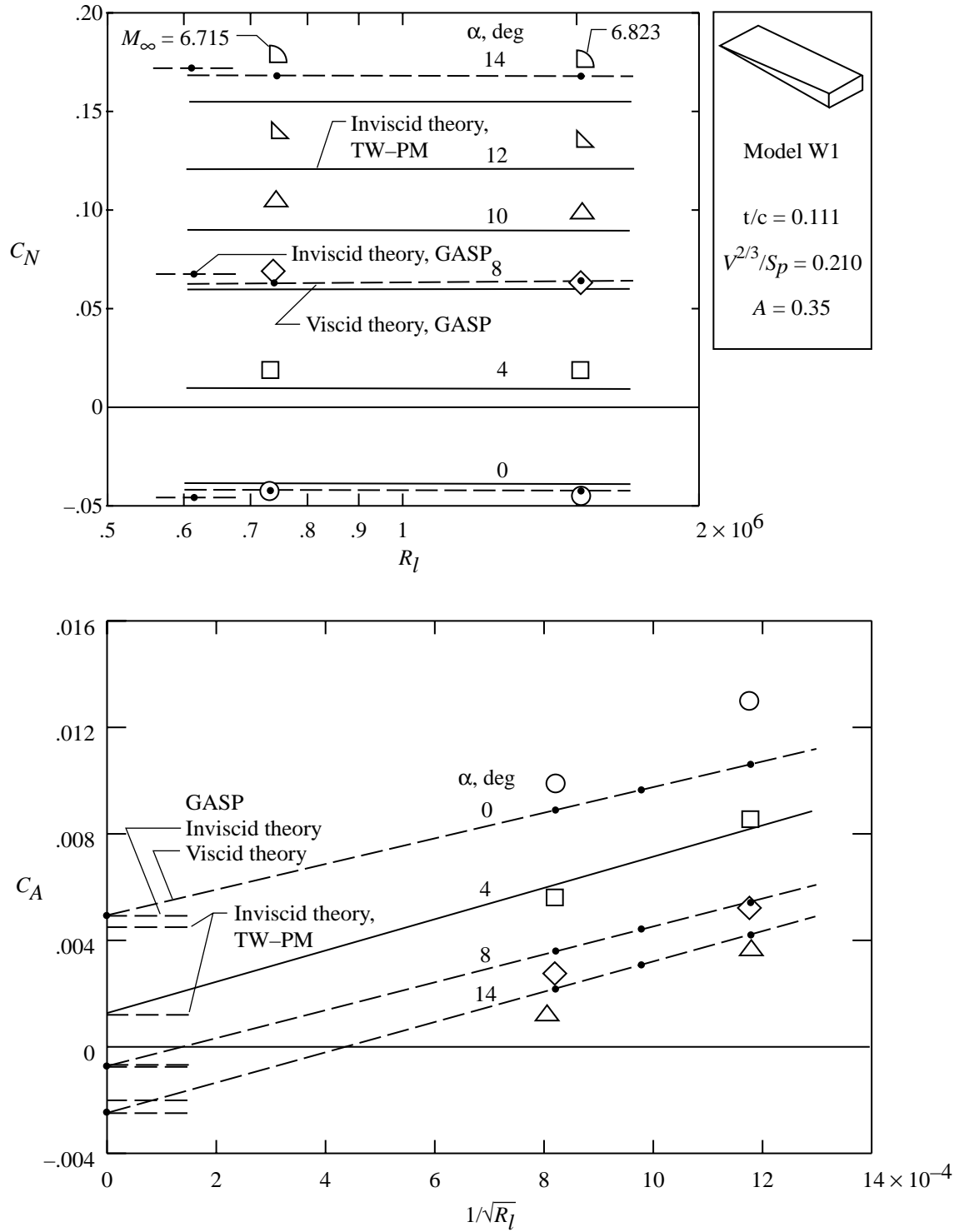
(a) Model W1; $t/c = 0.111$; $V^{2/3}/S_p = 0.210$; $A = 0.35$.

Figure 4. Variation of normal force and axial force coefficients with Reynolds number at $M_\infty \approx 6.86$ for rectangular wings.
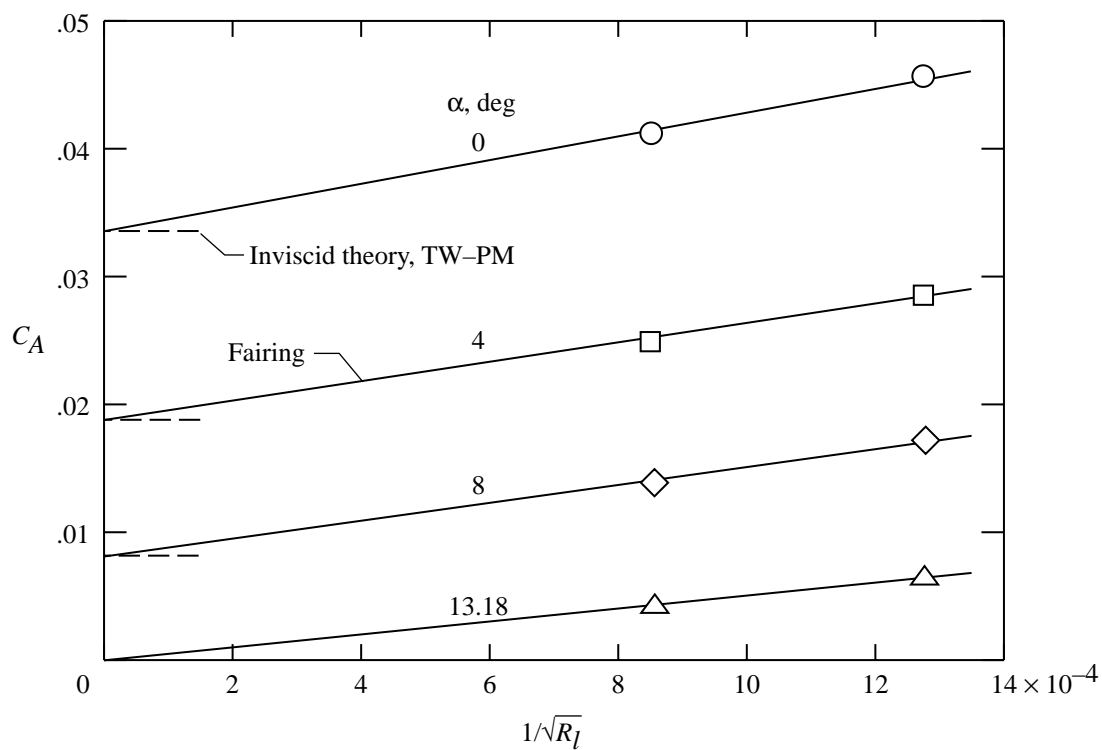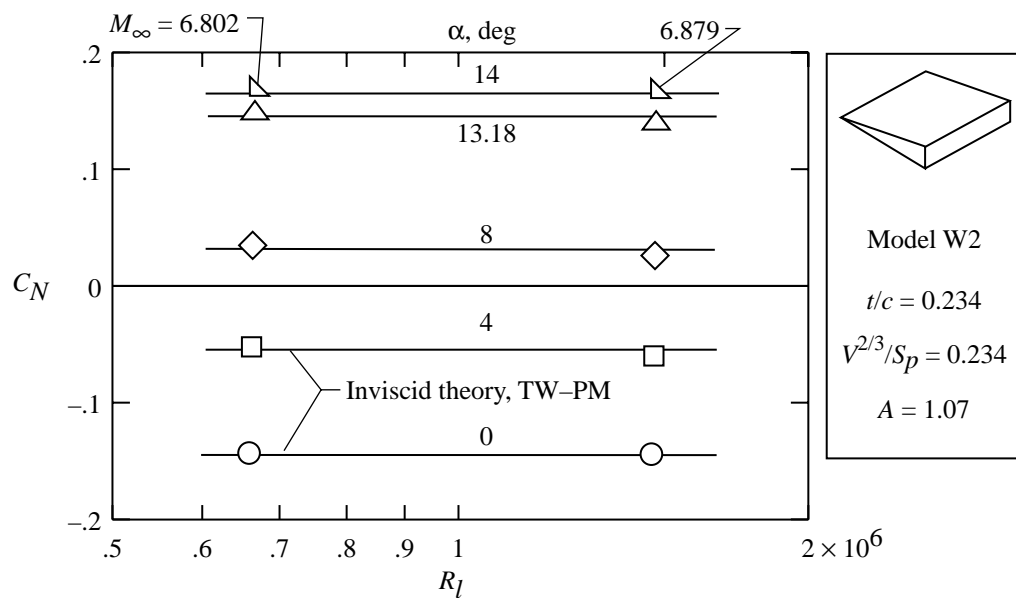
(b) Model W2; $t/c = 0.234$; $V^{2/3}/S_p = 0.234$; $A = 1.07$.

Figure 4. Continued.

$M_\infty = 6.829$ $\quad$ α, deg $\quad$ 6.863

Model W3

$t/c = 0.31$

$V^{2/3}/S_p = 0.200$

$A = 3.00$

Inviscid theory, TW–PM

C_N

R_l

19

16

14

12

10

8

4

0

α, deg

0

Inviscid theory, TW–PM

Fairing

4

8

12

19.22

C_A

$1/\sqrt{R_l}$
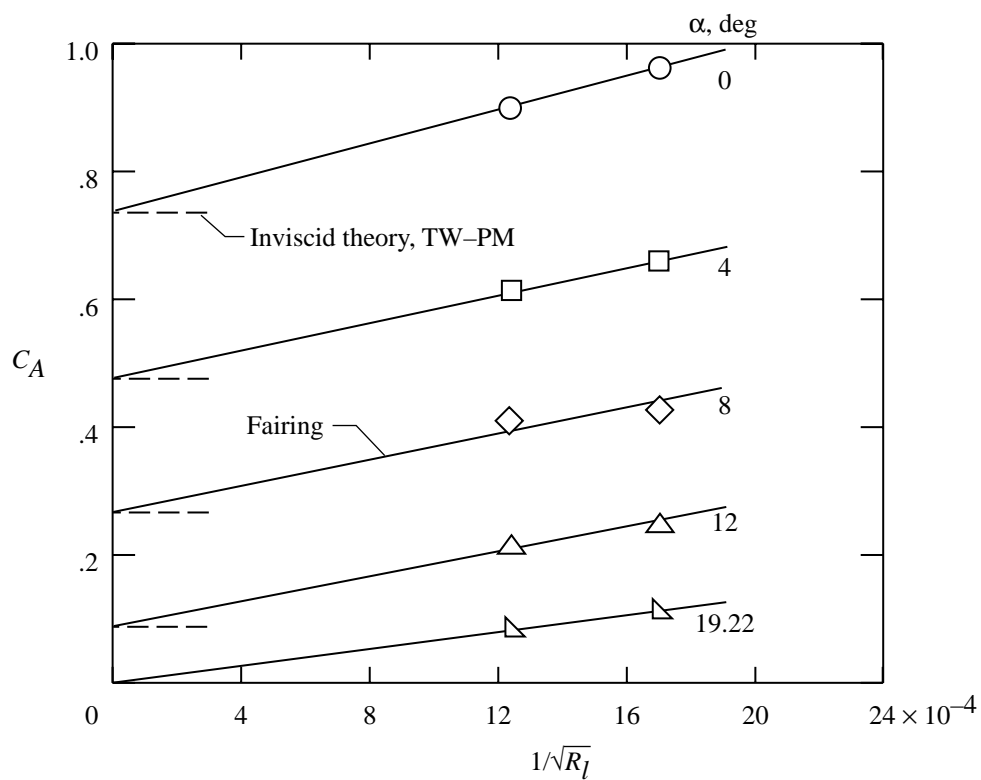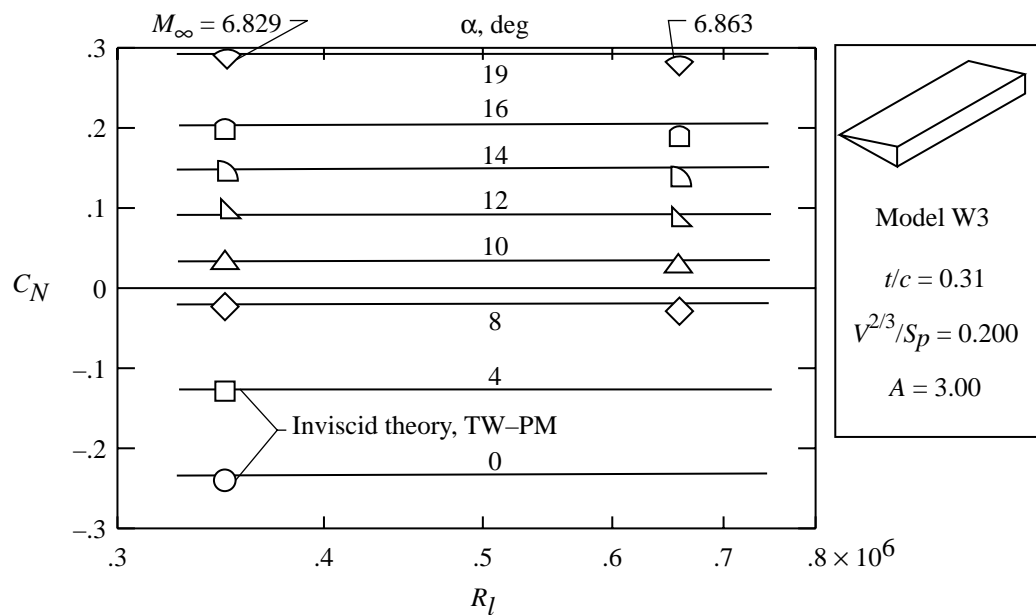
(c) Model W3; $t/c = 0.31$; $V^{2/3}/S_p = 0.200$; $A = 3.00$.

Figure 4. Continued.

35
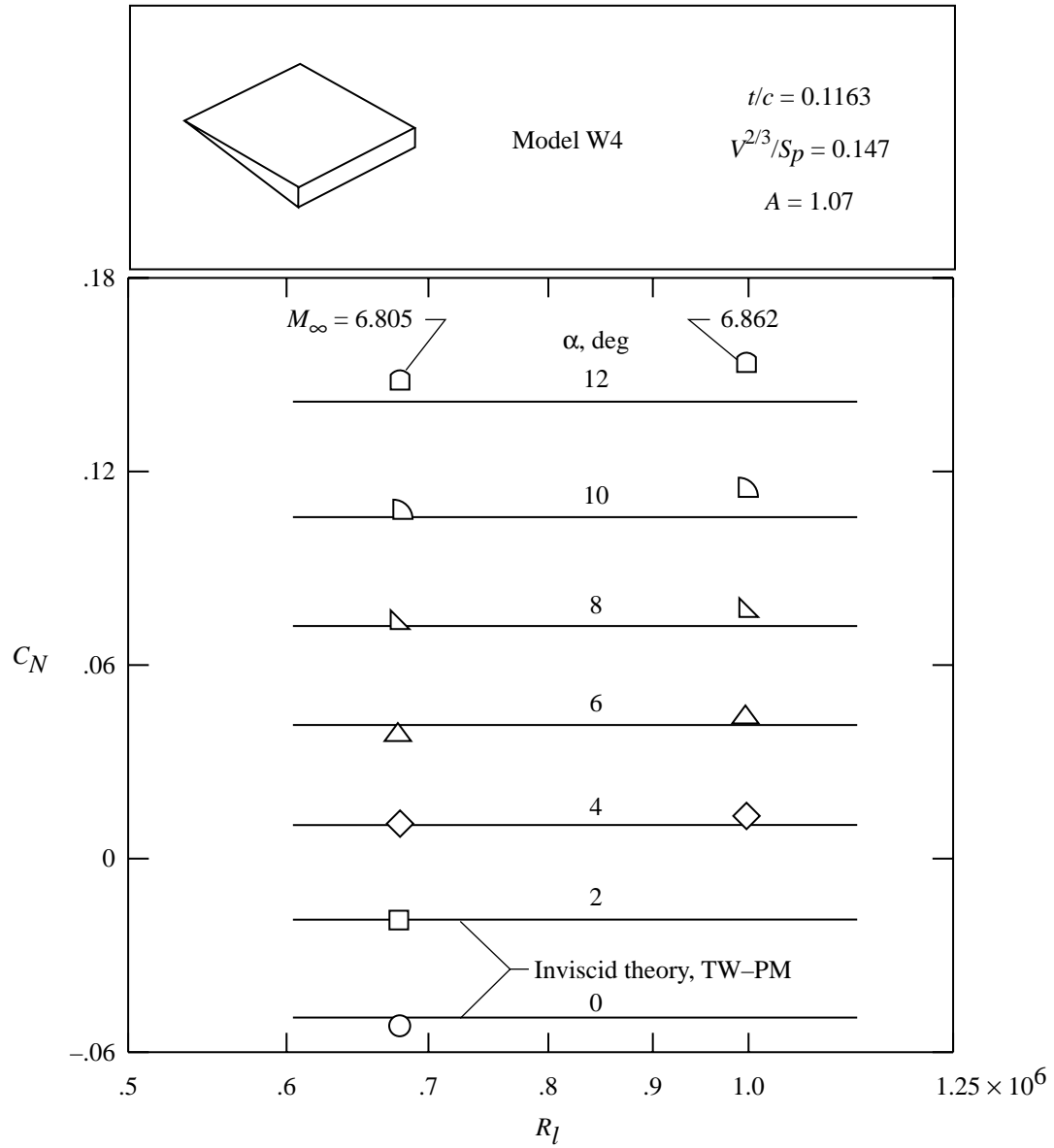
(d) Model W4; $t/c = 0.1163$; $V^{2/3}/S_p = 0.147$; $A = 1.07$.

Figure 4. Concluded.

• GASP calculation points

$M_\infty = 6.705$

6.893

Inviscid theory, TW–PM

α, deg

8

Inviscid and viscid theory, GASP

C_N

4

Inviscid theory, TW–PM

0

R_l

Model D1

$\Lambda = 75°$

$\theta = 5°$

$t/c_r = 0.088$

$V^{2/3}/S_p = 0.147$

$A = 1.07$

C_A

Viscid theory, GASP

α, deg

0

4

8

Inviscid theory, GASP and TW–PM

$1/\sqrt{R_l}$
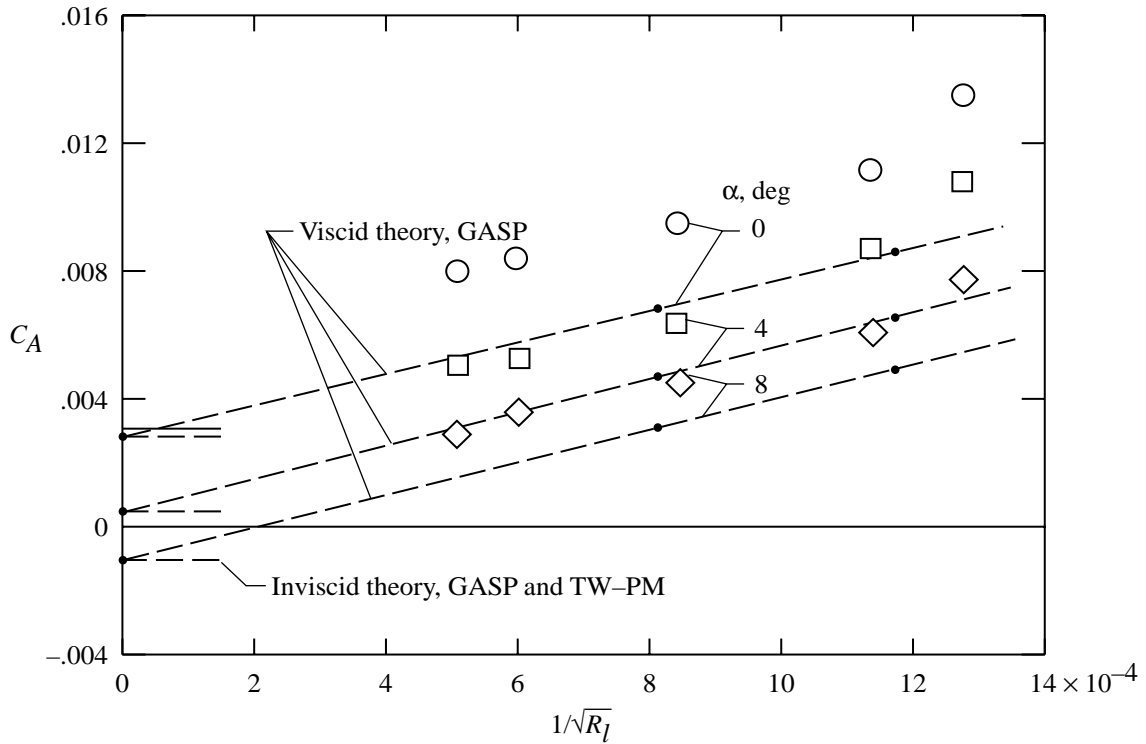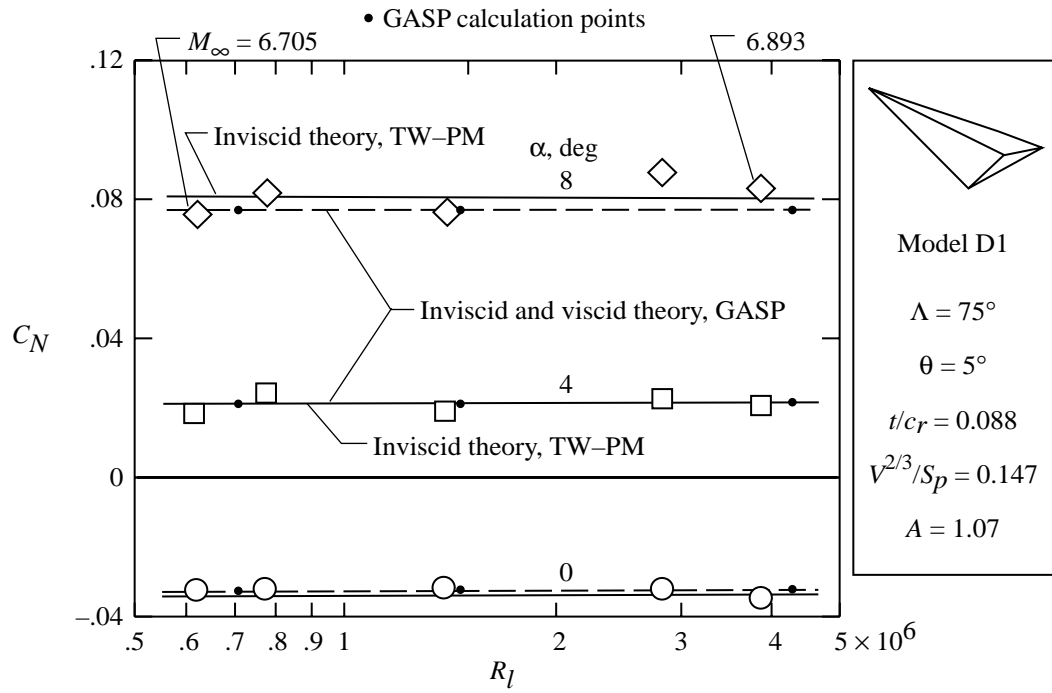
(a) Model D1; $\Lambda = 75°$; $\theta = 5°$; $t/c_r = 0.088$; $V^{2/3}/S_p = 0.147$; $A = 1.07$.

Figure 5. Variation of normal force and axial force coefficients with Reynolds number at $M_\infty \approx 6.86$ for delta wings.
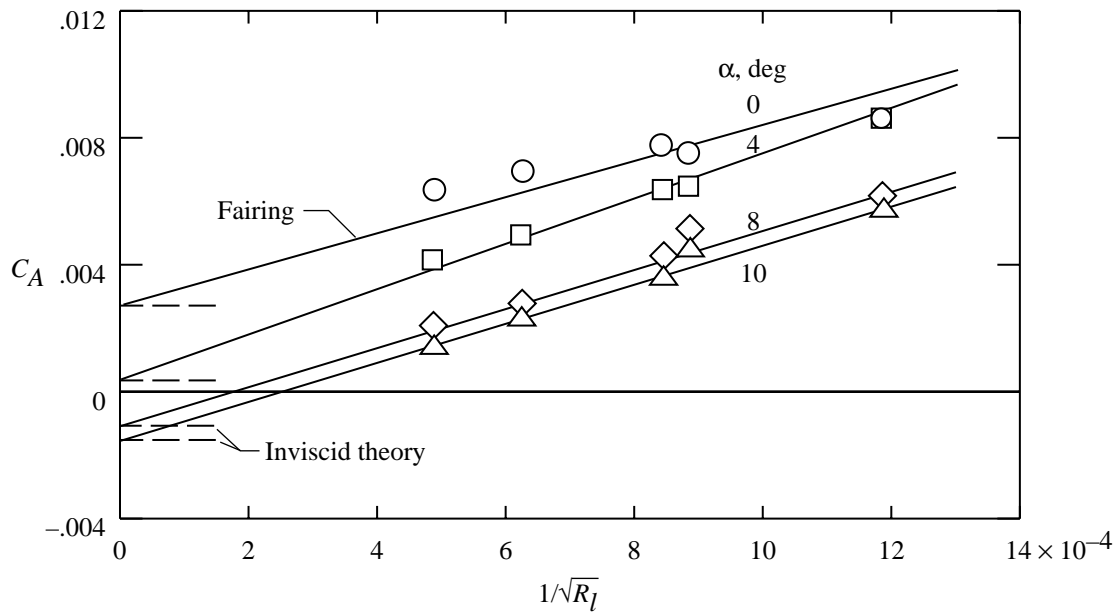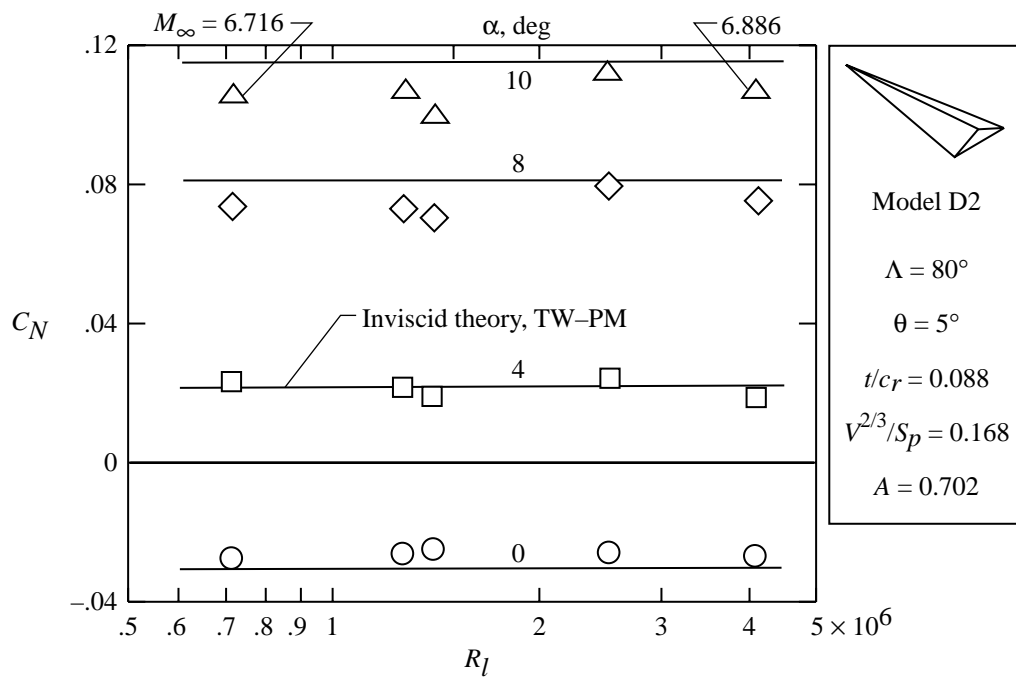
(b) Model D2; $\Lambda = 80°$; $\theta = 5°$; $t/c_r = 0.088$; $V^{2/3}/S_p = 0.168$; $A = 0.702$.

Figure 5. Continued.
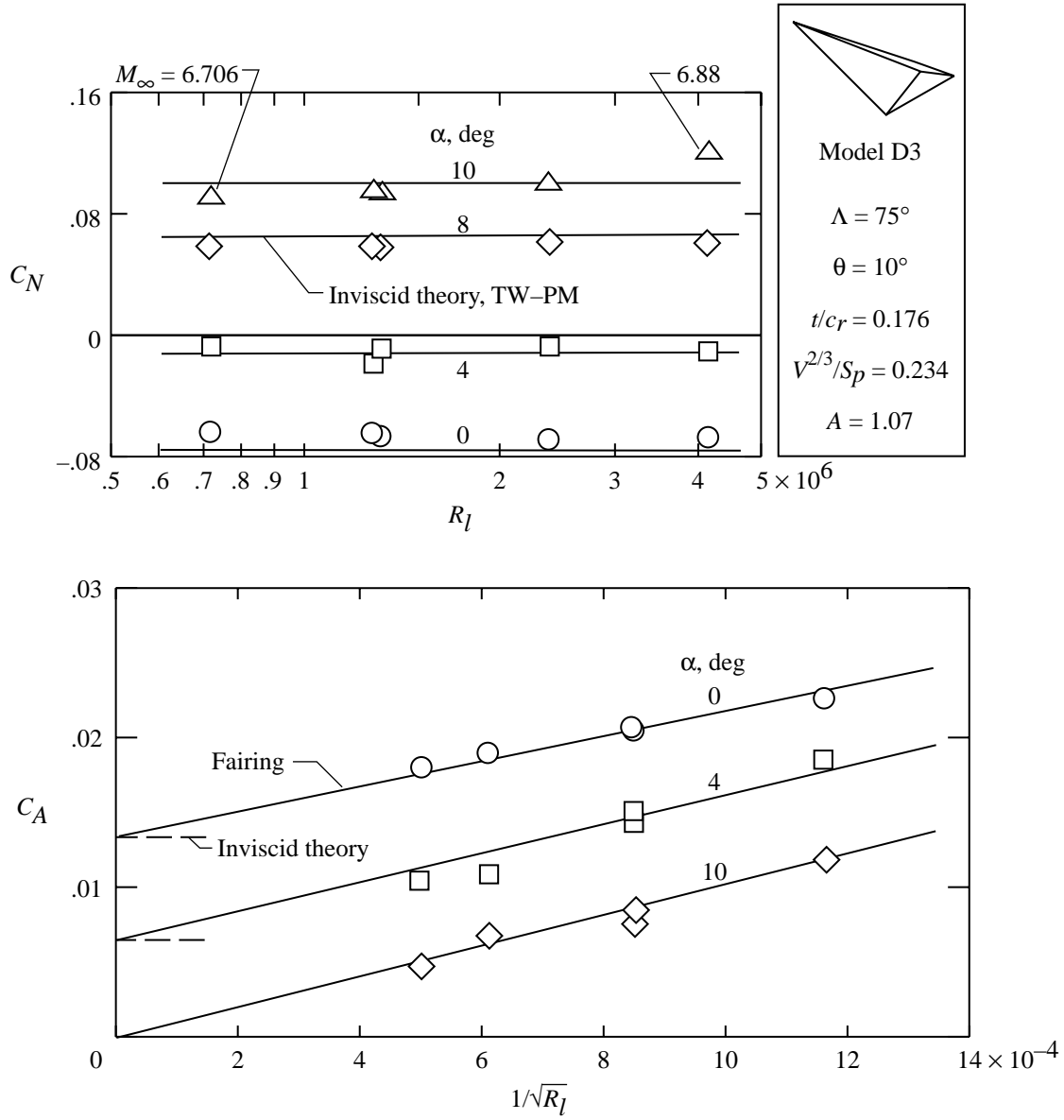
(c) Model D3; $\Lambda = 75°$; $\theta = 10°$; $t/c_r = 0.176$; $V^{2/3}/S_p = 0.234$; $A = 1.07$.

Figure 5. Continued.
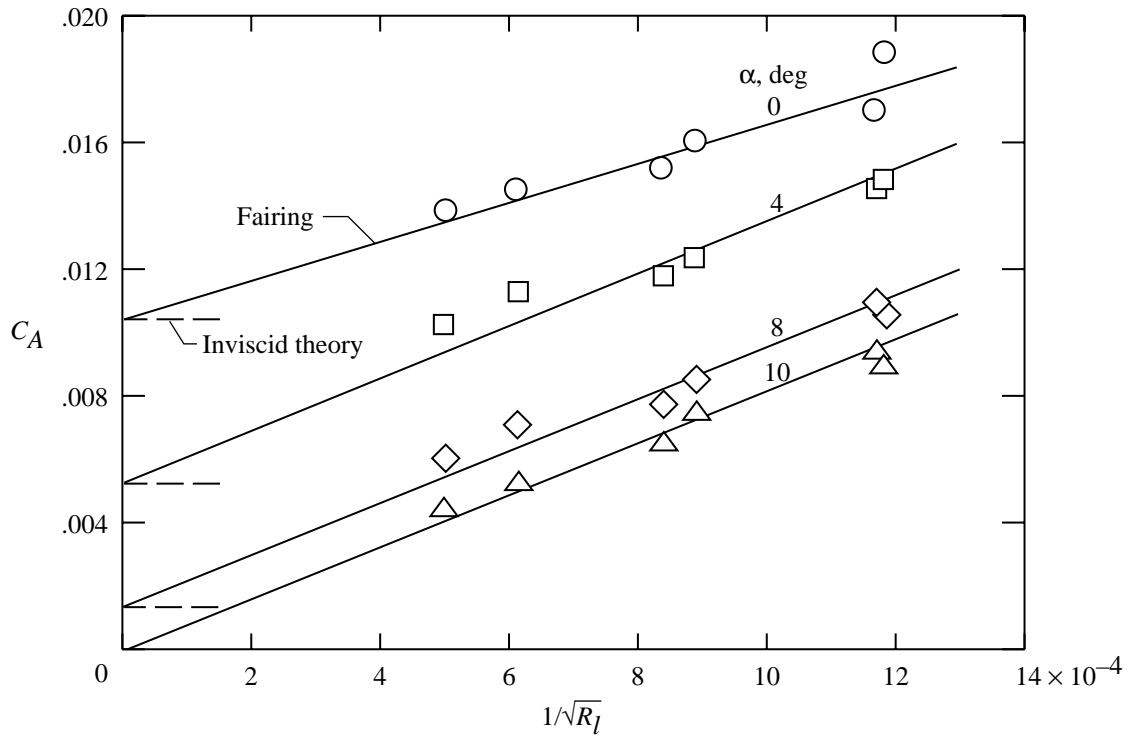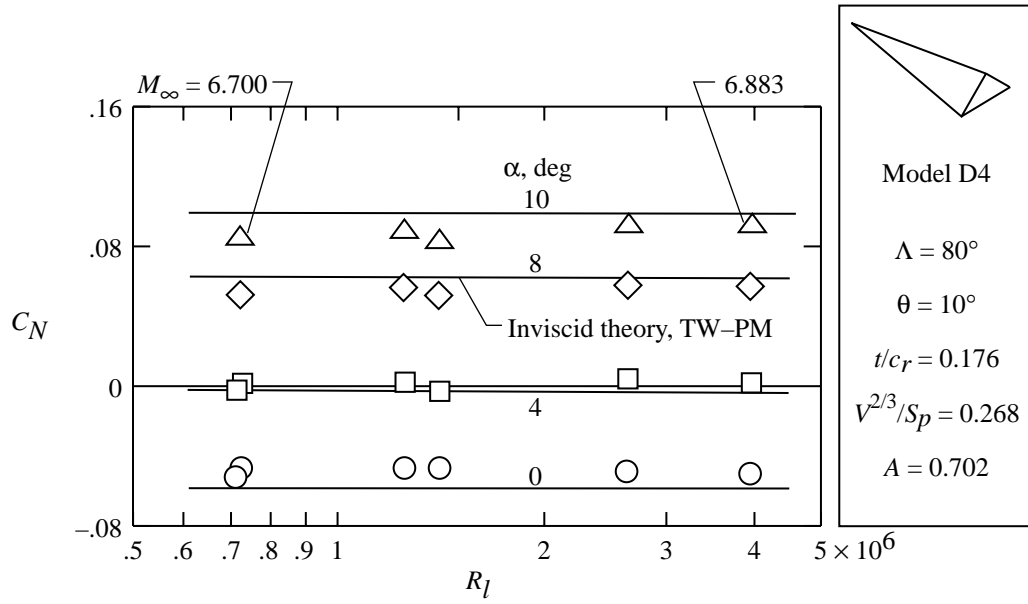
(d) Model D4; $\Lambda = 80°$; $\theta = 10°$; $t/c_r = 0.176$; $V^{2/3}/S_p = 0.268$; $A = 0.702$.

Figure 5. Continued.

Model D5

$\Lambda = 85°$

$\theta = 5°$

$A = 0.35$

$t/c_r = 0.088$

$V^{2/3}/S_p = 0.210$

.20

TW–PM

Inviscid theory

α, deg

14

$M_\infty = 6.686$ TC–PM

6.883

.15

12

.10

10

8

.05

6

4

2

0

Inviscid theory

0

−2

−.05

.5 .6 .7 .8 .9 1 2 3 4 5 × 10^6

C_N

R_l
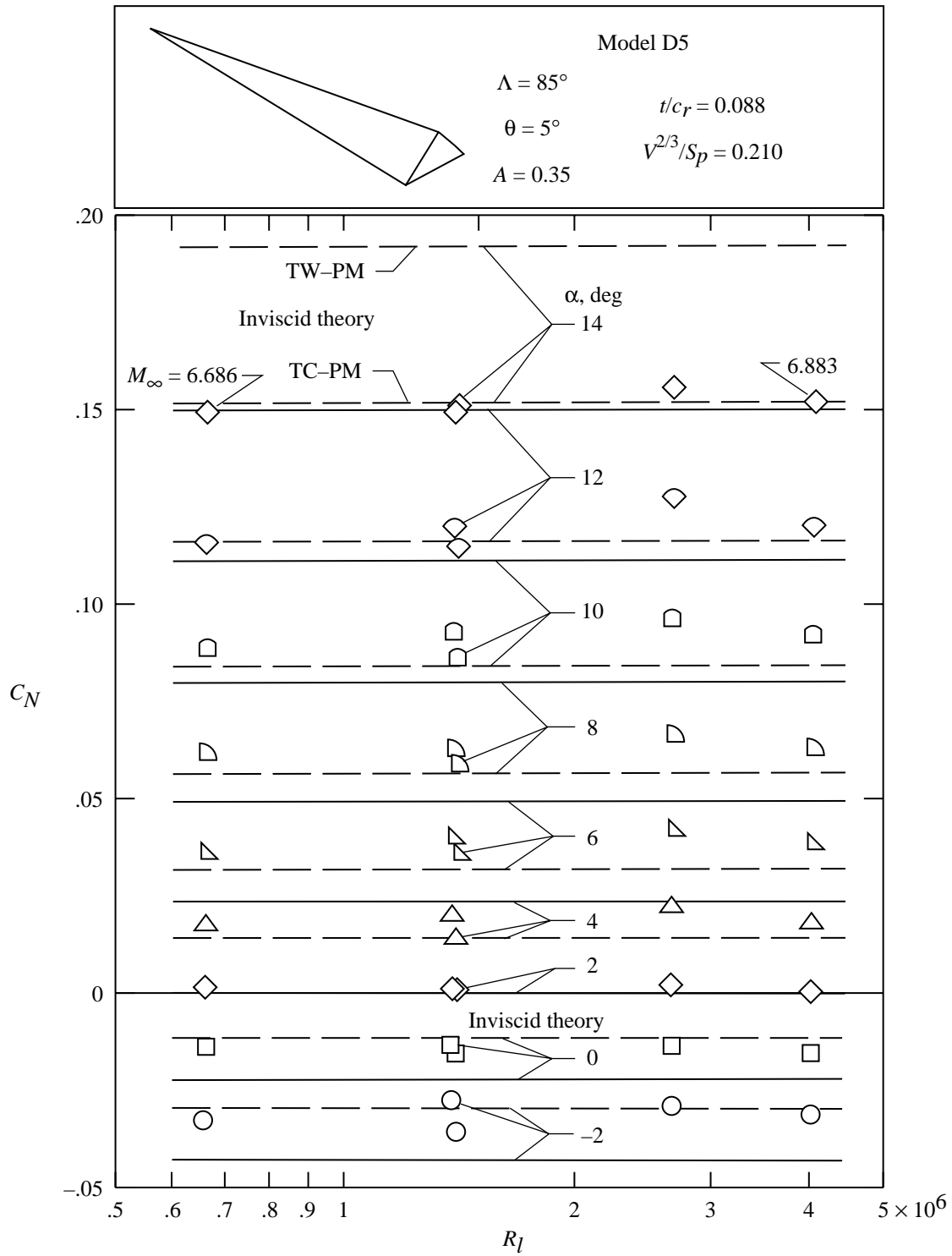
(e) Model D5; $\Lambda = 85°$; $\theta = 5°$; $t/c_r = 0.088$; $V^{2/3}/S_p = 0.210$; $A = 0.35$.

Figure 5. Concluded.

41

Figure 6. Variation of normal force and axial force coefficients with Reynolds number at $M_\infty \approx 6.86$ for caret wing. $\Lambda = 75°$; $\theta = 6.63°$; $t/c_r = 0.1163$; $V^{2/3}/S_p = 0.178$; $A = 1.07$.
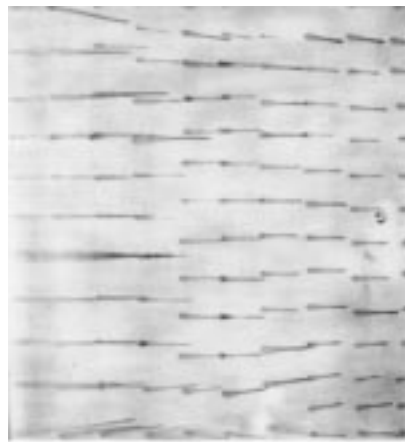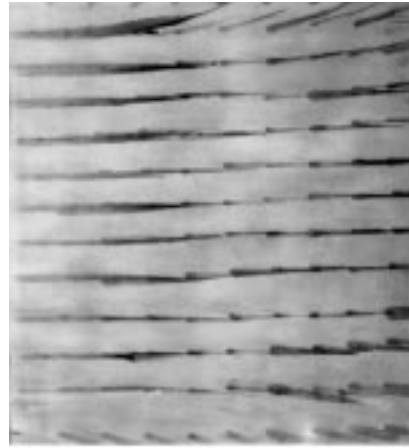
Top surface   Bottom surface

(a) Model W4; $\alpha = 9°$; $M_\infty = 6.86$; $R_l = 0.99 \times 10^6$.
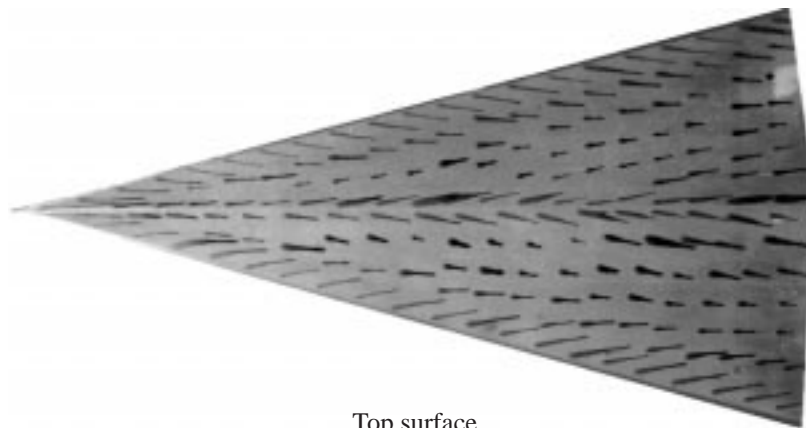
Top surface
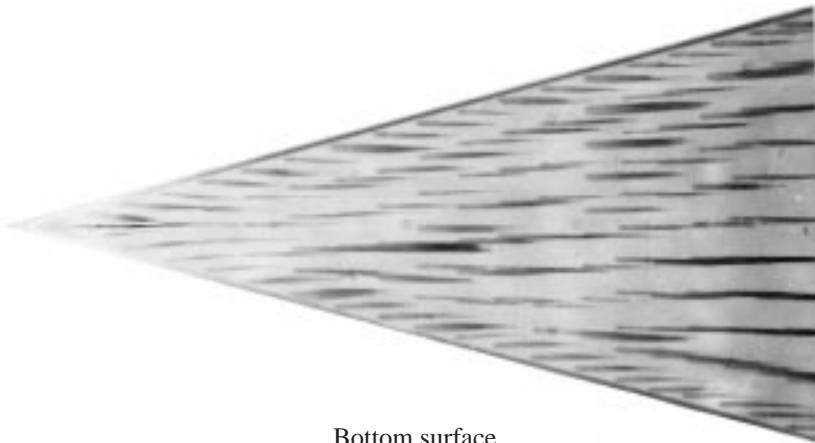
Bottom surface

(b) Model D1; $\alpha = 7°$; $M_\infty = 6.89$; $R_l = 3.88 \times 10^6$.

Figure 7. Oil flow on models.

Top surface viewed from side

Bottom surface

(c) Model D5; $\alpha = 8.5°$; $M_\infty = 6.69$; $R_l = 0.663 \times 10^6$.
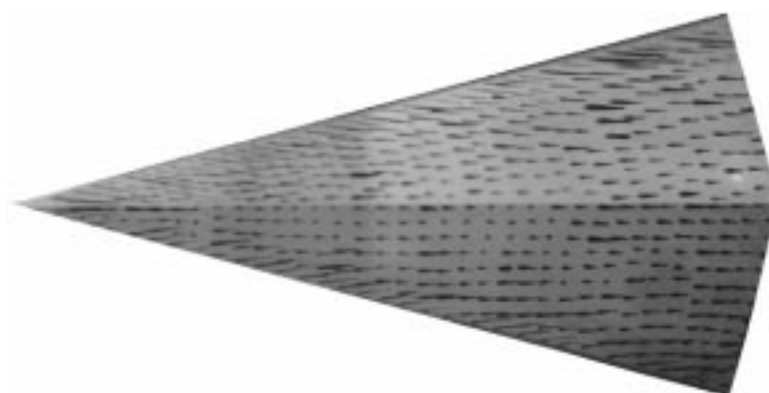
Top surface
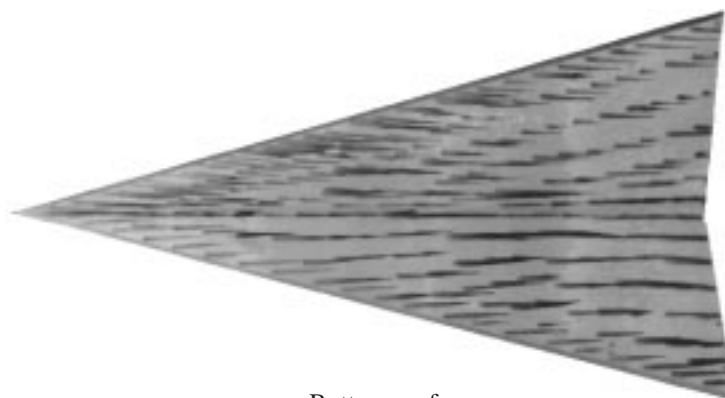
Bottom surface

(d) Caret wing; $\alpha = 7.5°$; $M_\infty = 6.83$; $R_l = 1.51 \times 10^6$.

Figure 7. Concluded.
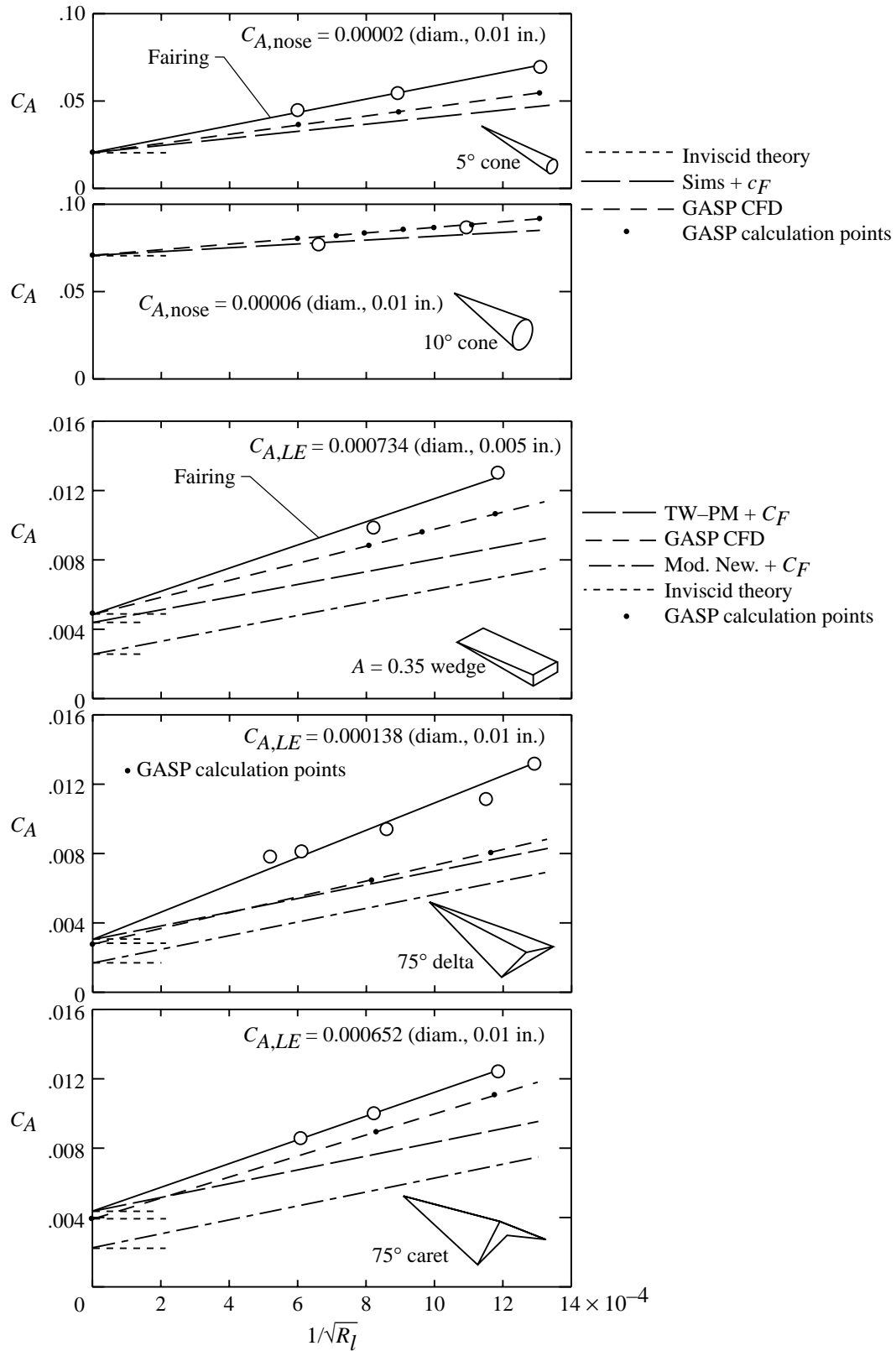
Figure 8. Theoretical and experimental axial force coefficients at $M_\infty = 6.86$ and $\alpha = 0°$ for simple configurations under laminar flow conditions.
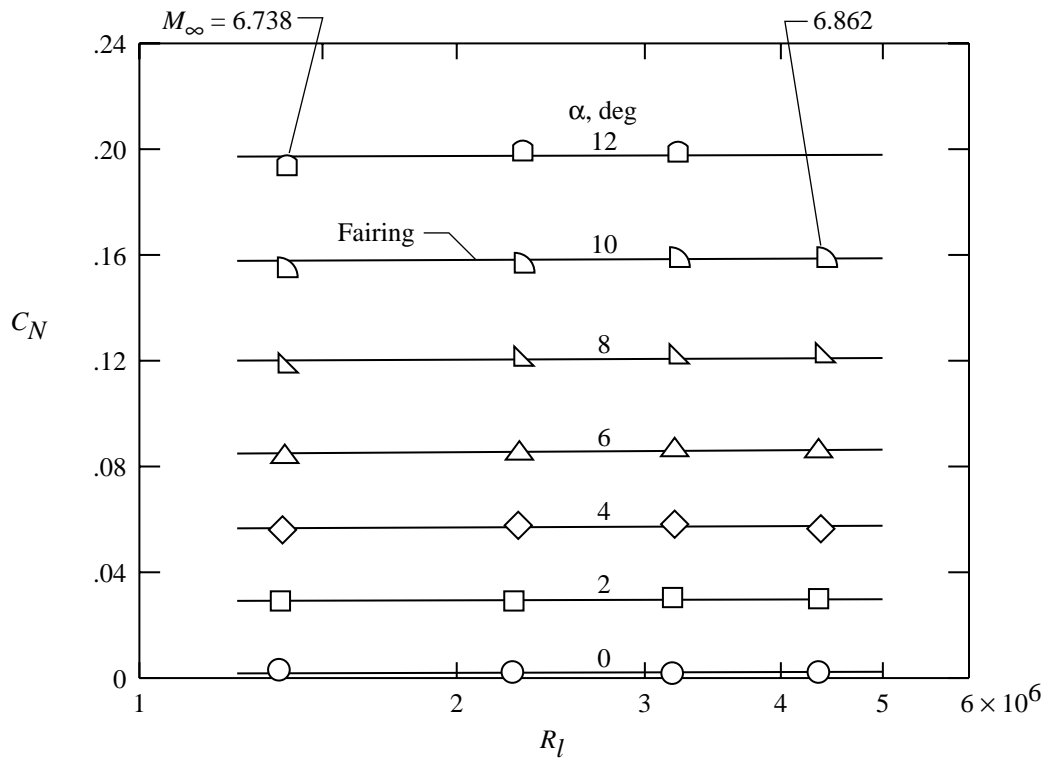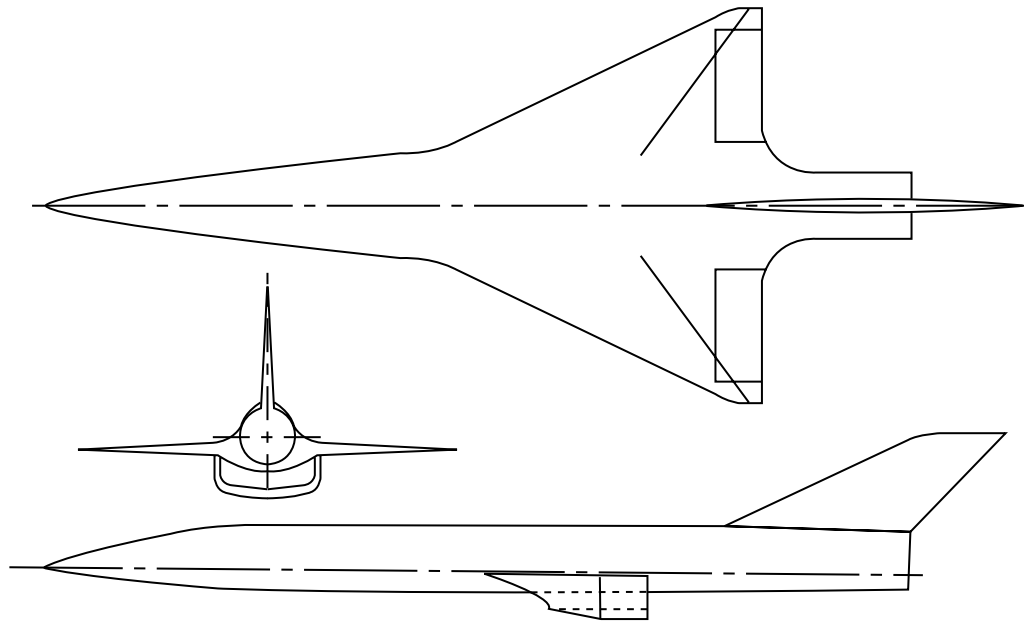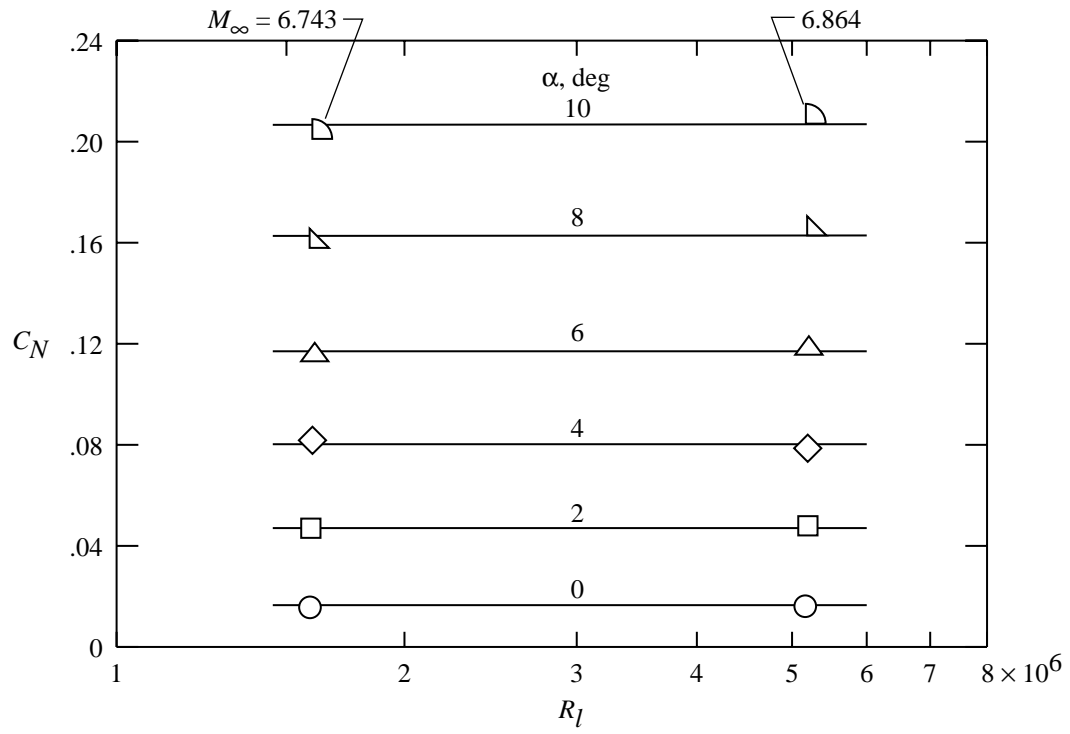
(a) BWEVI with $\delta_E = 0°$.

Figure 9. Variation of normal force coefficients with Reynolds number at $M_\infty \approx 6.86$ for blended body–wing hypersonic cruise configuration.
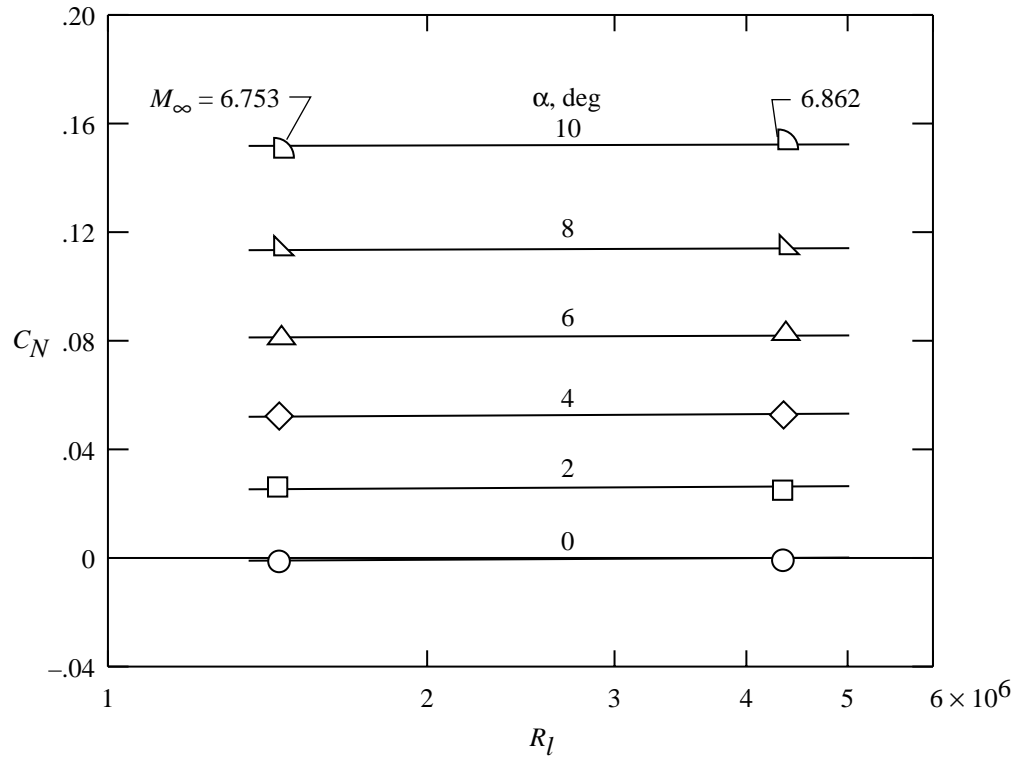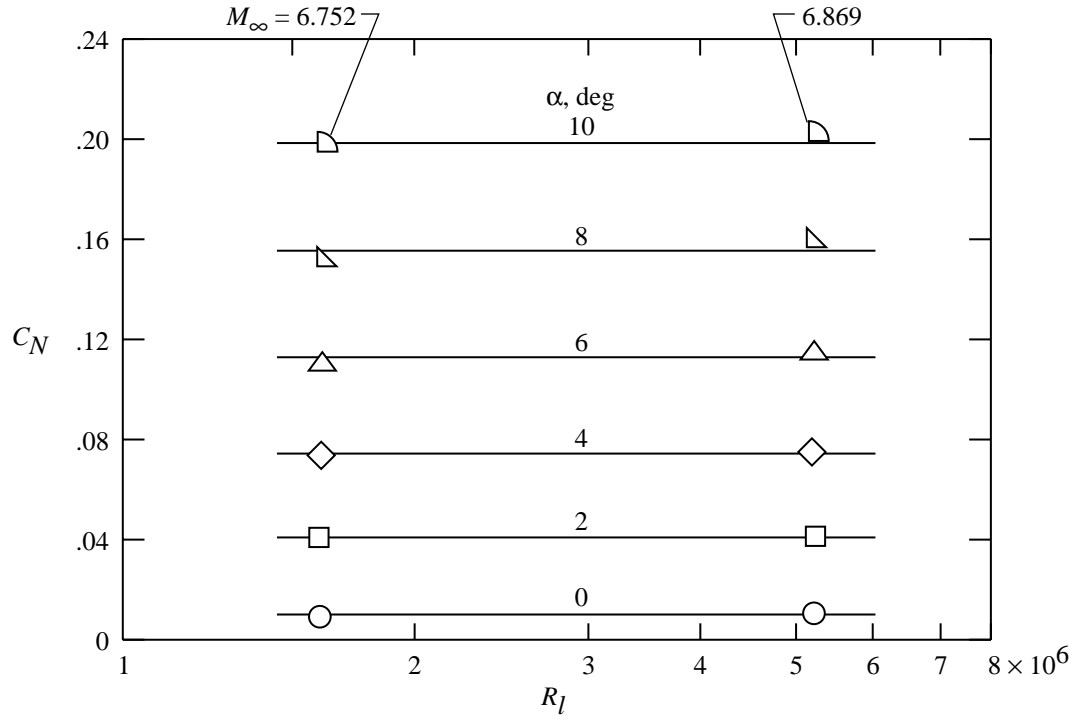
(b) BWEVI with $\delta_E = -5°$.
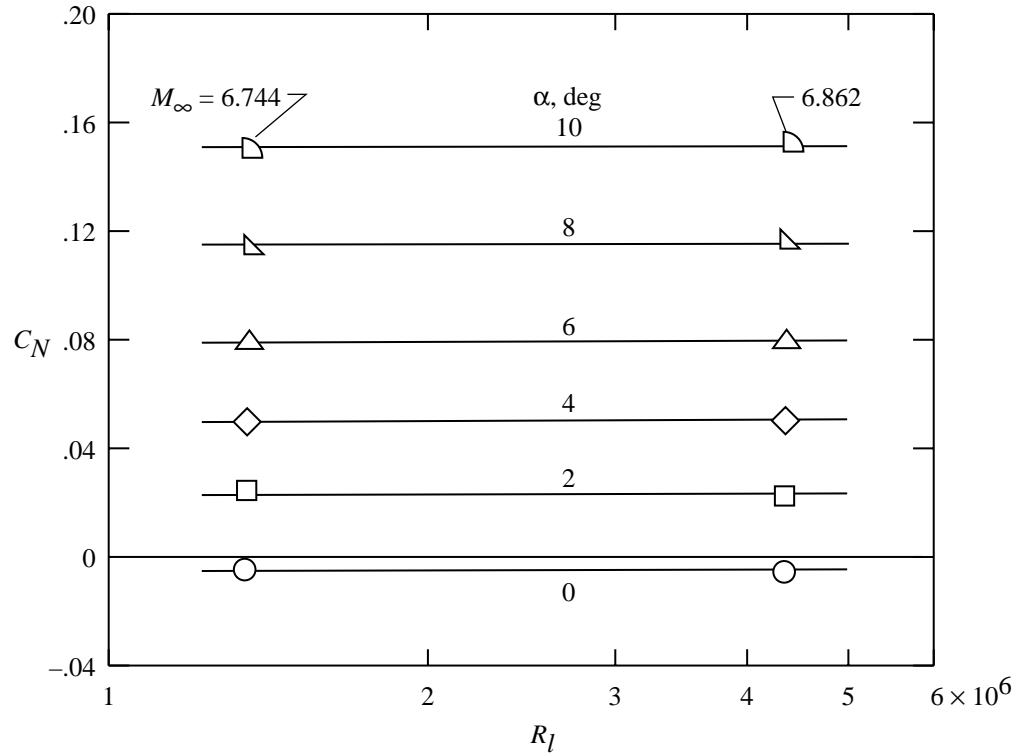
(c) BWEVI with $\delta_E = -10°$.

Figure 9. Continued.
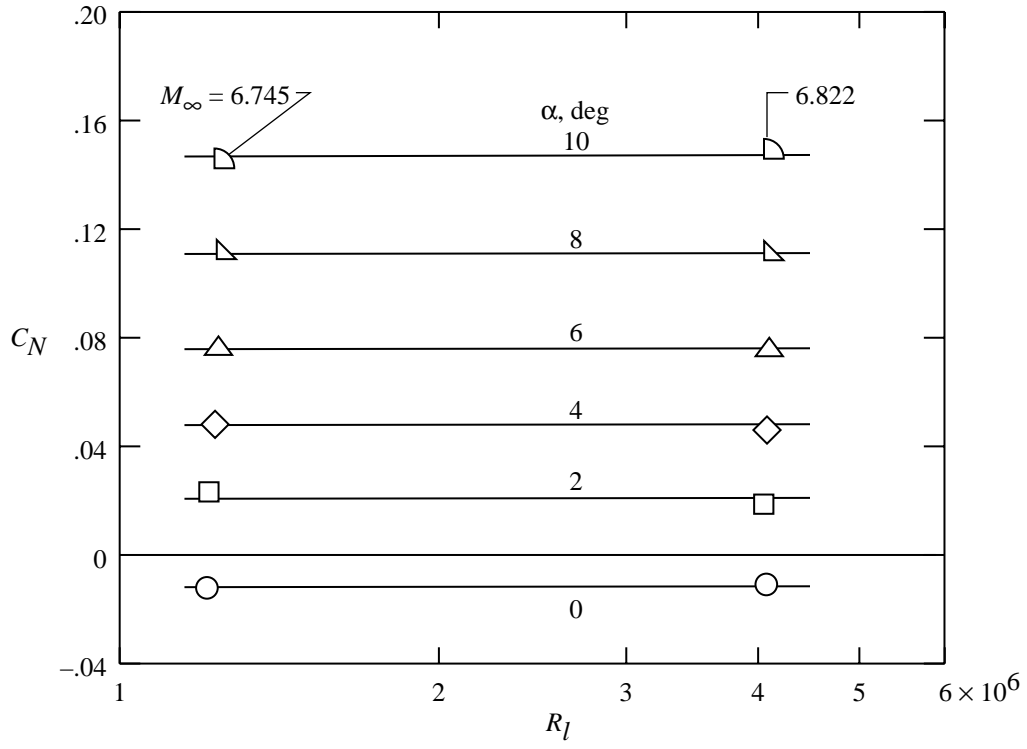
(d) BWEVI with $\delta_E = -15°$.
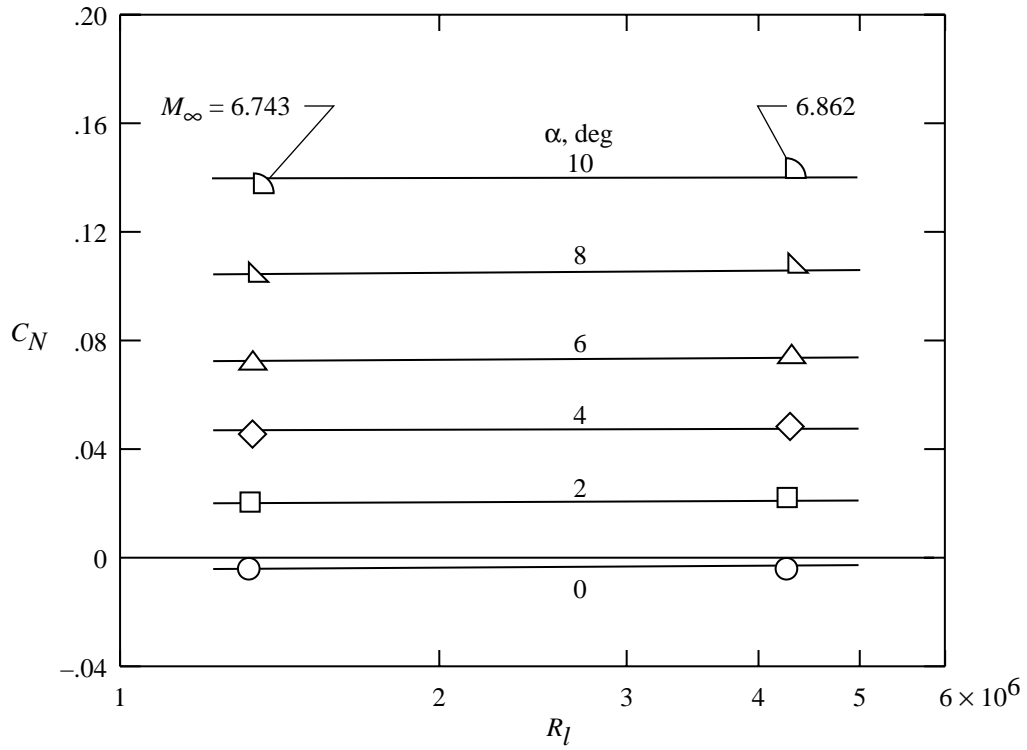
(e) BWEV with $\delta_E = 0°$.

Figure 9. Concluded.
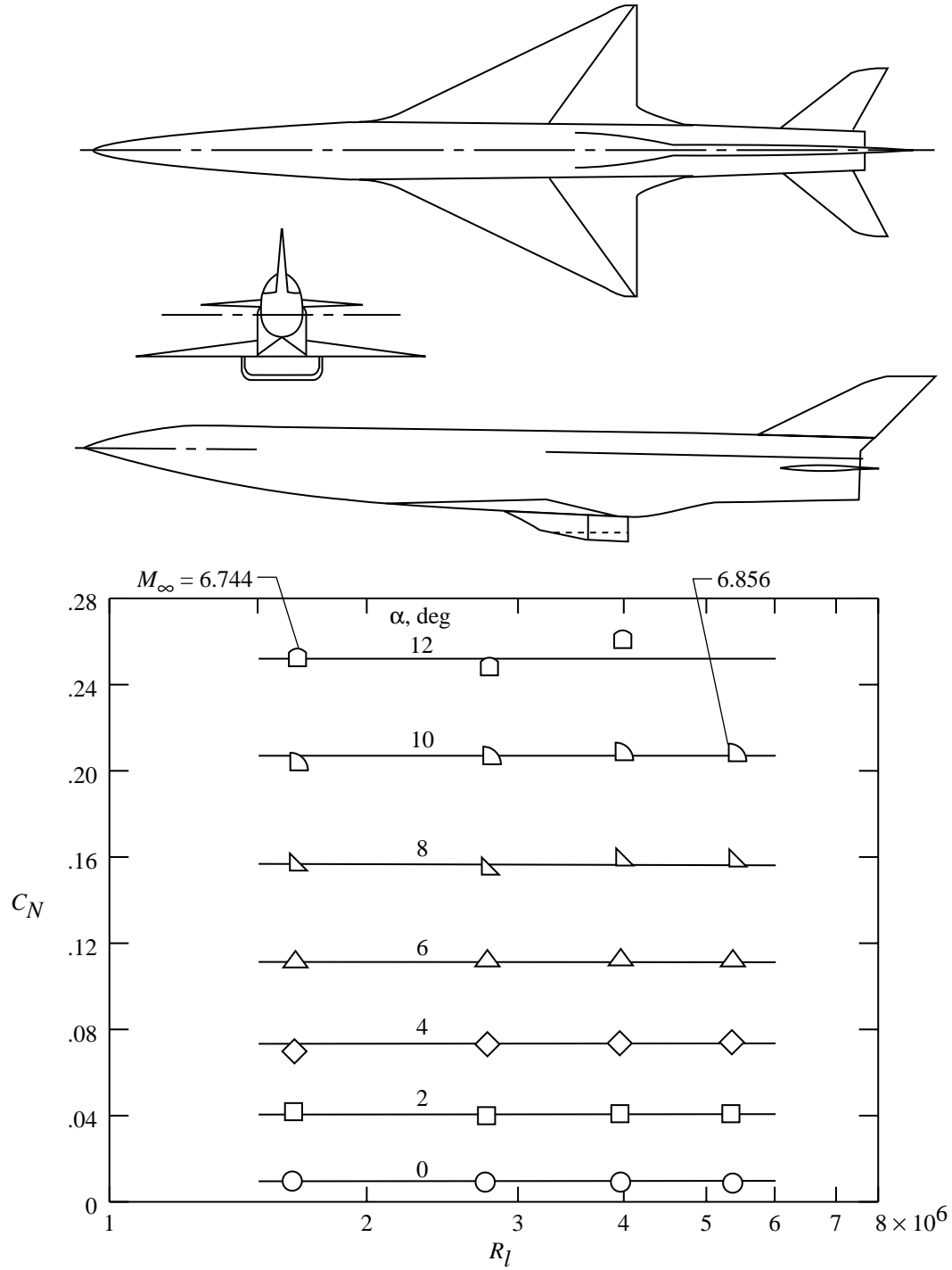
(a) BWHVI with $\delta_H = 0°$.

Figure 10. Variation of normal force coefficients with Reynolds number at $M_\infty \approx 6.86$ for distinct body–wing–horizontal tail hypersonic cruise configuration.
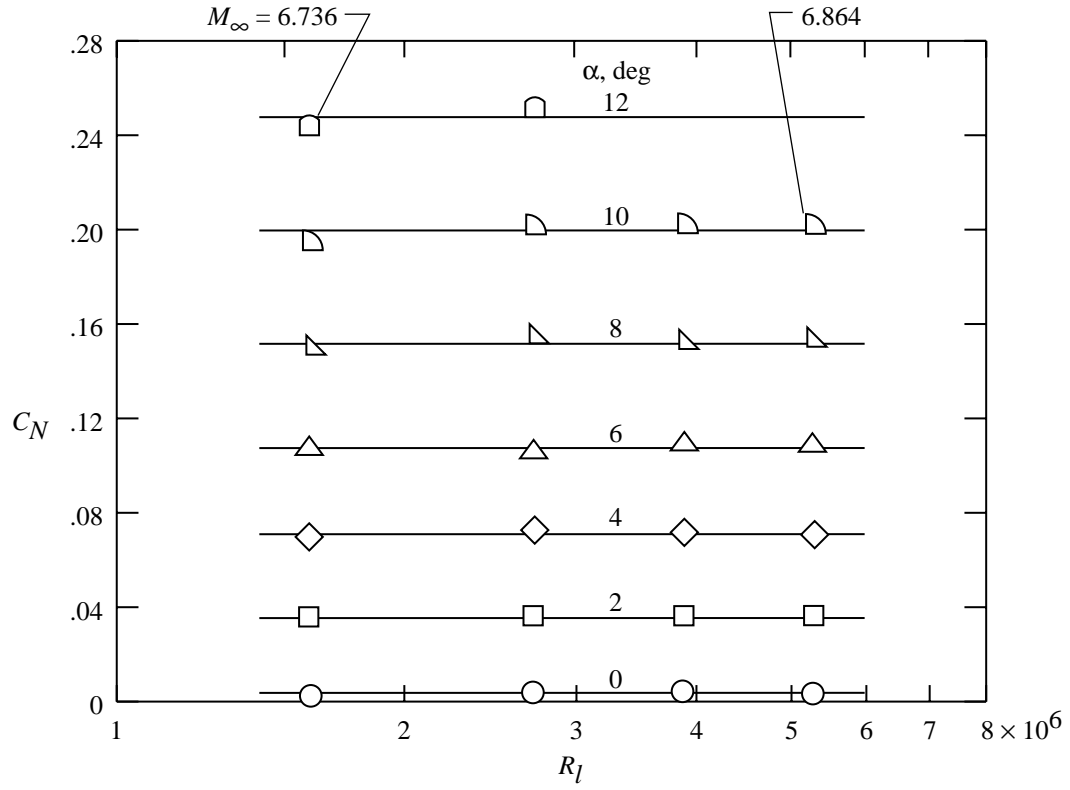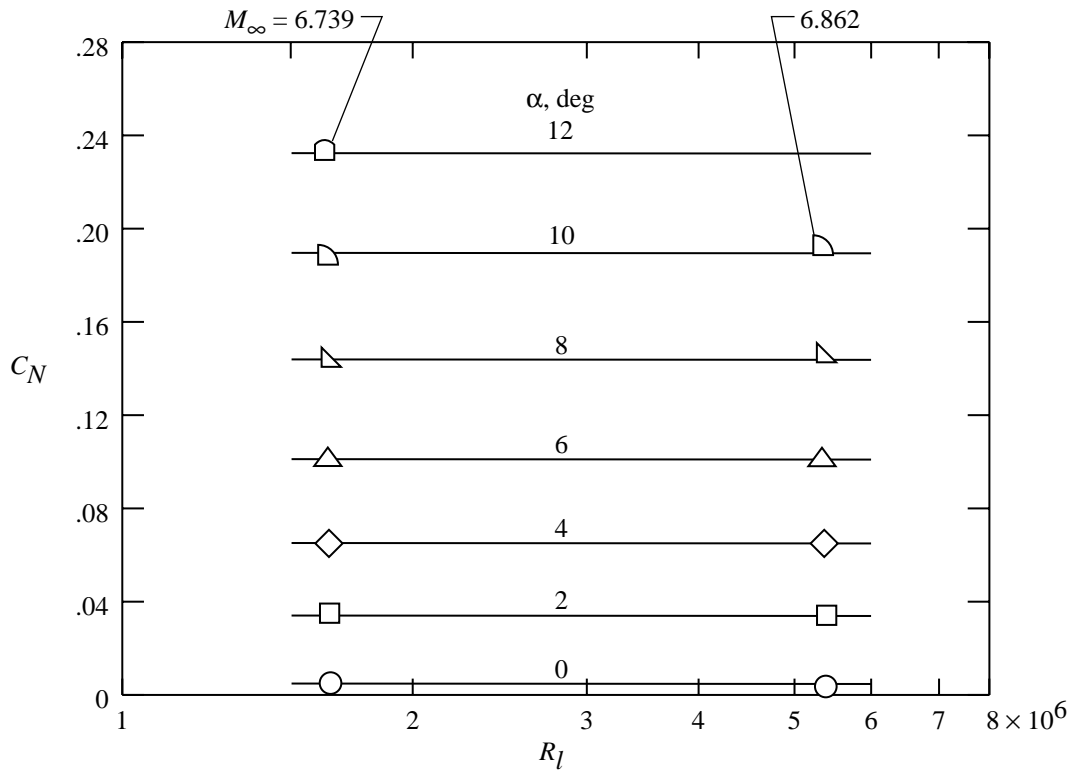
(b) BWHVI with $\delta_H = -5°$.
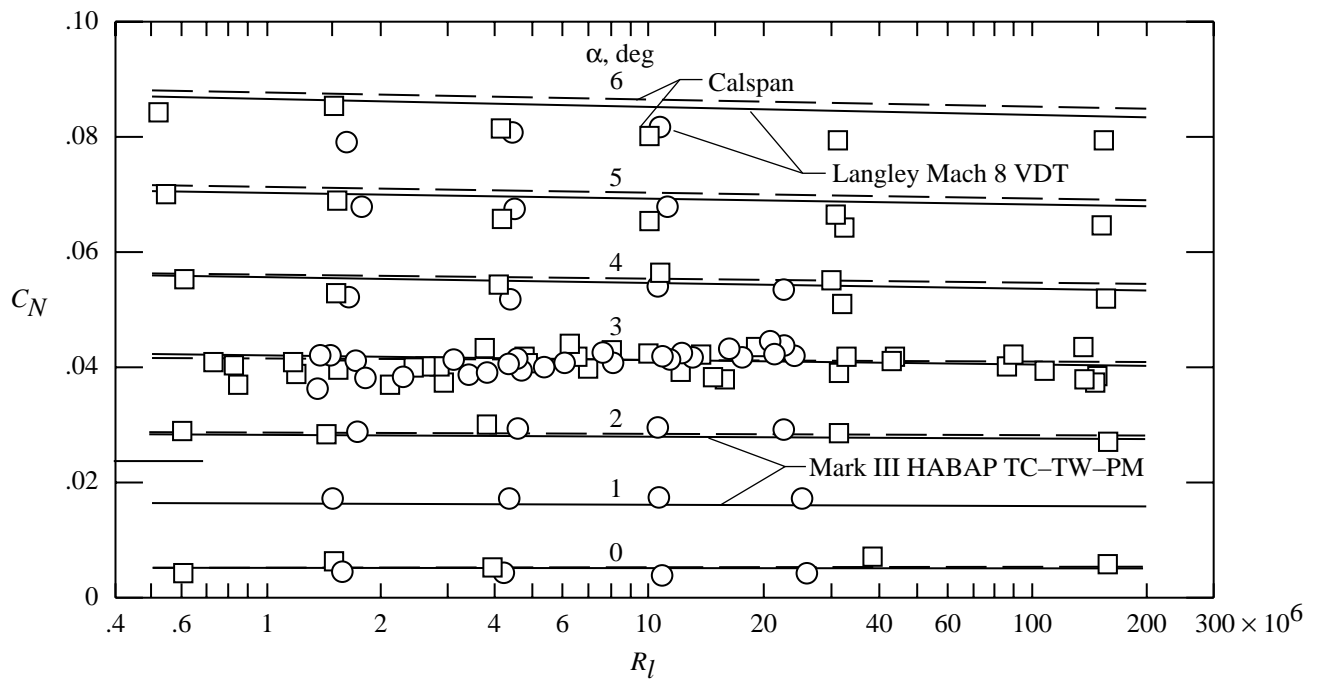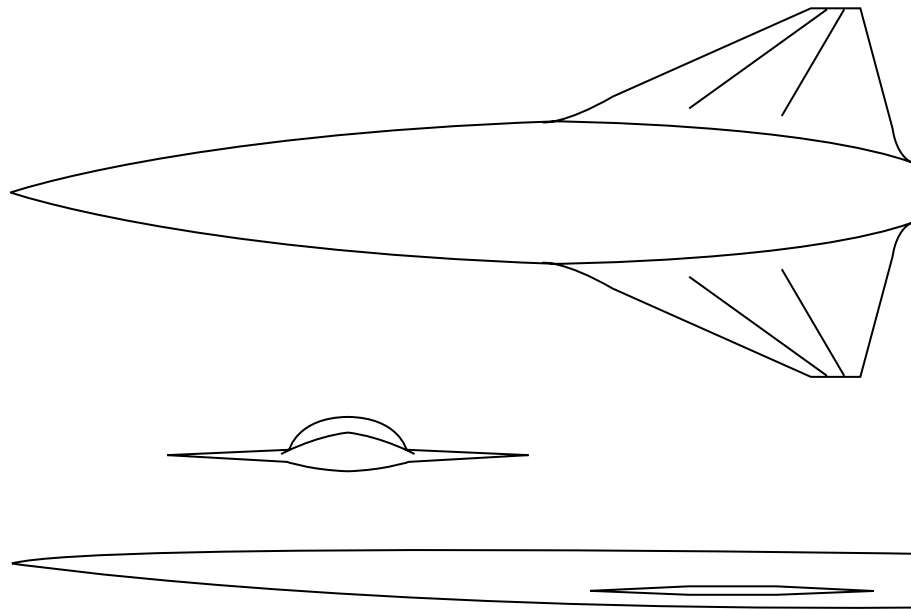

(c) BWHVI with $\delta_H = +5°$.

Figure 10. Continued.

(d) BWHVI with $\delta_H = 0°$; $\beta = -4°$.

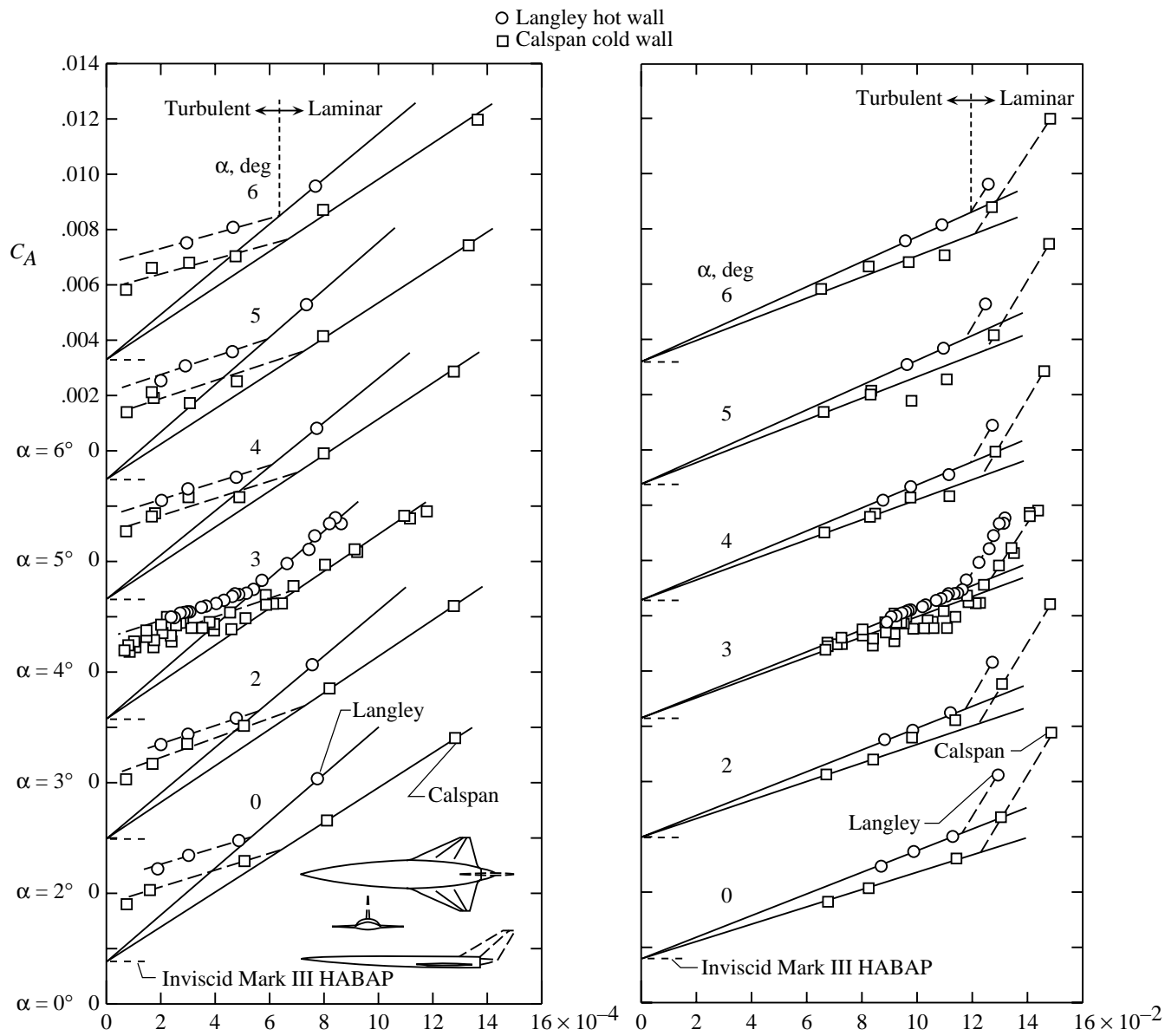(e) BWHV with $\delta_H = 0°$.

Figure 10. Concluded.

(a) Normal force.

Figure 11. Variation of force coefficients with Reynolds number at $M_\infty \approx 8.00$ for advanced blended body–wing hypersonic cruise configuration.

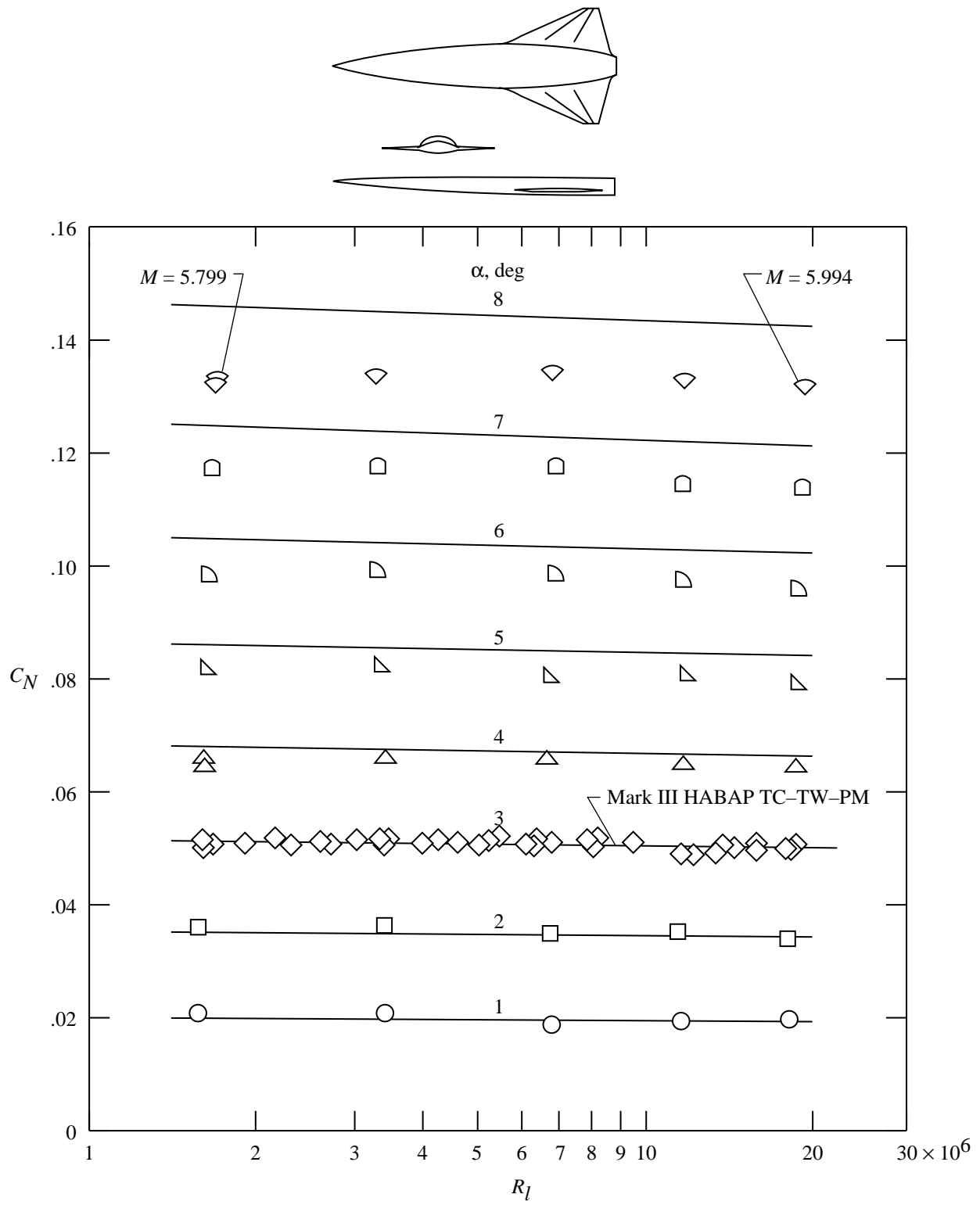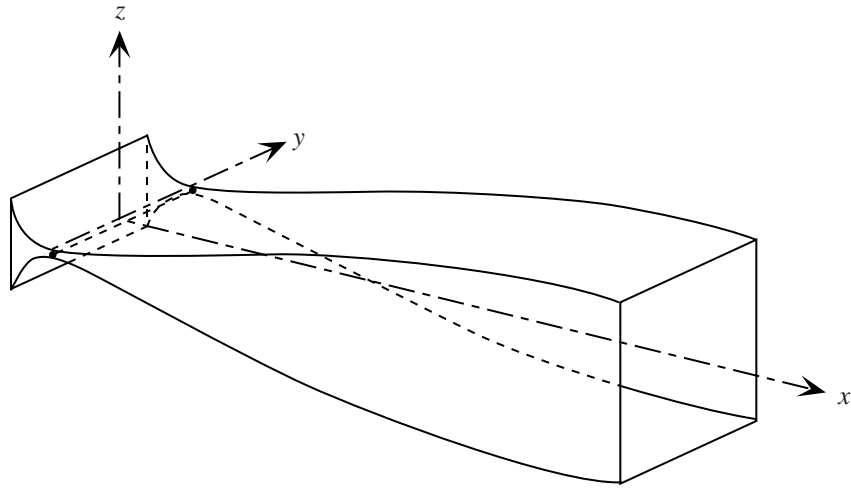(b) Axial force.

Figure 11. Concluded.

Figure 12. Variation of normal force coefficients with Reynolds number at $M_\infty \approx 6.00$ for advanced blended body–wing hypersonic cruise configuration.

Approach section

x, in.	z, in.
−1.736	1.950
−1.615	1.761
−1.493	1.573
−1.249	1.196
−1.005	0.837
−0.761	0.507
−0.713	0.446
−0.664	0.385
−0.615	0.330
−0.566	0.277
−0.518	0.227
−0.469	0.183
−0.420	0.146
−0.371	0.120
−0.347	0.109
−0.323	0.099
−0.298	0.090
−0.274	0.082
−0.250	0.073
−0.225	0.0682
−0.201	0.0634
−0.176	0.0585
−0.152	0.0536
−0.128	0.0526
−0.103	0.0507
−0.079	0.0487
−0.030	0.0468
−0.016	0.0467

Expansion section

| x, in.	z, in.	x, in.	z, in.	x, in.	z, in.
0	0.0467	4.861	1.2200	41.033	5.188
0.021	0.0469	5.731	1.440	42.931	5.256
0.039	0.0471	6.761	1.680	44.924	5.318
0.055	0.0474	7.982	1.942	47.016	5.375
0.071	0.0478	9.432	2.226	49.213	5.424
0.090	0.0483	10.257	2.377	50.353	5.446
0.115	0.0493	11.155	2.533	51.521	5.466
0.138	0.0502	12.137	2.695	52.719	5.484
0.160	0.0513	13.208	2.862	53.946	5.500
0.178	0.0523	14.378	3.035	63.889	5.500
0.215	0.0546	15.656	3.212		
0.243	0.0566	17.054	3.392		
0.263	0.0582	18.583	3.577		
0.310	0.0624	20.256	3.764		
0.356	0.0672	22.090	3.954		
0.400	0.0725	23.071	4.049		
0.442	0.0785	24.099	4.144		
0.482	0.0848	25.175	4.241		
0.524	0.0924	26.302	4.334		
0.641	0.1169	27.482	4.427		
0.721	0.1356	28.719	4.520		
0.823	0.1605	30.016	4.612		
0.953	0.1935	31.375	4.702		
1.123	0.2373	32.799	4.790		
1.679	0.3821	34.292	4.876		
2.413	0.5744	35.859	4.959		
3.161	0.7716	37.501	5.039		
3.908	0.9694	39.225	5.116		

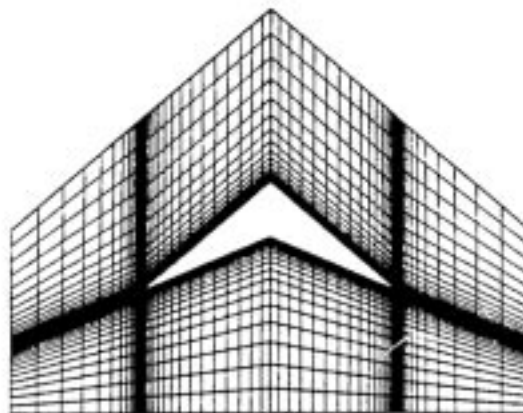Figure 13. Design of invar nozzle of Langley 11-Inch Hypersonic Tunnel.
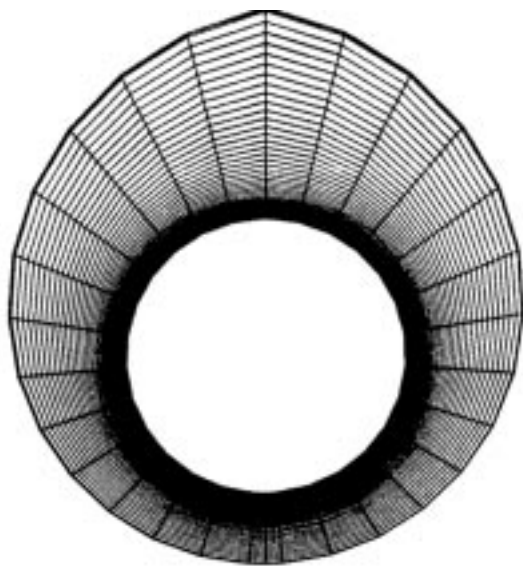
Cone with $\theta = 10°$
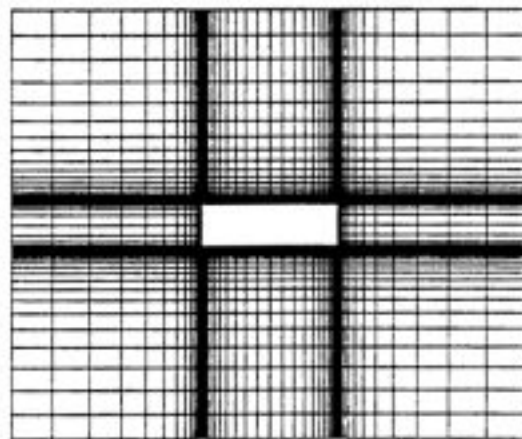
Rectangular wing with $A = 0.35$
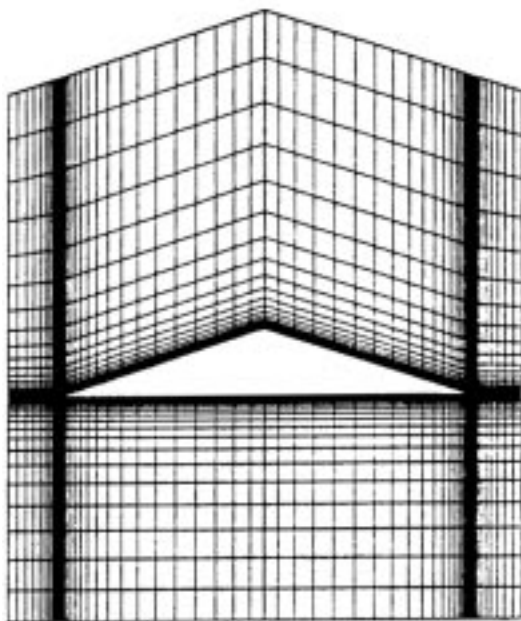
Delta wing

Caret wing

Figure 14. CFD grid in base plane of models. For cone, 33 percent shown, and for other models, 50 percent shown.
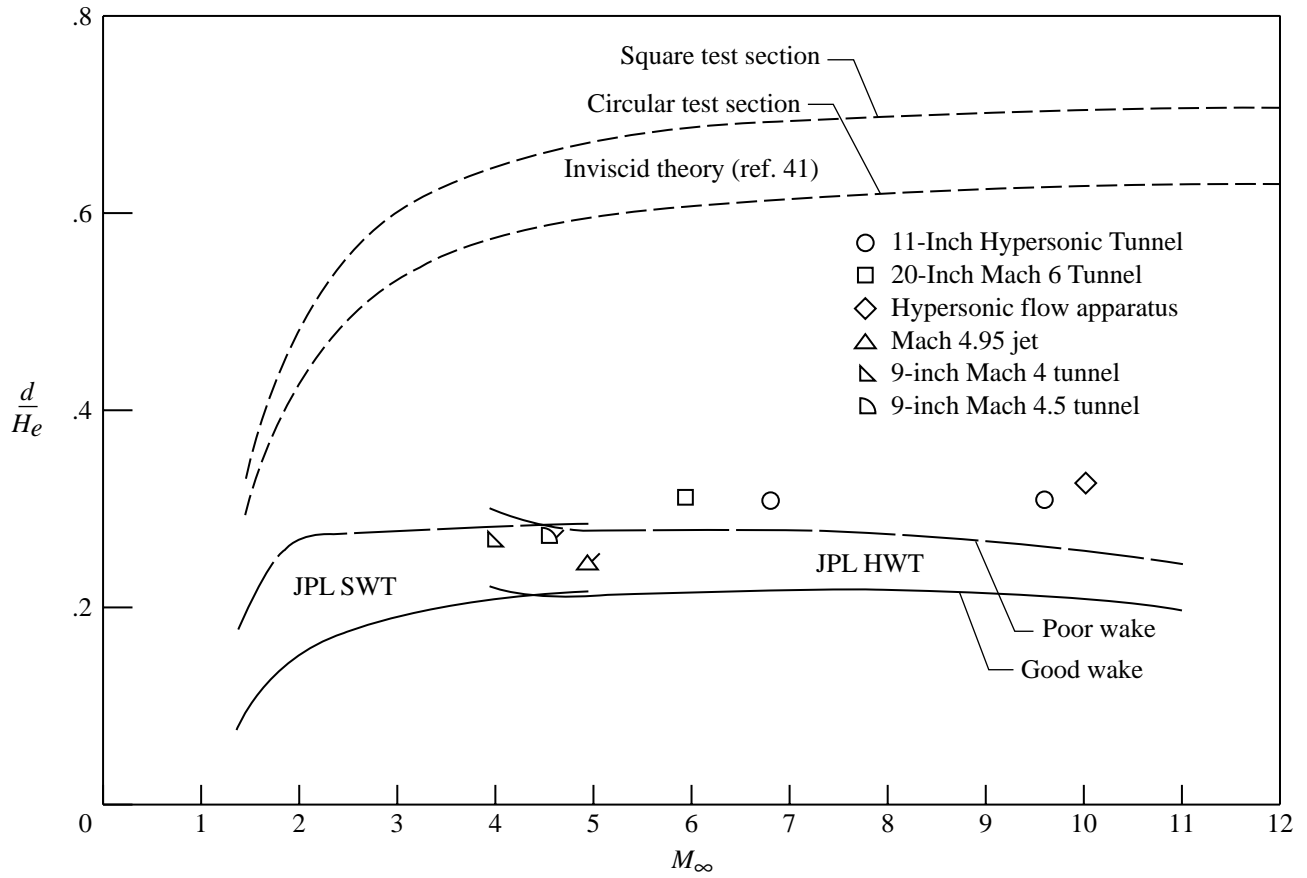
Figure 15. Ratio of disk diameter to effective test section height for determination of wind tunnel model size. Symbols with ticks indicate that δ^* was assumed to be approximately equal to 0.5δ.
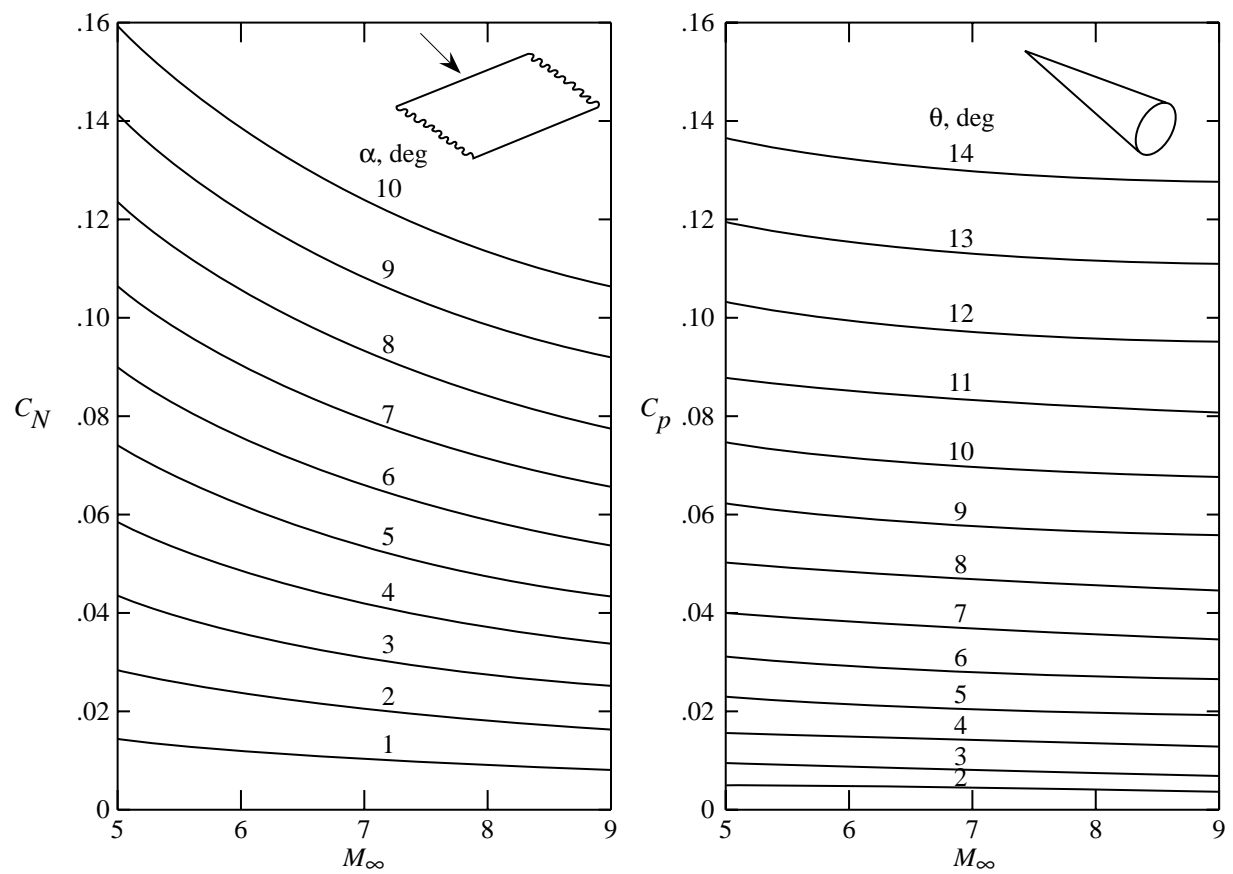
Figure 16. Normal force coefficient for infinite-span flat wing at various angles of attack and pressure coefficients for right circular cones at $\alpha = 0°$ versus free-stream Mach number.
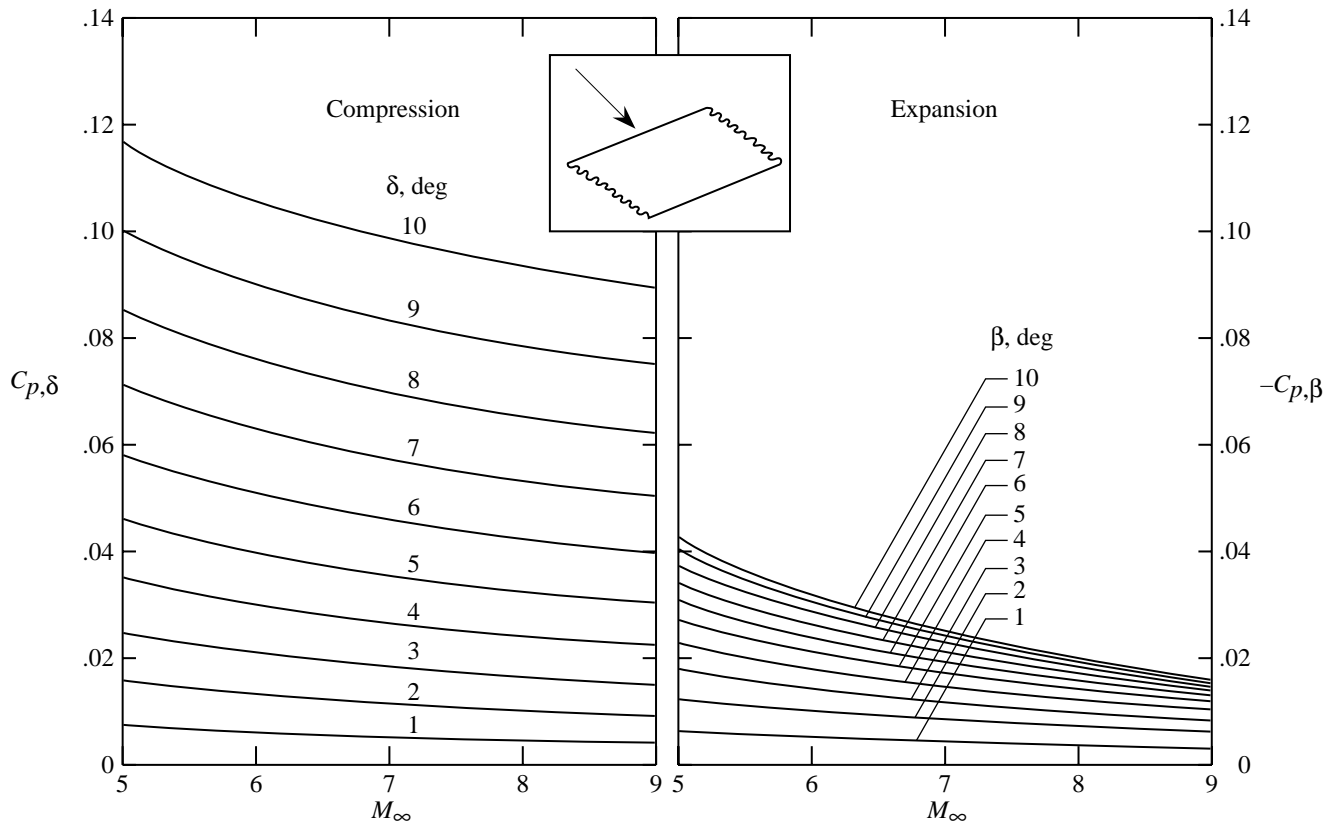
Figure 17. Pressure coefficients on compression and expansion sides of infinite-span flat wing versus free-stream Mach number.

REPORT DOCUMENTATION PAGE

Public reporting burden for this collection of information is estimated to average 1 hour per response, including the time for reviewing instructions, searching existing data sources, gathering and maintaining the data needed, and completing and reviewing the collection of information. Send comments regarding this burden estimate or any other aspect of this collection of information, including suggestions for reducing this burden, to Washington Headquarters Services, Directorate for Information Operations and Reports, 1215 Jefferson Davis Highway, Suite 1204, Arlington, VA 22202-4302, and to the Office of Management and Budget, Paperwork Reduction Project (0704-0188), Washington, DC 20503.

1. AGENCY USE ONLY *(Leave blank)*	2. REPORT DATE December 1997	3. REPORT TYPE AND DATES COVERED Technical Paper

4. TITLE AND SUBTITLE
Invariance of Hypersonic Normal Force Coefficients With Reynolds Number and Determination of Inviscid Wave Drag From Laminar Experimental Results

5. FUNDING NUMBERS
WU 505-70-63-01

6. AUTHOR(S)
Jim A. Penland and Richard Hawkins

7. PERFORMING ORGANIZATION NAME(S) AND ADDRESS(ES)
NASA Langley Research Center
Hampton, VA 23681-2199

8. PERFORMING ORGANIZATION REPORT NUMBER
L-17595

9. SPONSORING/MONITORING AGENCY NAME(S) AND ADDRESS(ES)
National Aeronautics and Space Administration
Washington, DC 20546-0001

10. SPONSORING/MONITORING AGENCY REPORT NUMBER
NASA TP-3673

11. SUPPLEMENTARY NOTES
Penland: Langley Research Center, Hampton, VA; Hawkins: Analytical Services & Materials, Inc., Hampton, VA.

12a. DISTRIBUTION/AVAILABILITY STATEMENT
Unclassified–Unlimited
Subject Category 02
Availability: NASA CASI (301) 621-0390

12b. DISTRIBUTION CODE

13. ABSTRACT *(Maximum 200 words)*
Observations have been made and reported that the experimental normal force coefficients at a constant angle of attack were constant with a variation of more than 2 orders of magnitude of Reynolds number at a free-stream Mach number M_∞ of 8.00 and more than 1 order of magnitude variation at $M_\infty = 6.00$ on the same body–wing hypersonic cruise configuration. These data were recorded under laminar, transitional, and turbulent boundary-layer conditions with both hot-wall and cold-wall models. This report presents experimental data on 25 configurations of 17 models of both simple and complex geometry taken at $M_\infty = 6.00$, 6.86, and 8.00 in 4 different hypersonic facilities. Aerodynamic calculations were made by computational fluid dynamics (CFD) and engineering methods to analyze these data. The conclusions were that the normal force coefficients at a given altitude are constant with Reynolds numbers at hypersonic speeds and that the axial force coefficients recorded under laminar boundary-layer conditions at several Reynolds numbers may be plotted against the laminar parameter (the reciprocal of the Reynolds number to the one-half power) and extrapolated to the ordinate axis to determine the inviscid-wave-drag coefficient at the intercept.

14. SUBJECT TERMS
Hypersonic normal force; Hypersonic axial force; Hypersonic Reynolds number; Laminar skin friction; Computation aerodynamics

15. NUMBER OF PAGES
65

16. PRICE CODE
A04

17. SECURITY CLASSIFICATION OF REPORT Unclassified	18. SECURITY CLASSIFICATION OF THIS PAGE Unclassified	19. SECURITY CLASSIFICATION OF ABSTRACT Unclassified	20. LIMITATION OF ABSTRACT